MEASUREMENT OF COSMIC-RAY MUON-INDUCED PROCESSES AT THE KAMLAND NEUTRINO EXPERIMENT

by

Dong-Ming Mei

A DISSERTATION

Submitted in partial fulfillment of the requirements
for the degree of Doctor in Philosophy in the
Department of Physics and Astronomy
in the Graduate School of
The University of Alabama

TUSCALOOSA, ALABAMA

2003

Submitted by Dong-Ming Mei in partial fulfillment

of the requirements for the degree of Doctor of Philosophy specializing in Physics.

Accepted on behalf of the Faculty of the Graduate School by the

dissertation committee:

_____

Louis J. Clavelli, Ph.D.

_____

Alexander L. Frenkel, Ph.D.

_____

Ion Stancu, Ph.D.

_____

Pieter B. Visscher, Ph.D.

_____

Jerome K. Busenitz, Ph.D.
Chairperson

_____

Stan Jones, Ph.D.
Department Chairperson

_____
Date

_____

Ronald W. Rogers, Ph.D.
Dean of the Graduate School

_____
Date

ii

LIST OF ABBREVIATIONS

KamLAND	Kamiokande Liquid Anti-Neutrino Detector
LMA	Large Mixing Angle
m.w.e.	meter-water-equivalent
LSND	Liquid Scintillator Neutrino Detector
K2K	KEK to Kamioka - Neutrino Oscillation Experiment
LSD	Large Volume Detector - Gran Sasso (3650 m.w.e.)
LVD	Large Scintillation Detector - Mont Blanc (5200 m.w.e.)
IMB	Irvine Michigan Brookhaven experiment
MACRO	Monopole, Astrophysics and Cosmic Ray Observatory
CHOOZ	Reactor Neutrino Experiment
Palo Verde	Reactor Neutrino Experiment
MC	Monte Carlo
ATWD	Analog Transient Waveform Digitizers
PMT	Photomultiplier Tube
p.e.	Photoelectrons
DAQ	Data Acquisition
NsumMax	The maximum number of PMT hits per event
TQ	Time and Charge
OD	Outer Detector
ID	Inner Detector
LS	Liquid Scintillator
MO	Mineral Oil
GEANT	Monte Carlo Simulation Program
GCALOR	Monte Carlo Simulation Program
MeV	10^6 eV
GeV	10^9 eV

ACKNOWLEDGMENTS

CONTENTS

LIST OF TABLES

LIST OF FIGURES

ABSTRACT

The cosmogenic activation and the fast neutrons produced by cosmic-ray muons are very important sources of background for all underground low rate experiments, including the KamLAND reactor neutrino experiment. The KamLAND experiment is the first entirely terrestrial experiment with enough sensitivity to verify or exclude the large mixing angle (LMA) solution using the reactor neutrino source. In the understanding of muon-induced backgrounds, the production of neutrons by cosmic-ray muons at a depth of 2700 meter-water-equivalent (m.w.e) has been measured with the KamLAND detector. About 1 kton of ultra-pure liquid scintillator and about 1.5 kton of ultra-pure buffer oil are used as the target. The neutrons were detected through the reaction $n + p \rightarrow d + \gamma$ (2.225 MeV) in the scintillator. Our measurement finds a neutron production yield of $(2.26 \pm 0.01$ (stat.) ± 0.40 (syst.) $) \times 10^{-4}$ neutrons per muon g/cm^2. We measure an average neutron multiplicity of 8±1 per muon-induced neutron production at a muon average energy of about 220 GeV. Our measurements are compared with the measurements at other depths and with theoretical models.

CHAPTER 1

INTRODUCTION

1.1   History of neutrinos

About a century ago, Becquerel discovered the phenomenon of radioactivity and Bohr realized that beta decay is a process in which the electron is ejected from the nucleus. Twelve years later, Chadwick measured the beta spectrum and discovered that the energy spectrum of beta is a continuous distribution. This led to a crisis in the principle of energy conservation in beta decay. In 1929, Wolfgang Pauli wrote a letter to a conference [1, 2] to save the principle of energy conservation in beta decay with the idea of a neutral particle of spin-$\frac{1}{2}$ involved in this reaction. Thus, the neutrino was born into the world of theoretical physics. After the neutron was discovered by Chadwick in cosmic rays in 1932, Fermi introduced the four-Fermi Hamiltonian [3] for beta decay using the neutrino, electron, neutron and proton. As a result, the field of weak interactions came into existence. In 1955 [4], Reines and Cowan discovered the neutrino. Since then, the study of neutrino physics has played an important role in understanding elementary particle properties and interactions.

1.2 Neutrinos in the Standard Model

In the Standard Model of particle physics, the fundamental fermions particles are grouped into three generations: (u, d, ν_e, e^-), (c, s, ν_μ, μ^-) and (t, b, ν_τ, τ^-). The particles in a higher generation differ from those in a lower generation only in mass. Each generation consists of two quarks (u, d), (c, s), or (t, b) and two leptons (ν_e, e^-), (ν_μ, μ^-), or (ν_τ, τ^-). The different kinds of particles are known as different "flavors". The quarks have a quantum number called color and come in three colors. Each lepton has a lepton number as the quantum number. The lepton numbers are assigned to three flavors separately. For instance, $L_e = 1$ for (e^-, ν_e), $L_\mu = 1$ for (μ^-, ν_μ) and $L_\tau = 1$ for (τ^-, ν_τ). Therefore, the names of the lepton numbers are different for different lepton families. The lepton number for the anti-lepton particle has the same absolute value as that for the lepton particle, but has an opposite sign. The quarks participate in strong interactions, in which the spin-one particle called gluons carry the force. The neutral neutrino particles participate only in weak interactions, in which W^+, W^- and Z^0, all of spin one, carry the force. Each particle has an associated anti-particle, which is identical in mass with the particle, but has an opposite electric charge. The Standard Model identifies these twelve building blocks of all matter and how these building blocks interact with one another through strong, weak and electromagnetic forces (in which photons, particles of spin one, carry the force).

Mathematically, symmetries have played a fundamental role in the Standard Model. There are two distinct kinds of symmetries for physical systems: global symmetries where the same symmetry transformation is applied to a field at all space-time points, and local symmetries where the symmetry transformations at different space-time points are unrelated. The existence of exact global symmetries always implies relations between masses and coupling constants among particles. The demands of a local symmetry require that some new spin-1 fields, called gauge

fields, be introduced into the theory. These gauge fields have interactions with all fields that transform non-trivially under the local symmetry.

The gauge group $SU(3)_c \times SU(2)_L \times U(1)_Y$ represents the Standard Model of electro-weak and strong interactions developed in the 1960's and 1970's. In the Standard Model, the neutrino is responsible for completing the lepton sector. The corresponding gauge group is $SU(2)_L \times U(1)_Y$. For each charged lepton (e, μ, τ), there is a corresponding neutral neutrino partner $(\nu_e, \nu_\mu, \nu_\tau)$, which is the so-called three active-flavored neutrino. Neutrinos only participate in weak interactions because they carry neither color nor electric charge. The interaction cross-section with matter is on the order of 10^{-43} cm^2 at neutrino energies of a few MeV. This makes neutrinos very difficult to detect.

In the Standard Model, all neutrinos are left-handed and all anti-neutrinos are right-handed. This conclusion was precisely what was found experimentally[5] prior to 1970. The parity transformation corresponds to space inversion, which can be violated in weak interactions.

The Standard Model assumes that the neutrinos are massless. It is, indeed, a requirement in the Lee-Yang Two-Component Theory of the Neutrino, necessary to explain why the weak force is so fundamentally parity violating. One consequence of this assumption is that the lepton number is conserved. For example, $\pi^- \rightarrow \mu^- + \bar{\nu}_\mu$. If the pion is at rest, then the muon and the anti-neutrino would come out back to back. Moreover, since the pion has spin 0, the muon and the anti-neutrino spins must be oppositely aligned. Therefore, if the anti-neutrino is right-handed, then the muon must be right-handed, too. In this reaction, the parity is violated, but the lepton number is conserved.

In summary, the Standard Model requires that the neutrino be massless and the lepton number be conserved. It implies that any violation of the lepton number conservation and any evidence of massive neutrinos must be physics beyond the Standard Model.

1.3   The neutrino puzzle

There are experimental evidences to suggest that neutrinos may indeed have a non-zero mass and non-conservation of lepton family number. We review here the experimental evidences from solar neutrinos and atmospheric neutrinos. Other experimental evidences, for example, the LSND effect and measurements at long baseline experiments such as K2K, are discussed later.

1.3.1   Solar neutrino problem

There are two nuclear fusion reaction chains responsible for the energy production in our Sun, namely the *pp*-cycle and the CNO-cycle. The overall effect of both cycles is the fusion of hydrogen nuclei into helium, with the emission of electron neutrinos:

$$4p \rightarrow^4 He + 2\nu_e + 2e^+ + 26.73 MeV \tag{1.1}$$
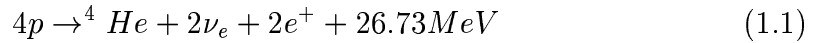
Many solar models have been developed in the past 30 years. The most famous and well-accepted model is certainly the Bahcall-Pinsonneault one (BP SSM [6]). Fig. 1.1 shows the neutrino energy spectra from the pp cycle of the BP2000 SSM model [7]. The CNO cycle contributes less than 2% to the total neutrino flux.

The BP SSM is believed to be correct since it has been checked with different arguments. One of the most impressive checks of the BP SSM is from the comparison between the BP98 model predictions, obtained without any adjustment of the parameters, and the most accurate helioseismology measurements of the sound speed [9]. The excellent agreement between the calculated and the measured values is displayed in Fig. 1.2. The size of the fraction difference between the measurements and the predictions (0.001 standard deviation for radii between 5% and 95% of the Sun radius) is much smaller than any generic change in the model with an impact on the predicted neutrino flux.
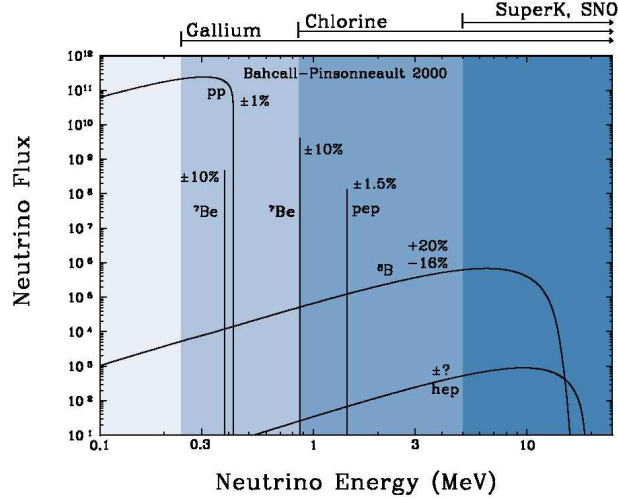
Figure 1.1. The predicted solar neutrino energy spectra from the pp-cycle (Fig. 1.1 from Ref. [8].) reaction [7]. It includes 98% of solar neutrino flux. The continuum spectra are expressed in event $\text{cm}^{-2}s^{-1}MeV^{-1}$ at one astronomical unit, while the monochromatic lines are given in event $\text{cm}^{-2}s^{-1}$. The uncertainties on the different flux components are also shown and the energy thresholds of the different experiments are indicated at the top of the plot.

About thirty-five years ago, Davis and his collaborators reported a detected flux of solar electron neutrinos that was significantly lower than the expected value from the Standard Solar Model (SSM). These first Homestake chlorine experimental results [10] were later confirmed by four other experiments, SAGE [11], GALLEX [12], Kamiokande [13], and Super-Kamiokande [14]. This solar neutrino flux deficit is the so-called solar neutrino problem (SNP).

In Table 1.1, the measured values of the integrated solar neutrino fluxes are compared with the BP2000 model predictions [7]. The rates are measured in Solar Neutrino Units (SNU), a convenient unit to describe the rates of solar neutrino experiments (1 SNU = 10^{-36} events atoms^{-1}s^{-1}).

In short, all experiments report a deficit of solar neutrinos compared to the pre-
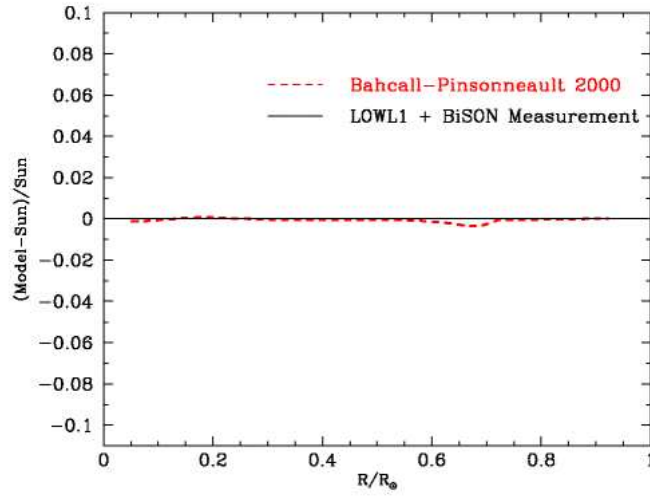
Figure 1.2. Comparison between the predictions (Model) and the measured (Sun) (Fig. 1.2 from Ref. [8].) sound speeds in the Sun. Predictions come from the BP98 model [6], while measurements come from the helioseismological data on the sound speed [9].

Table 1.1. Comparison between the measured integrated solar neutrino fluxes and the corresponding BP2000 predictions [7]. Units are SNU for chlorine and gallium experiments and 10^6 cm^{-2}s^{-1} for ^{8}B neutrinos.

Experiment	Measured	BP2000
Chlorine [10]	2.56 ± 0.23	$7.6^{+1.3}_{-1.1}$
GALLEX + GNO [12, 15]	$74.1^{+7.8}_{-6.7}$	128^{+9}_{-7}
SAGE [11]	$75.4^{+7.8}_{-7.4}$	128^{+9}_{-7}
^{8}B-Kamiokande [13]	$2.80\times(1.00\pm0.14)$	$5.05\times(1.00^{+0.20}_{-0.16})$
^{8}B-Super-Kamiokande [16]	$2.32\times(1.00\pm0.03)$	$5.05\times(1.00^{+0.20}_{-0.16})$
^{8}B-SNO [17]	$2.39\times(1.00\pm0.34)$	$5.05\times(1.00^{+1.01}_{-0.81})$
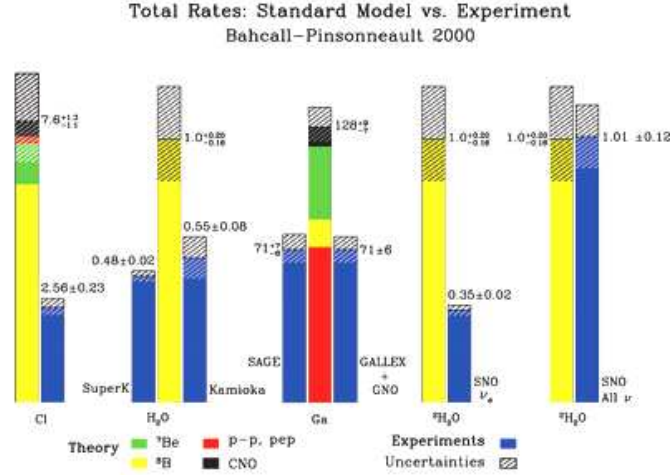
Figure 1.3. Measured vs. predicted solar neutrino rates (Fig. 1.3 from Ref. [8].) for all solar neutrino experiments. The predicted rates for the various components of the neutrino spectrum are taken from the BP98 model [6]. The columns (Cl, H_2O, Ga, etc) are the targets of experiments.

dictions. The deficit ranges from 31% 60 66% depending on ν_e energy. Fig. 1.3 [8] summarizes the inconsistency of the solar neutrino results between the measurements and the predictions, where a breakdown of all the measured and calculated event rate is shown as a function of the experimental technique and of the different reactions contributing to the solar neutrino flux. In summary, the solar neutrino problem is clearly stated in Table 1.1 and in Fig. 1.3.

1.3.2 The atmospheric neutrino anomaly

The atmospheric neutrinos are born in the atmosphere created by pion and kaon decay chains, for example, $\pi^+ \rightarrow \mu^+ + \nu_\mu$, $\mu^+ \rightarrow e^+ + \nu_e + \bar{\nu}_\mu$. From this decay chain one can see that twice as many muon-flavored neutrinos as electron-flavored neutrinos will be produced. The experiments which measure the atmo-

spheric neutrino flux have brought up a discrepancy. The so-called double ratio, $R=\frac{(\nu_\mu/\nu_e)_{measured}}{(\nu_\mu/\nu_e)_{predicted}}$ (one can reduce the uncertainties associated in both measuring and predicting the absolute fluxes), is found to be closer to 0.5 instead of 1. It is reported by both the IMB and the Kamiokande experiments [18, 19]. This value of the double ratio is confirmed by the Super-Kamiokande [14] and the MACRO experiment [20]. This difference between measurements and predictions is the so-called atmospheric neutrino anomaly.

1.4   The solution to the neutrino puzzle

In 1955, Gell-Mann and Pais [21] proposed the idea of mixing eigenstates in the neutral kaon system responsible for the weak decay of the kaon. This proposal put forth the existing possibility of particle-antiparticle oscillations in nature and led Pontecorvo [22] to postulate the phenomenon of neutrino oscillations in 1958. Later, Maki *et al* [23] extended this idea to oscillations between the neutrino flavors after the muon neutrino was discovered and proved to be a distinct particle. Pontecorvo and Bilenky [24] reviewed the experimental situation and stated the new standard treatment of neutrino flavor oscillations in 1978. Interest in this field has been revived by several very interesting experimental results, which reached the stage where the interpretation of the measurements in terms of oscillations between the flavors is inescapable. This is only possible if neutrinos have non-zero and non-degenerate masses, which are the so-called new physics beyond the Standard Model of the electro-weak interactions.

1.4.1   General formalism of neutrino oscillations
1.4.1.1   General description

In general, neutrinos are produced by charged current weak interactions. For example, neutrinos are produced through $W^+ \rightarrow l^+ \nu_l$ in pion or nuclear beta de-

cay, where $l = e, \mu, \tau$. Apparently, neutrinos produced this way are eigenstates of the weak interactions, which are known as flavor eigenstates. If there are mass differences among the neutrino flavors, then the flavor eigenstates and the mass eigenstates are not necessarily coincident, which indicates that the flavor orthonormal eigenstates can be expanded in terms of mass orthonormal eigenstates:

$$|\nu_l > = \sum_\alpha U^*_{l\alpha}|\nu_\alpha >, \tag{1.2}$$

where ν_l (l = e, μ, τ) represents the three flavor eigenstates that participate in charge current weak interactions, ν_α (where α runs over all the existing mass eigenstates) stands for mass eigenstates, and $U^*_{l\alpha}$ are the elements of unitary matrix.

Note that the measurements of the Z_0 width from LEP constrain the number of active neutrinos to be $N_\nu = 2.994 \pm 0.012$ [25]. Yet nothing forbids the existence of more than three neutrinos of definite masses so far. Moreover, to accommodate all the experimental results on neutrino oscillations (solar neutrino, atmospheric neutrino and LSND), the existence of at least one sterile neutrino is necessary, which leads to the four independent mass eigenstates. A change of basis from the mass to the flavor eigenstates requires one more linear combination,

$$|\nu_s > = \sum_\alpha U^*_{s\alpha}|\nu_\alpha > \tag{1.3}$$

which has no normal weak couplings. Eq.(1.3) is referred to as the sterile neutrino equation. However, for the sake of simplicity, we will only discuss the three active neutrino flavors.

In writing this, we assumed that the neutrinos (ν_α) are stable particles and $E_\alpha = \sqrt{p^2 + m_\alpha^2}$ in units where c = $\hbar$ = 1, where p is the 3-momentum. After time t, the evolution of the initial state of Eq.(1.2) gives

$$|\nu_l(t > 0) > = \sum_\alpha e^{-iE_\alpha t} U^*_{l\alpha}|\nu_\alpha > \tag{1.4}$$

At any time t, the probability of finding a ν_β in an originally ν_l state is given by:

$$P(\nu_l \to \nu_\beta) = |<\nu_\beta(t)|\nu_l>|^2 = |\sum_\alpha U_{\beta\alpha}e^{-iE_\alpha t}U_{l\alpha}^*|^2 \tag{1.5}$$

In all practical situations, neutrinos are extremely relativistic. In the ultra-relativistic limit,

$$E_\alpha \sim |p| + \frac{m_\alpha^2}{2|p|} \tag{1.6}$$

Considering the unitary condition for U and Eq.(1.6), Eq.(1.5) can be expressed as

$$P(\nu_l \to \nu_\beta) = \sum_\alpha |U_{\beta\alpha}|^2|U_{l\alpha}|^2 + 2Re\sum_{\gamma>\alpha} U_{\beta\alpha}U_{\beta\gamma}^*U_{l\alpha}^*U_{l\gamma}e^{i\frac{\Delta m_{\gamma\alpha}^2 L}{2E}} \tag{1.7}$$

where $\Delta m_{\gamma\alpha}^2 = m_\gamma^2 - m_\alpha^2$, the t is replaced by length L, which are equivalent in these units. Thus the oscillation probability $P(\nu_l \to \nu_\beta)$ is periodic (in the limit of between two flavors) in distance with a characteristic oscillation length that depends on the squared-mass difference of the various eigenstates and the neutrino energy.

The unitary mixing matrix U, known as the Maki-Nakagawa-Sakata (MNS) matrix [26] in the case of three neutrino flavors, is given by:

$$\begin{pmatrix} \nu_e \\ \nu_\mu \\ \nu_\tau \end{pmatrix} = \begin{pmatrix} U_{e1} & U_{e2} & U_{e3} \\ U_{\mu 1} & U_{\mu 2} & U_{\mu 3} \\ U_{\tau 1} & U_{\tau 2} & U_{\tau 3} \end{pmatrix} \begin{pmatrix} \nu_1 \\ \nu_2 \\ \nu_3 \end{pmatrix} \tag{1.8}$$

In a form analogous to that of the CKM quark sector matrix [27] for Dirac neutrinos, the U matrix is:

$$U = \begin{pmatrix} c_{12}c_{13} & s_{12}c_{13} & s_{13}e^{-i\delta} \\ -s_{12}c_{23} - c_{12}s_{23}s_{13}e^{i\delta} & c_{12}c_{23} - s_{12}s_{23}s_{13}e^{i\delta} & s_{23}c_{13} \\ s_{12}s_{23} - c_{12}c_{23}s_{13}e^{i\delta} & -c_{12}s_{23} - s_{12}c_{23}s_{13}e^{i\delta} & c_{23}c_{13} \end{pmatrix} \tag{1.9}$$

where the standard convention $c_{ij} = \cos\theta_{ij}$ and $s_{ij} = \sin\theta_{ij}$ (i,j = 1,2,3 are the generation labels). Thus in this formalism, the mixing matrix has three mixing angles and one CP-violating phase, δ.

In the case of oscillation between two Dirac neutrinos, the matrix U defined in Eq.(1.9) takes a particularly simple form:

$$U = \begin{pmatrix} cos\theta & sin\theta \\ -sin\theta & cos\theta \end{pmatrix}$$

where θ is the mixing angle, analogous to the Carbibo angle for the quarks. The flavor eigenstates can expanded as:

$$|\nu_l> = cos\theta|\nu_1> +sin\theta|\nu_2> \tag{1.11}$$

$$|\nu_\beta> = -sin\theta|\nu_1> +cos\theta|\nu_2> \tag{1.12}$$

The oscillation probability in this case is as follows:

$$P(\nu_l \rightarrow \nu_\beta) = sin^2 2\theta sin^2(\pi \frac{L}{\lambda_{osc}}) \tag{1.13}$$

where $\lambda_{osc} = \frac{4\pi E}{\Delta m^2}$ is the oscillation wavelength, E is the neutrino energy and Δm^2 is the squared mass difference.

Substituting the definition of λ_{osc} into Eq.(1.13), the oscillation probability takes its usual form:

$$P(\nu_l \rightarrow \nu_\beta) = sin^2 2\theta sin^2(\frac{1.27\Delta m^2 L}{E}) \tag{1.14}$$

where Δm^2 is expressed in eV^2, the distance from the detector to neutrino source L is in meters (km) and the neutrino energy E is in MeV (GeV). The factor, $1.27 = 10^3/(4\hbar c)$, results from the conversion from natural units to laboratory units. In the oscillation probability equation 1.14, $sin^2 2\theta$ is an intrinsic parameter which describes the strength of the coupling between the two neutrino flavors. $sin^2(\frac{1.27\Delta m^2 L}{E})$ is dependent on experimental conditions. In order to have sensitivity to small values of Δm^2 , the ratio of E/L must also be small. This can be achieved by having low energy neutrino beams and large distances between the neutrino sources and the detector.

1.4.1.2   MSW effects

When neutrinos propagate in matter, neutrinos of all flavors can have neutral current interactions with the protons, neutrons and electrons of the medium. However, only electron neutrinos can interact with the electrons by charged current exchange. Under the favorable circumstances of a resonance enhancement of the oscillation amplitude, the so-called Mikheyev-Smirnov-Wolfenstein (MSW) effect [28] can take place.

As an example in the charged current interaction, the potential of ν_e is different from the other types of neutrinos because of its charged current interaction of ν_e-e. This potential is computed to be

$$V_e = \sqrt{2} G_F N_e, \tag{1.15}$$

where G_F is the Fermi coupling constant and N_e is the electron number density.

In the case of constant electron density, the matrix U defined in Eq.(1.9) can be represented as:

$$U = \left(\begin{array}{cc} cos\theta_m & sin\theta_m \\ -sin\theta_m & cos\theta_m \end{array} \right)$$

where θ_m is the matter mixing angle defined by:

$$tan2\theta_m = \frac{sin2\theta}{cos2\theta - \frac{L_{osc}}{L_0}} \tag{1.17}$$

where L_0 is the neutrino interaction length for charged current (CC) interactions:

$$L_0 = \frac{2\pi}{V_e} = \frac{\sqrt{2}\pi}{G_F N_e} \tag{1.18}$$

The matter mixing angle will become resonant when $cos2\theta = \frac{L_{osc}}{L_0}$. This is the resonant condition. The critical energy to have a MSW resonance for given parameters is

$$E_{crit} = \frac{\Delta m^2 cos2\theta}{2\sqrt{2} G_F N_e^{max}} \tag{1.19}$$

where N_e^{max} is the maximum electron density in the Sun. Therefore. the neutrino spectrum is suppressed in the region of energies higher than E_{crit}.

The probability that a ν_e is converted to a ν_μ after traceling in matter a distance L is now written:

$$P(\nu_e \to \nu_\mu; L) = sin^2 2\theta_m sin^2 (\frac{\pi L}{L_m}) \qquad (1.20)$$

where

$$L_m = L_{osc}(\frac{sin 2\theta_m}{sin 2\theta}) \qquad (1.21)$$

The above constant electron density solutions are also valid in matter of variable density if the changes in the electron density occurs on a distance scale much larger than the matter oscillation length (L_m).

1.4.2 The experimental solution for neutrino puzzle

1.4.2.1 Solar neutrino solution

Neutrino oscillations, with the probability of a resonant enhancement, provide a satisfactory explanation of the solar neutrino problem. If solar electron neutrinos have transformed into muon or tau neutrinos before reaching the detector, then the disappearance in all experiments would be an expected effect. The SNO detector [17] would detect the muon and tau neutrinos via neutral current measurement. Furthermore, the neutrino flux measured via neutral current measurement should agree with BP SSM. SNO has published the charge current result and the neutral current result. In Ref. [29], the charge current result is significantly different from the expectation from BP SSM, while the total neutrino flux measured from the neutral current result ($\phi_{NC} = 5.09^{+0.44}_{-0.43}$ (stat.)$^{+0.46}_{-0.43}$(syst.)$\times 10^{-6}$ cm^{-2} s^{-1}) agrees with the expectation ($\phi_{SSM} = 5.05^{+1.01}_{-0.81} \times 10^{-6}$ cm^{-2} s^{-1}) from BP SSM. The SNO neutral current result strongly suggests that the oscillation scenario is responsible for the solar electron neutrino disappearance. The differ-

ence in the square of the masses (Δm^2) of the neutrinos involved in solar neutrino experiments is $\sim 10^{-5} eV^2$.

Interpreting the solar neutrino deficit in the two-flavor mixing framework, the allowed regions can be drawn on the oscillation parameter space ($\tan^2\theta$, Δm^2) at the set confidence level (C.L.). The proposed oscillation solutions as obtained in Ref. [30] are oscillations in matter (MSW solutions) and in vacuum ("Just-so", or VO solutions) from a combined analysis of the total rate results in the chlorine, SAGE, GALLEX and Super-Kamiokande experiments. The matter solutions are conventionally named according to the allowed ranges of the oscillation parameters: small mixing angle (SMA, $\Delta m^2 \sim 10^{-5}$ eV^2, $\tan^2\theta \sim 10^{-4}$ - 10^{-2}), large mixing angle (LMA, $\Delta m^2 \sim 10^{-5}$ - 10^{-4} eV^2, $\tan^2\theta > 0.1$) and low Δm^2 (LOW, $\Delta m^2 \sim 10^{-7}$ eV^2, $\tan^2\theta >0.4$). The VO solution ($\Delta m^2 < 10^{-9}$) is the case for which one astronomical unit matches the neutrino oscillations length for typical solar energies. Fig. 1.4 shows the allowed ranges for the MSW solutions.
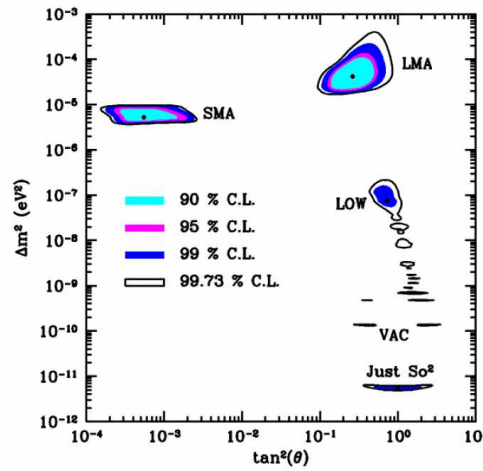
Figure 1.4. The allowed ranges of solar neutrino oscillation solutions. (Fig. 1.4 from Ref. [8].)

1.4.2.2   Atmospheric neutrino solution

The high energy cosmic-rays which produce neutrinos have provided experiments the opportunity to measure both the electron flavor and the muon flavor neutrino flux. Therefore, the double ratio as discussed earlier can be checked. Here, the measured results are explained by the following scenarios:

1. the muon neutrino flux is low due to $\nu_\mu \to \nu_\tau$.

2. the electron neutrino flux is high due to $\nu_\mu \to \nu_e$.

Scenario (1) is consistent with the neutrino oscillation hypothesis and the maximum oscillation is found by Super-Kamiokande [14]. Fig. 1.5 shows the zenith angular dependence of multi-GeV neutrinos observed in Super-Kamiokande detector.
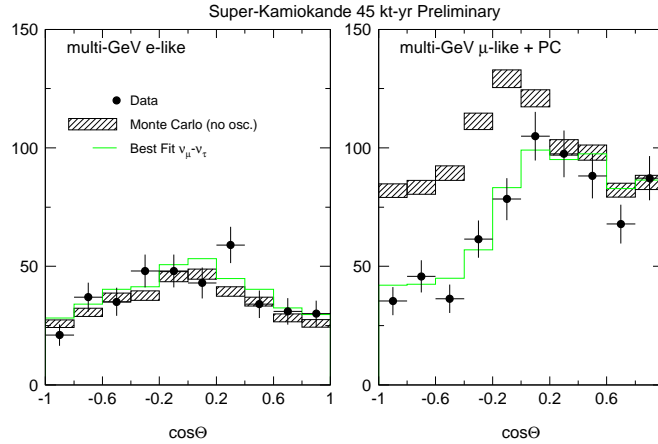
Figure 1.5. Zenith-angle dependence of multi-GeV neutrino interactions obtained from Super-Kamiokande [16]. The boxes show the expectation without any oscillation. The lines are the fitted lines with some assumed oscillation parameters, as described in Ref. [16]

.

The K2K experiment reports an indication of neutrino oscillation: a reduction of ν_μ flux together with a distortion of the energy spectrum [31]. The difference in the square of the masses (Δm^2) of the neutrinos involved is $\sim 10^{-3} eV^2$. Scenario (2) is excluded at 90% confidence level by the CHOOZ [32] and the Palo Verde [33] experiments utilizing reactor neutrinos.

1.4.2.3 The LSND accelerator neutrino experimental result

The neutrino oscillation hypothesis is also tested employing the accelerator neutrinos. A Liquid Scintillator Neutrino Detector (LSND) has reported [34] the result of $\bar{\nu}_\mu \to \bar{\nu}_e$ oscillation. The difference in the square of the masses (Δm^2) of the neutrinos involved is $\sim 10^{-2} eV^2$. Although LSND reported strong evidence for neutrino oscillations, more experimental data will be needed to firmly establish the result. The MiniBooNE experiment will address the LSND effect.

1.4.2.4 Summary of the neutrino oscillation hypothesis

The above experimental evidences support the hypothesis of neutrino oscillations. This is only possible if neutrinos have non-zero and non-degenerate masses, which is contrary to what assumed in the Standard Model of electro-weak interactions. The evidence for neutrino oscillations would represent a major discovery in elementary particle physics and would then require an extension of the currently accepted description of sub-nuclear phenomena beyond the Standard Model. However, although the neutrino oscillations have been used as the solutions to explain the solar neutrino problem and atmospheric neutrino anomaly, very little is known about the oscillation properties: (1) the mixing angles (exact values); (2) the difference in the square of the masses (Δm^2); and (3) the neutrino species exist in nature. Experimentally, we have three independent Δm^2 values from solar neutrino experiments, atmospheric neutrino experiments and LSND. In the Standard Model, the three active-favored neutrinos correspond to two independent Δm^2

values. Therefore, the observation of three independent Δm^2 values requires a new explanation for the existence of the generations of neutrinos. Theoretically, there are several different oscillation solutions as discussed earlier. The mixing angles, the difference in the square of the masses (Δm^2) and the species of neutrinos are correlated to the neutrino oscillation solutions. Testing neutrino oscillations then become necessary.

1.4.2.5 Test of the solar neutrino oscillation hypothesis

Although the measured results from Super-Kamiokande and SNO favor the LMA solution, there are still a lot of open questions to be answered. A test of the LMA solution is being made by the KamLAND [35] experiment, a 1 kton pure liquid scintillator detector located in the Kamioka mine in Japan. KamLAND is the first terrestrial experiment with enough sensitivity to confirm or exclude one of the possible solutions to the solar problem, the large-mixing-angle MSW solution, or the LMA. KamLAND detects the low-energy (1-8 MeV) $\bar{\nu}_e$ flux emitted by the nuclear reactors at 16 Japanese power stations. Among these power stations, 80% of $\bar{\nu}_e$ flux comes from reactors at a distance between 140 and 210 km from the detector. KamLAND experimental sensitivity, $\Delta m^2 \leq 10^{-5}$ eV^2, is good enough to be the first direct test of the LMA solutions. The excluding ranges of the oscillation parameters space $(\Delta m^2, \sin^2 2\theta)$ are shown in Fig. 1.6. As can be seen in Fig. 1.6, KamLAND is the only experiment to be sensitive to the LMA solution using reactor neutrinos.
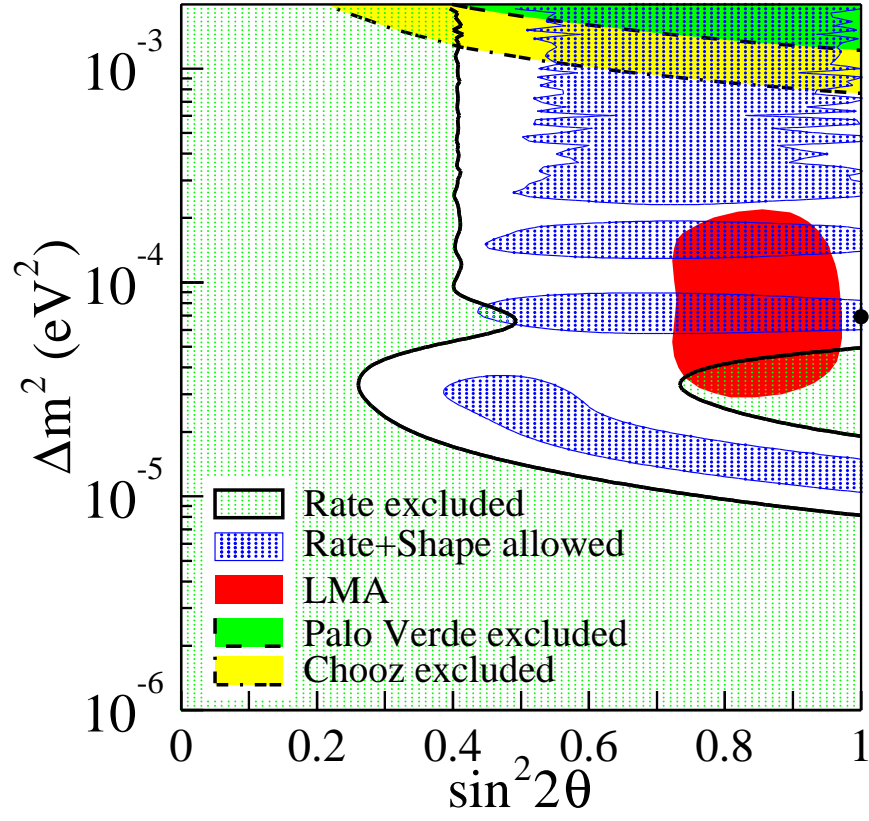
Figure 1.6. Allowed and excluded regions in the Δm^2 - $\sin^2 2\theta$ plane for neutrino oscillations (Fig. 1.6 from Ref. [35]). In this plot, the 95% C.L. allowed region of the large mixing angle (LMA) solution of solar neutrino experiments is shown, which corresponds only to the KamLAND experimental sensitivity. The solid dot shows the best fit to the KamLAND data from the first result.

1.5   KamLAND reactor experiment

The KamLAND experiment uses electron anti-neutrinos produced from nuclear reactors. Electron anti-neutrinos are primarily captured by protons in the detector's liquid scintillator according to the reaction:

$$\bar{\nu}_e + p \rightarrow e^+ + n \qquad (1.22)$$

The positrons have energies of a few MeV, which they lose energy by ionization and annihilate with electrons to produce the two annihilation gammas. The total energy deposit induced by positron provides a prompt signal in the above reaction. However, the neutron is thermalized and captured in the reaction

$$n + p \rightarrow d + \gamma \quad (2.225 MeV) \qquad (1.23)$$

The capture time is about 200 μs in the scintillator. This reaction provides a delayed signal for the reaction (1.22). Therefore, reactor neutrino events have a clear signature of a delayed coincidence between the prompt signal (positron + annihilation gammas) and delayed signal (neutron capture gamma).

Although the signal is clean, the background is still very important to know because of the low rate signal. In searching for the neutrino oscillation using reactor neutrinos, the event rate analysis and the analysis of the shape of the positron energy spectrum are commonly used. Fig. 1.7 shows the event rate analysis results for the reactor neutrino experiments, while the positron energy spectrum is shown in Fig. 1.8. Both strategies are conditional upon the understanding of the backgrounds induced by cosmic-ray muons.
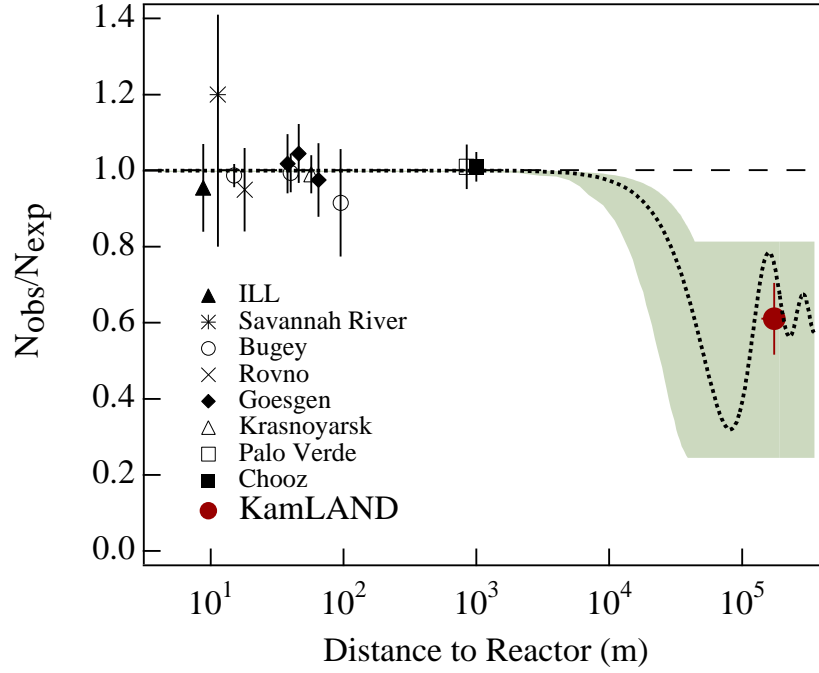
Figure 1.7. The ratio of measured to expected $\bar{\nu}_e$ flux from reactor neutrino experiments [35]. The solid dot is the KamLAND point plotted at a flux-weighted average distance (the dot size is indicative of the spread in the reactor distance). The shaded region indicates the range of flux predictions corresponding to the 99% C.L. LMA region found in a global analysis of the solar neutrino data [37]. The dotted curve corresponds to $\sin^2 2\theta = 0.833$ and $\Delta m^2 = 5.5 \times 10^{-5}$ eV^2 and is representative of recent best-fit LMA predictions while the dashed curve shows the case of no oscillations.
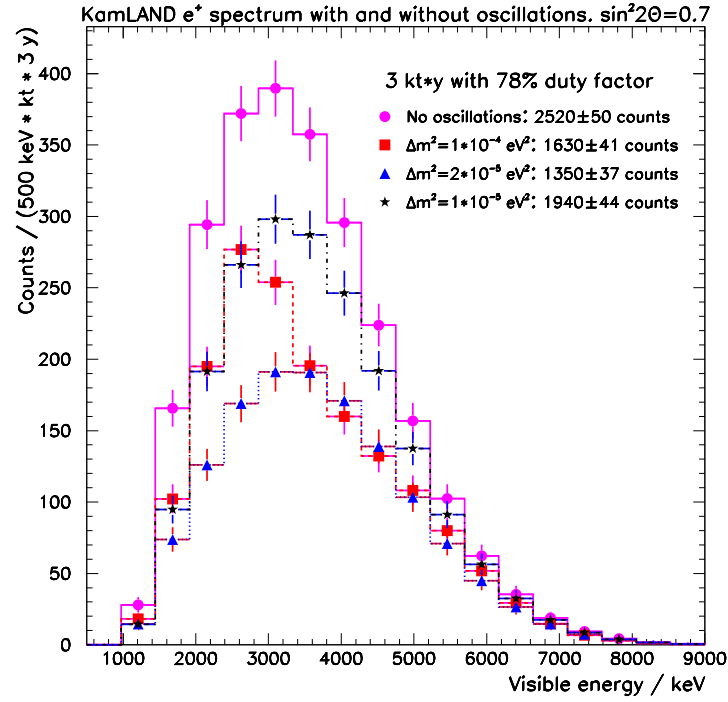
Figure 1.8. The visible e$^+$ energy spectrum (including photons from e$^+e^-$ annihilations) from the reactor neutrinos expected in KamLAND [36] for different types of oscillation scenarios and for the case of no oscillations. It assumes an exposure of 3-kt-y at 78% of the maximum power flux and 100% of detection efficiency.

1.6   The motivation for measuring neutrons

Even below the surface of the Earth, fast neutrons induced by cosmic ray muons are an important source of backgrounds for underground low-rate experiments. The KamLAND reactor neutrino oscillation experiment estimated fast neutrons to be the dominant background [35] for the case where the fiducial volume is comprised of the whole mass of the liquid scintillator target. We distinguished two classes of fast neutrons: (a) neutrons produced by muons traversing the detector itself, (b) neutrons created in the external rock by muons missing the detector. Type (a) neutrons can be tagged with finite efficiency with a muon veto detector system. For type (b) neutrons no such convenient tag exists. Therefore, un-tagged neutrons are an unavoidable source of background. Knowledge of the neutron production rate is thus essential to the quantitative understanding of the neutron induced background in low-rate experiments such as KamLAND.

A substantial disagreement exists between different analytical calculations and measurements of the neutron production yield and multiplicity. Furthermore, the data reported by different experiments are not always consistent in the following:

1. **Neutron production rate**

   The total neutron production rate has been measured at various depths [38, 39, 40, 41, 42, 43]. However, some inconsistencies seem to exist at large overburden. Especially the LSD [42] and LVD [43] data points exhibit a rather large discrepancy (Fig. 1.9). A measurement of the neutron production yield at the depth of KamLAND (2700 mw.e) is therefore important in resolving this puzzle.

   Y-F Wang *et al.* approached neutron production employing the Monte Carlo (MC) simulation package FLUKA [44]. The corrected neutron yield in their paper is expressed as a function of muon energy (GeV): $N_n = 4.14 \times E_\mu^{0.74} \times 10^{-6}$ neutron/$(\mu \ g \ cm^{-2})$. Predicted production yields for the LVD (3650

mw.e) and LSD (5200 mw.e) depths are $N_n = 2.61 \times 10^{-4}$ n/μ g cm^{-2} and $N_n = 3.35 \times 10^{-4}$ n/μ g cm^{-2}, respectively. These values differ by 4.3 σ and 2 σ respectively from the experimental data.
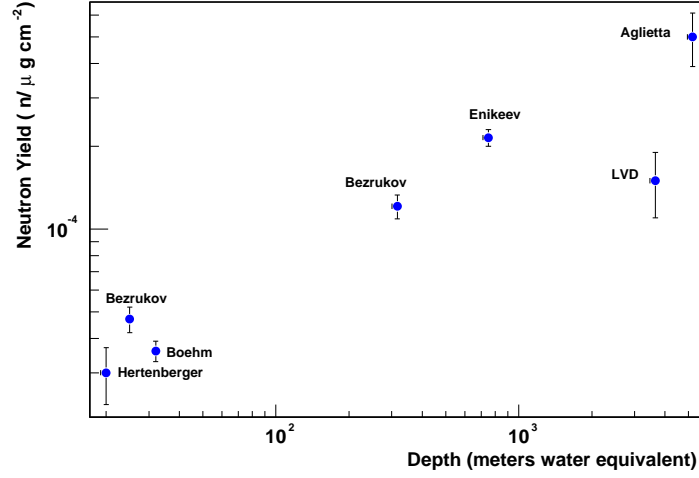
Figure 1.9. This plot shows a summary of available data on the total neutron production versus depth. The points are labeled by the corresponding first author [38, 39, 40, 41, 43] and the collaboration [42].

2. **Neutron multiplicity**

Neutron multiplicity is the least known quantity in neutron production by muons. There are only a few experimental results regarding neutron multiplicity. The Palo Verde experiment [39] utilized a detector situated at a shallow depth (32 mw.e.). A two-neutron to one-neutron ratio between 5 and 10, depending on the assumed three-neutron yield, was observed. Bezurukov *et al.* [40] reported results similar to those of Palo Verde, using a low-overburden detector. Ref. [44] states that the multiplicity of the MC

prediction is a factor 2 different from the results reported by these measurements.

The purpose of this thesis is to present a measurement of these two quantities with improved precision.

CHAPTER 2

KAMLAND EXPERIMENT DESCRIPTION

2.1 KamLAND experimental site

This thesis is based on the data collected by the KamLAND experiment at Kamioka mine in Japan. The KamLAND detector is situated in the Kamiokande detector cavity under the summit of Mt. Ikenoyama in the Japanese Alps. The site is within 50 km of the town of Toyama. At this location, the rock overburden in any direction is more than 1000 meters, corresponding to about 2700 meters-water-equivalent (m.w.e)[45]. With an average rock density of 2.7 g/cm^3, the minimum surface energy required for a muon to reach the detector is above 1 TeV.

2.2 Detector description

2.2.1 Overview

A cutaway view of the KamLAND detector is shown in Figure 2.1.
The central detector of KamLAND is liquid scintillator. The scintillator consists of dodecane (80%), pseudocumene (PC, 1,2,4-Trimethylbenzene, 20%) and PPO (2,5-Diphenyloxazole, 1.5 g/liter). The central detector is spherical and has a
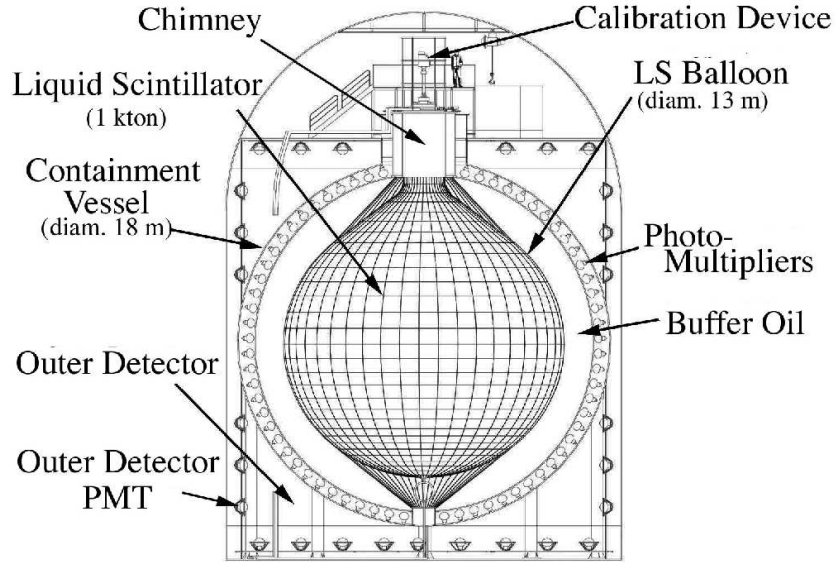
Figure 2.1. Schematic of the KamLAND detector.

diameter of 1300 cm. The scintillator is surrounded by a protective shell of ultra-pure paraffin oil which is about 250 cm thick. These two regions are separated by a 135 μm-thick Nylon/EVOH (Ethylene vinyl alcohol copolymer) balloon, that is transparent to blue light. The scintillator and the paraffin oil serve as the inner detector (ID). The ID is viewed by an array of 1879 photomultiplier tubes (PMTs), supported by a 1800 cm diameter stainless steel vessel. Among the total of 1879 PMTs, 1325 of the PMTs are of 17" PMTs. The balance is made of 20" PMTs left over from the Kamiokande detector. The scintillation light produced by the ionization of charged particle is detected by the ID.

The PMT sphere is almost completely surrounded and immersed in an external shield of ultrapure water, which fills the remainder of the detector cavity. This outermost layer, called the outer detector (OD), is instrumented by an array of 225 20" PMTs. The outer detector serves as an active muon veto detector. The

veto detector with water as the medium is used to detect cosmic-ray muons via
Čerenkov light.

2.2.2 Mechanical structure

The main mechanical structure of the ID is a stainless steel sphere, which
encloses the liquid scintillator and paraffin oil and supports the inner detector
PMTs. A set of 16 vertical columns and wall braces support the sphere at its
equator via a special ring reinforcement.

A chimney made of stainless steel with a cylinder of $\sim$3 m diameter protrudes
from the top of the sphere to permit access to the central detector. Concentric
with the stainless steel chimney is an acrylic chimney connected to the balloon.
The volume between the two chimneys is filled by buffer oil. The buffer oil filled
this way occupies the volume between the PMT sphere and the balloon. The
acrylic chimney provides access for the calibration device deployment and the
scintillator recirculation lines. The buffer oil recirculation lines are mounted in
the stainless steel sphere. A special radon-impermeable feed-through referred to
as a penetration allows the PMT signal and the high voltage cables to be fed out
of the buffer oil between the two chimneys and into the detector electronics.

The balloon is supported by nylon ropes. These are fed up through the region
between the two chimneys using a deflection sheave and terminate in load-sensing
and balancing whiffle-tree structure supported on the dock structure in the cavity.
The ropes are then sealed inside the radon-impermeable feed-throughs.

The inner detector PMTs are mounted inside the stainless steel sphere on a
diamond structure. All surface on the PMT sphere except the PMT photocathode
is covered by light-absorbing materials to reduce light reflection that confuses
event reconstruction.

The ultrapure water surrounding the PMT sphere absorbs much of the ra-
dioactivity coming from the walls and moderates the fast neutrons produced by

cosmic rays in the rock. As an active anti-coincidence veto, it detects the cosmic-ray muons traversing it. The veto detector has a cylindrical shape. The total volume of 4,500 m^3 of ultrapure water is divided into four main sections according to the placement of the PMTs: (1) the top section consists of the PMTs that are on the ceiling; (2) the upper section is composed of the PMTs along the wall that are suspended on a wire-cable anchor in the upper half of the cylinder; (3) the lower section is the lower half of the cylinder which has the PMTs along the wall that are suspended on a wire-cable anchor and (4) the bottom section is the PMTs that are on the floor. This structure can be seen in Fig. 2.1. The rock surface that touches the water is painted with a water-resistant urethane coating impermeable to radon.

2.3   Detector electronics and data acquisition

The KamLAND trigger is flexible and programmable. Data readout is initiated whenever more than 200 PMT hits are detected in a time window of 200 ns (a PMT hit is defined if the charge is registered by this PMT). In order to detect time-correlated events after each prompt trigger, a 1 ms time window is opened for a possible delayed event. The trigger threshold is then lowered to 120 PMT hits during this period. The maximum number of PMT hits, obtained in a 200 ns time window, is the so-called variable NsumMax, which is energy dependent. The 17-inch PMTs provide 22% photocathode coverage (this analysis is based on the data collected using 17-inch PMTs). We observe a light yield of about 300 photoelectrons (p.e.) per MeV at the center of the detector. Most of the PMT hits are due to single photoelectron events. Event triggers with hits in the OD are collected.

The KamLAND data acquisition system is based on a set of Analog Transient Waveform Digitizers (ATWD). The ATWD is designed to capture analog wave-

forms with 128 samples in a 200 ns interval for any input signal which surpasses an internal threshold level. If an event trigger is generated, then the captured analog signals are digitized by an internal ADC and buffered for readout. The digitization time is about 26 μs for energy deposits of a few MeV events. The start of the event sampling relative to the event trigger is recorded so that the arrival time of the signal can be obtained from the digitized waveform. Each PMT is connected to two ATWD channels in order to allow up to two close but separated events in time to be digitized without loss due to dead time. The average occupancy of the KamLAND detector for events around 2.2 MeV is less than 50%. Hence, even multiple neutron events can be recorded with distortions only in the channels where PMTs receive hits from more than two steps in a sequence.

2.4   Reactor information

There are 16 commercial nuclear power plants in Japan, supplying 130 GW thermal at maximum power [46]. Fig. 2.2 shows the reactor flux as a function of time.

For all practical purposes for each reactor the anti-electron neutrino flux and spectrum depend only on the composition of the core in terms of the four isotopes ^{235}U, ^{238}U, ^{239}Pu, ^{241}Pu. All 16 reactors together provide an anti-electron neutrino flux of 1.3×10^6 cm^{-2} s^{-2} for E$_{\bar{\nu}} > 1.8$ MeV at the Kamioka site. Eighty percent of this flux is from the reactors between 140 km and 210 km away. Therefore, the average baseline is about 180 km. For a 1 kton scintillator with a ratio of H/C 1.96, the expected number of $\bar{\nu}_e + \mathrm{p} \rightarrow \mathrm{e}^+ + \mathrm{n}$ events is about 700 per year without oscillations. The positron energy spectrum covers the range from 1.022 MeV to about 8 MeV.
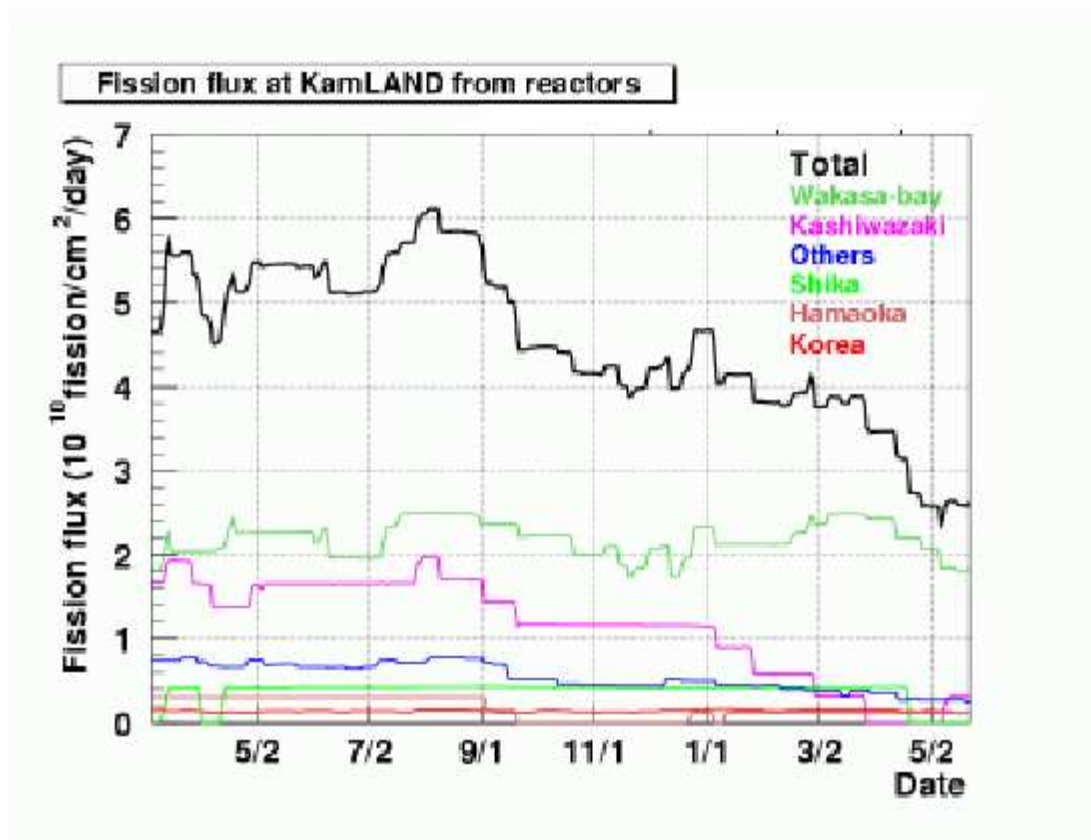
Figure 2.2. KamLAND reactor power flux. It is plotted as a function of time. The data period is from March 7, 2002 to May 27, 2003.

CHAPTER 3

DETECTOR CALIBRATION

The calibration is responsible for a thorough understanding of the detector performance, which is crucial in extracting reliable physics conclusions from the observed measurements. In this chapter, the KamLAND detector calibrations will be outlined. A detailed description of the detector calibration and the energy scale determination is provided in Appendix A.

3.1 The purposes of the detector calibration

The primary physics goal of the KamLAND detector is to address the LMA solution for the solar neutrino problem using the reactor neutrinos. The detector employs an organic liquid scintillator that is purified. Therefore, the calibration purposes are established as the following:

1. convert the observed waveforms to charge, then to energy deposition; hence, the detector energy response would be found.

2. relate the event timing and charge to positions, and to establish the detector geometry functions, which elucidate the z-axis asymmetry of the detector.

3. optimize the discrimination between signals ($\bar{\nu}_e$ events) and backgrounds (fast neutrons and radioactivity).

4. determine the detection efficiencies as a function of energy and to an accuracy commensurate with the attainable statistical precision, at least in the energy range relevant to reactor anti-neutrino measurements.

In order to carry out the above calibration tasks, we need to build a set of calibration sources and a system to deploy them.

3.2 The deployment system

In the calibration of the KamLAND detector, a variety of radioactive and light flasher sources are deployed in the KamLAND detector to calibrate the detector's response with respect to the different energies and different positions in the detector. A reliable and flexible deployment system is needed to carry out calibration tasks. The deployment system is being built in two phases. The phase 1 system is the z-axis system. Phase 2 is the 4π system, which allows us to deploy the calibration sources anywhere in the entire detector. It is currently under construction.

The z-axis deployment system is currently being utilized in the KamLAND for the calibration deployment. It allows the deployment of various radioactive and LED sources along the z-axis of the detector by attaching a source to a cable, which is then lowered into the detector via a remotely controlled motor. Fig. 3.1 shows a deployment of the calibration source through the chimney into the detector along the z-axis.

The operation of the deployment is through a control hardware which is written by using a LabView software program. The determination of the source positions inside the detector is given by an electronic readout of a shaft encoder that is positioned at the top pulley of the system assembly. The positions determined this way provide an accuracy better than 1 cm. A sealed glovebox is used to encase the deployment assembly. The attachment of sources is accessible through
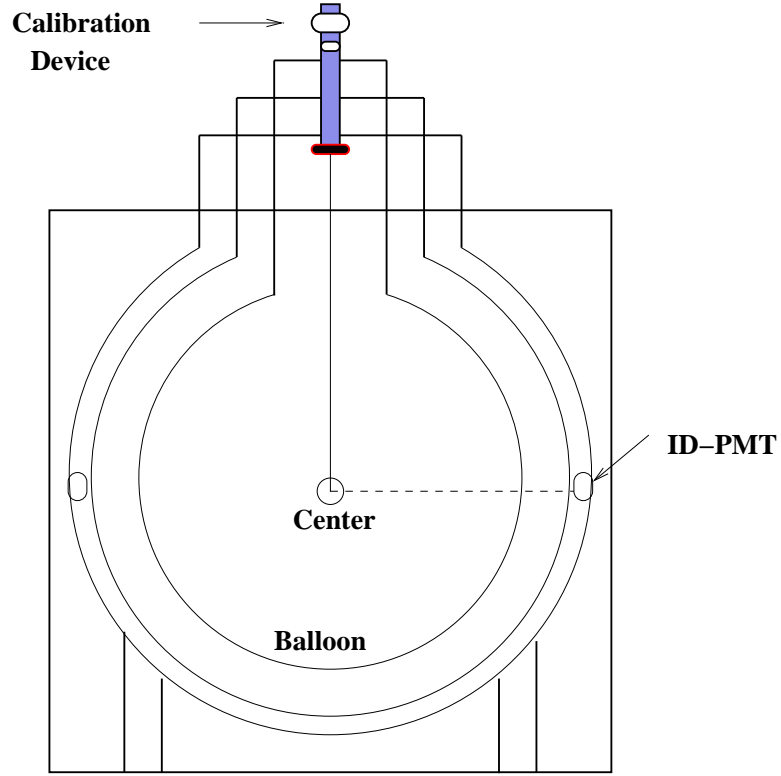
Figure 3.1. A sketch of the calibration source deployment through the chimney into the detector along the z-axis.

the gloveports, which are an airlock system used to load and remove sources.

3.3   Gamma sources

Currently, we have used several gamma sources, spanning the energy range from 0.511 MeV to 7.6 MeV. The sources are ^{68}Ge, ^{65}Zn65, ^{60}Co, and ^{241}Am/Be. The data from such sources are used to measure the energy response as a function of position and to tune the Monte Carlo simulation program, which is used to cal-

culate the positron detection efficiency, gamma energy scale function, beta energy scale function and positron energy scale function. In particular, the data from many positions along the z-axis have been used to establish the energy estimator for the event energy reconstruction with an accuracy of 2% (see Appendix A for details). The source data at the center is used to extract the PMT time constant and charge constant for each event for the vertex reconstruction and the energy reconstruction. The calibrations on a weekly basis have been used to monitor the detector for the PMT gain stability and the scintillator transparency. Fig. 3.2 shows the calibration charge distribution from the ^{60}Co source.
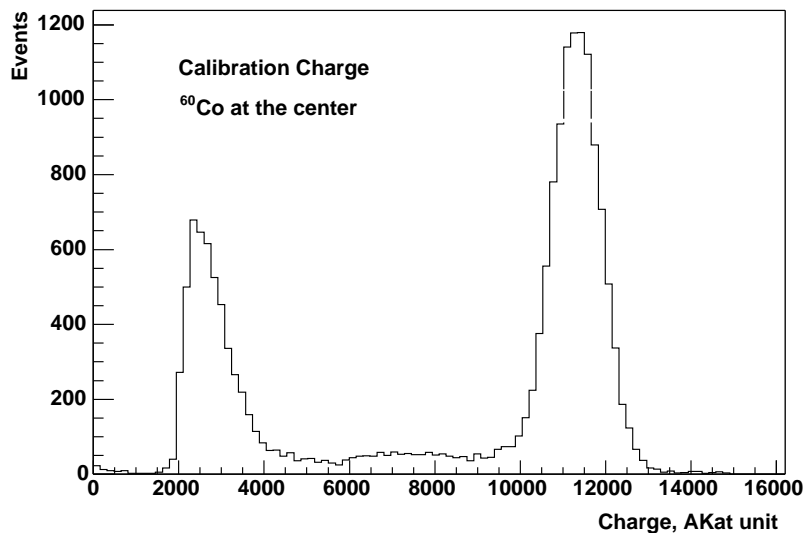
Figure 3.2. Event charge distribution from calibration source 60Co. The unit is AKat (an arbitrary unit).

3.4   Neutron source

^{241}Am/Be is a compound neutron source and gamma source. It emits single neutrons from ^{9}Be$(\alpha, n)^{12}$C* reaction. There are five discrete neutron groups, n_0, n_1, n_2, n_3, n_b, populating the ground state, the 4.43, 7.65, 9.64 MeV levels of the ^{12}C product nucleus and the break-up neutrons. The detailed information about the source can be found in Ref.[47] and Ref.[48]. The neutron data is used to calibrate the neutron detection efficiency. In particular, for the reactor neutrino event, we employ the neutron source for the calibration of the spatial correlation and the time correlation between the prompt event and the delayed event.

3.4.1   Spatial and timing correlation calibration

The signature of inverse beta decay is a delayed coincidence between the delayed events and the prompt events. The coincidence can be performed in the spatial correlation and the timing correlation. However, the spatial correlation and the timing correlation between the prompt events and delayed events should be calibrated to test our hardware. This is done by using ^{241}Am/Be. As can be seen in Fig. 3.3, the prompt events and delayed events are mostly distributed within 2 meters. Of course, this is not a real case for inverse decay events in which the prompt signal is from positron and annihilation gammas. The range of the prompt events from inverse beta decay should be smaller than the prompt events from ^{241}Am/Be. Therefore, Fig. 3.3 only provides the test of hardware for the correlations.
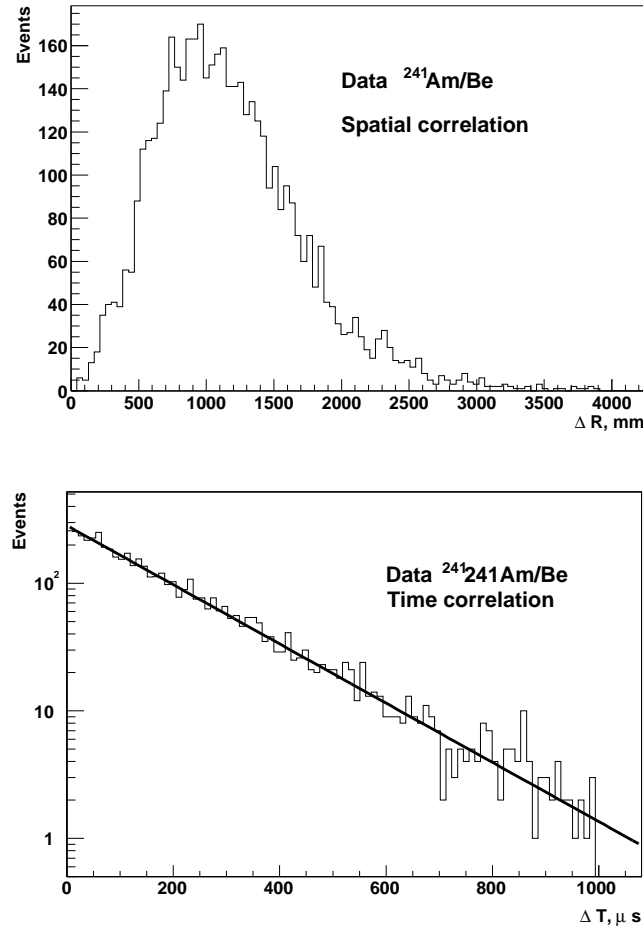
Figure 3.3. The upper plot is the spatial correlation of ^{241}Am/Be events. The distance is in the unit of millimeters. The lower plot shows the time correlation of ^{241}Am/Be events. The solid line is a fit. The fitted time constant is 195.3 μs. The expected time constant is 195.7 μs.

3.4.2 Neutron detection efficiency

^{241}Am/Be with the moderator is also used to study the neutron detection efficiency. As described in the ^{241}Am/Be source calibration section, ^{241}Am/Be is a tagging neutron source, which allows us to study the spatial correlation and the timing correlation for inverse beta decay events. It can also be used to study the neutron detection efficiency. Since kinetic energy of the ^{241}Am/Be neutrons is much higher than inverse beta decay neutrons and the prompt gammas (4.43 MeV gammas) can travel much longer distances than a few MeV positrons can, using the ^{241}Am/Be source to obtain the neutron detection efficiency is an approximation. However, by testing the correlations and the neutron capture as a function of the width of the time window utilizing both the data and the MC, we have obtained a good agreement between the MC and the measurement. We can then generate the positrons and neutrons uniformly in the detector to calculate the neutron detection efficiency for inverse beta decay.

We have studied all available positions along the z-axis using the measurement and the MC. The overall 1% agreement between the MC and the measurement has been achieved. We generate the positron kinetic energy with the end-point of 8 MeV and a neutron kinetic energy of 44 keV on the average in the detector. The neutron detection efficiency is calculated by the formula,

$$\epsilon_n = \epsilon_c \cdot \epsilon_p \cdot \epsilon_\gamma \cdot \epsilon_\tau \cdot \epsilon_r \cdot \epsilon_{FBE} \qquad (3.1)$$

where ϵ_n is the neutron detection efficiency, ϵ_c is the probability that a neutron will not leak out of the fiducial volume, ϵ_p is the probability of capture on proton, ϵ_γ is the delayed 2.225 MeV detection efficiency, ϵ_τ is the probability of capture in the time window, ϵ_r is the spatial correlation efficiency and $\epsilon_{FBE} = 1$ is the electronic detection efficiency. Table 3.1 shows a summary of the neutron detection efficiency using the moderated ^{241}Am/Be source from the MC and the measurement for the source at the center.

Table 3.1. Neutron detection efficiency table for the source at the center.

Sources	0.5μs - 1 ms	0.5 μs - 660 μs
Data ^{241}Am/Be	0.791±0.001%	0.765±0.002%
MC ^{241}Am/Be	0.792±0.001%	0.769±0.001%

For the ^{241}Am/Be source, the criteria of selecting events are:

- the prompt events: $R_{prompt} \leq 3$ meters and $E_{prompt} > 4.4$ MeV

- the delayed events: $R_{delayed} \leq 2$ m and $E_{delayed} > 1.8$ MeV

- the spatial correlation: $\Delta_R \leq 1.6$ m

- the time correlation: $0.5 \ \mu$s$< \Delta_t \leq 1$ ms and $0.5 \ \mu$s$< \Delta_t \leq 660 \ \mu$s

In the simulation of the inverse beta decay, we generate positrons and neutrons uniformly in the fiducial volume of R $\leq$ 5 m. Table 3.2 and Table 3.3 show the neutron detection efficiency for inverse beta decay in the fiducial volume with a radius of 5 m. The prompt space cut is $R_{prompt} \leq 5$ m and the delayed space cut is $R_{delayed} \leq 5.5$ m. The spatial correlation between the prompt event and the delayed event is $\Delta_R \leq 1.6$ m. The vertex resolution is smeared manually. As can be seen in Fig. 3.4, $\epsilon_r = 0.8352$ for $\Delta_R \leq 1.6$ m.

Putting the values in Table 3.2 and Table 3.3 into Equation (3.1), the neutron detection efficiency is $\epsilon_n = 0.8086 \pm 0.0011$ for the time window from 0.5 μ to 1 ms, $\epsilon_n = 0.7833 \pm 0.0014$ for the time window from 0.5 μ to 660 μs. Both results take $\epsilon_r = 0.8352$, assuming that the vertex resolution $\Delta_R = 35$ cm.
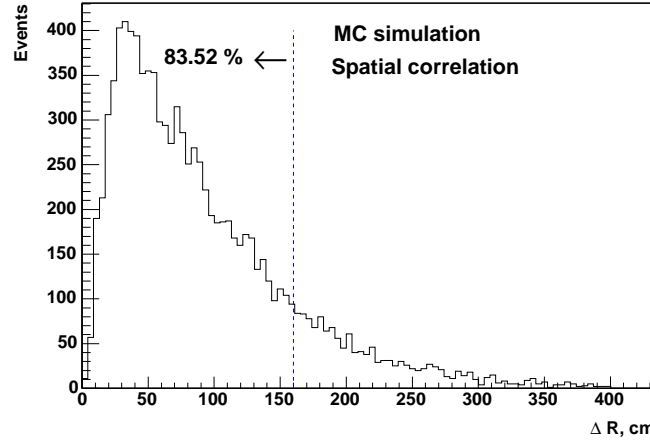
Figure 3.4. Spatial correlation of inverse beta decay events obtained from the MC. The spatial correlation between the prompt events and the delayed events is shown. The distance is in the unit of centimeters.

Table 3.2. Neutron detection efficiency table for the $\Delta_T < 1$ ms obtained from the MC.

ϵ_c	ϵ_p	ϵ_γ	ϵ_τ (0.5 μs - 1 ms)	ϵ_r
0.9955±0.0004	0.9940±0.0004	0.9856±0.0008	0.9927±0.0005	0.8352

Table 3.3. Neutron detection efficiency table for the $\Delta_T < 660\mu$s obtained from the MC.

ϵ_c	ϵ_p	ϵ_γ	ϵ_τ (0.5 μs - 660 μs)	ϵ_r
0.9955±0.0004	0.9940±0.0004	0.9856±0.0008	0.9617±0.001	0.8352

3.5 Light flasher system

The laser emits ultraviolet (UV) light in short (~ 1 ns) pulses. The UV light is absorbed by the scintillator and is then re-emitted by the scintillator with a longer wavelength. Therefore, it is expected that the short light pulses from the laser have the same spectral profile as the scintillation light. Therefore, the laser is used to study single photoelectron gain, PMT timing, PMT gain linearity and scintillator stability. Fig. 3.5 shows the gain linearity of the PMT obtained using the laser. In addition, the LEDs are used to monitor the detector response.
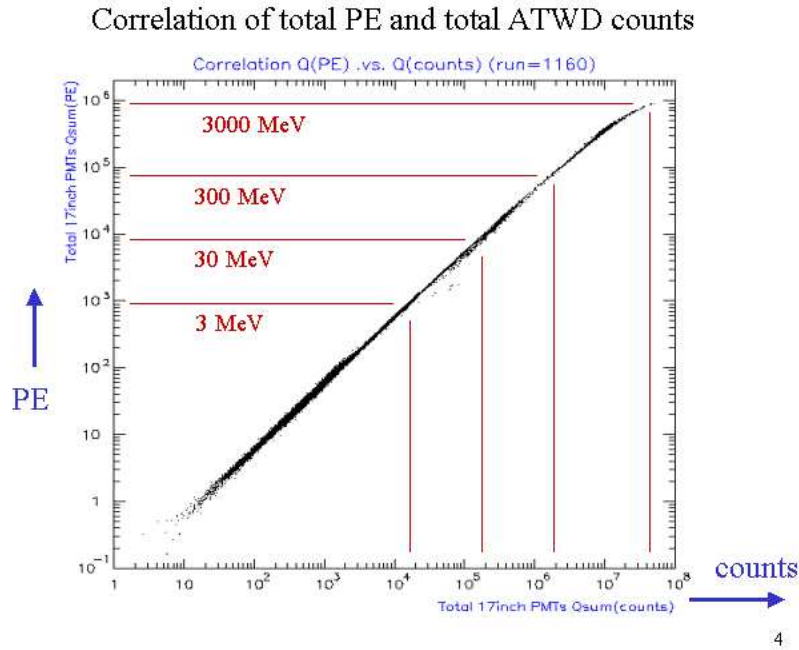
Figure 3.5. PMT gain linearity calibration using the laser. It is plotted as the total number of photoelectrons (PE) versus the total ATWD counts.

3.6 Spallation neutrons as calibration sources

Spallation neutrons and spallation products induced by cosmic-ray muons distribute uniformly everywhere in the detector. Due to the lack of a 4π calibration system, we have used the spallation neutron capture gammas (2.2 MeV) to do the off-axis calibration. The calibration includes the energy scale and vertex. Fig. 3.6 shows the delayed energy distribution obtained using the spallation neutrons in the entire detector. Appendix A contains details.
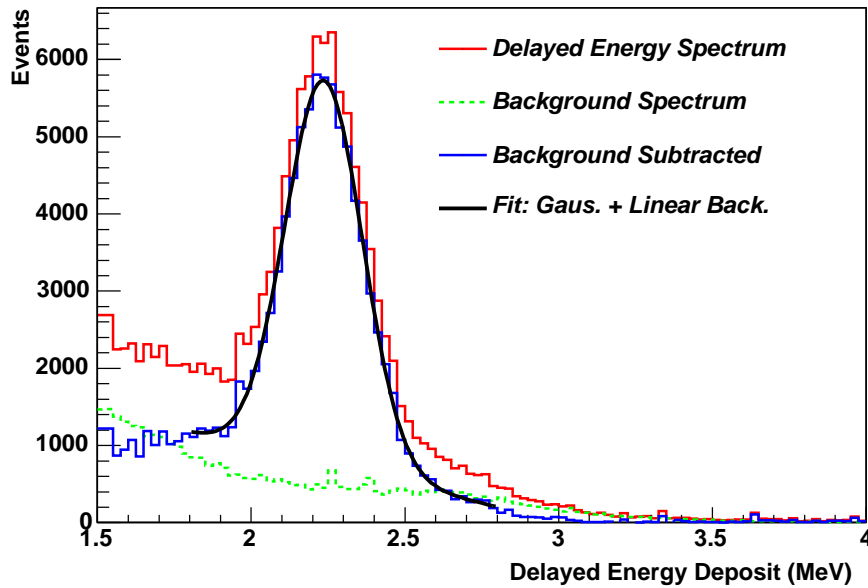
Figure 3.6. The delayed energy spectrum measured using spallation neutrons produced by cosmic-ray muons in the LS. The centroid of the distribution is 2.237 MeV and the width of the distribution is 0.116 MeV. The energy resolution obtained from this distribution is 5.2%. The accuracy of the energy reconstruction is about 0.5%.

3.7   Energy scale

The energy scale for the KamLAND detector is set utilizing the various energy calibration gamma sources, which span the energy range from 0.5 MeV to 7.6 MeV. It is expected that different types of particles have different energy scales. Therefore, the detector energy scale obtained from the gamma sources is used to tune the Monte Carlo, in which the different types of particles are simulated. Once the MC reproduces the calibration data, the positrons and electrons are then simulated for discrete energies. Hence, the energy scale functions for positrons, electrons and gammas are established, respectively. The details can be found in Appendix A.

CHAPTER 4

EVENT RECONSTRUCTION

This chapter briefly describes the event reconstruction algorithms, the results of which will be used in the reduction of the samples of events to a final sample of the neutrino candidates or fast neutron candidates. Events collected in Kam-LAND are divided into two categories, depending on the trigger type. Events with the OD trigger are considered as candidates for muons. Events with the ID trigger are considered as candidates for the neutrino events reduction. Fig. 4.1 shows the data flow for the event reconstruction.

4.1 Event builder

The raw data files are the so-called "kdf" (KamLAND data acquisition) files. The kdf files are taken by the DAQ system according to the trigger conditions that are above the trigger threshold in a certain time window. The kdf data stream consists of the trigger data and the waveforms for each event. These blocks of data are stored in a parallel format. The event builder is used to reconstruct the events using kdf data files and it combines data from different kdf files according to the event timestamps. The event data is stored in a serial format.
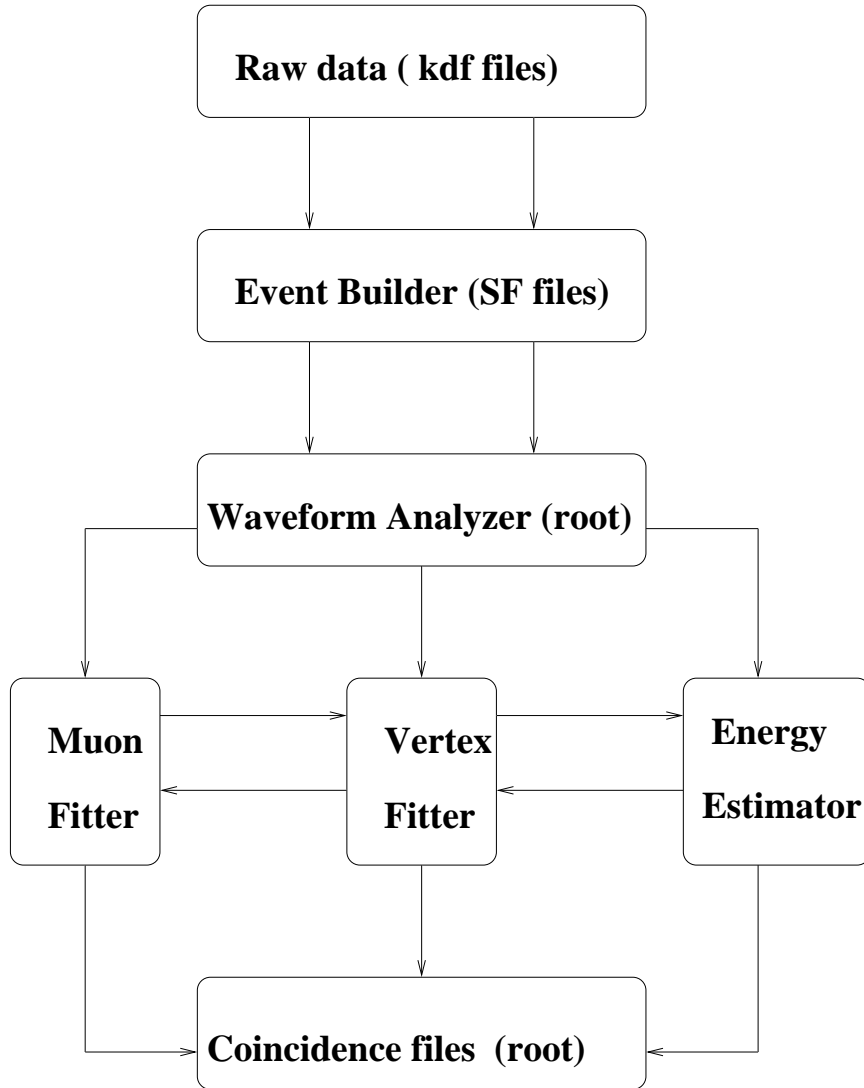
Figure 4.1. The diagram of the event reconstruction.

4.2 Waveform analyzer

The waveforms per event are reconstructed using a tool called the waveform analyzer to extract the charge and the time per PMT. The waveform analyzer

is optimized in such a way that the baseline is properly renormalized, the PMT charge is carefully calculated, the noise and real pulse are well identified. Therefore, the arrival time is determined with an accuracy better than 1 ns. After the waveform analyzer, the TQ (the arrival time and PMT charge) data are stored in Root (data analysis tool) format and are ready to reconstruct the energy and vertex. Fig. 4.2 shows an example for the waveforms reconstruction.
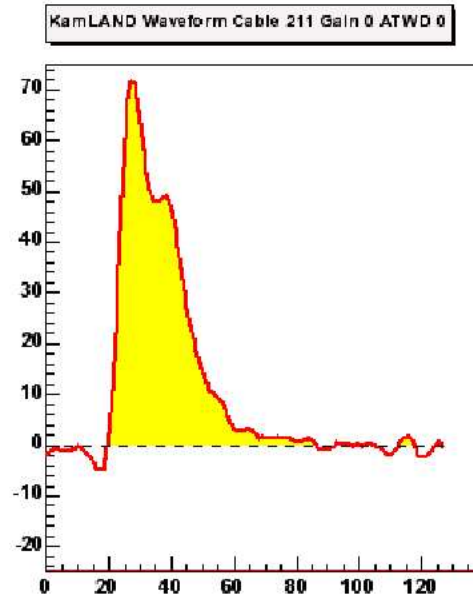
Figure 4.2. Waveform reconstruction. It is plotted after pedestal subtraction and baseline renormalization. The units in both vertical and horizontal axises are arbitrary units.

4.3 Energy estimator

The energy is estimated based on the event charge rather than the number of photoelectrons to minimize the effect of the discriminator threshold. Therefore, it is called the charge-based energy estimator (see Appendix A). To properly estimate the event energy, we have used ^{60}Co as a calibration source to derive the calibration constants. Firstly, the noise charge due to the noise hits per event is well subtracted by applying the time window. Secondly, the light transport in the detector due to the scintillation optical properties (scattering, absorption and reemission) and the detector geometry (PMT acceptance, balloon reflection and shadowing due to the balloon stripes and ropes) are carefully studied utilizing the ^{60}Co calibration data along the z-axis. Finally, the light transport (parameterization functions) and the calibration constants are used to estimate the event energy. The accuracy is carefully examined using various calibration point sources and the 2.225 MeV capture gammas from the spallation neutrons produced by cosmic ray muons in the entire detector. Due to the lack of a 4π calibration system at the moment, the 2.225 MeV gammas from spallation neutrons are well used to study the accuracy of the energy reconstruction. A maximum of 1.4% systematic shift on energy reconstruction has been found by using the above evaluation methods. Employing the various calibration sources (the energy is covered from 0.5 - 7.6 MeV), we have found, in fact, that the energy response is not linear for our detector, which is expected because the scintillation quenching and Cerenkov radiation are energy dependent. After having carefully studied the scintillation quenching and Cerenkov radiation using the Monte Carlo, the conversion functions for different types of particles are then found. The overall systematic error of the energy scale is about 2%.

As an example, Fig. 4.3 shows the energy reconstruction utilizing the energy estimator for ^{60}Co at z = 4.75 m above the center of the detector along the z-axis. Fig. 4.4 shows the accuracy of the energy reconstruction using the ^{60}Co source along the z-axis.

Figure 4.3. Event energy reconstruction at z = 4.75 m above the center of the detector along the z-axis. It is plotted using the ^{60}Co calibration data.

The plot shows:
- Y-axis: Percentage (%), ranging from -10 to 10
- X-axis: Z (meters), ranging from -6 to 6
- Title text: Energy reconstruction (Source Co60)
- Equation: $\dfrac{E - 2.506}{2.506}$
- Legend: Reconstructed with energy estimator

Figure 4.4. The accuracy of the event energy reconstruction along the z-axis. It is plotted using the ^{60}Co calibration data.

4.4 Vertex fitter

The vertex is reconstructed based on both the event timing and the charge, which are called the time-based fitter and charge-based fitter. In the time-based fitter, the PMTs are grouped into diamond-shaped regions in the PMT sphere according to the PMT displacement geometrical feature. The absorption-reemission process (PPO) and elastic scattering (PC) will introduce a time spread in the time distribution of the PMT signal and affect the vertex reconstruction accuracy. However, this scintillation decay time and the PMT jitter are independent of the event position and can be determined by using the isotropic source, like the energy source at the center. The arrival time of ATWD pulse is calculated using the following formula:

$$t_a = t_{event} + t_d + t_f + t_j + t_{tr} + t_c \tag{4.1}$$

where

- t_a is the time of which the ATWD pulse occurs,

- $t_{event} = \text{t}_{trig}$ - t_{offset} is the event time,

- t_d is the decay time of the scintillator,

- t_f is the photon time of flight, and

- t_j is the PMT jitter,

- t_{tr} is the transition time of the photons from the cathode of the PMT to the anode of the PMT,

- t_c is the time that the photons need to propagate through the electronics,

We know that the relative time to the trigger ($t_0 = t_a$ - t_{trig}) can be calculated using the average time of the PMT pulse. The time t_0 per PMT is extracted from

the ^{60}Co calibration data for the source at the center. The photon arrival time per event is determined using the arrival time of the ATWD pulse weighted by charge. The group speed of light is carefully tuned to reflect the fact that the scintillation light consists of direct light, scattered light and reemission light. The different time scales from these three parts of light result in a slower speed of light compared to that of direct light alone. Therefore, the speed of light is calculated based on the so-called "effective refraction index", which averages the effects of the different time scales of light in the speed of light. The accuracy of vertex reconstruction using the time-based fitter is evaluated using various calibration sources along the z-axis at different positions. The systematic shift along the z-axis is about 5 cm and the position resolution is about 10 cm at the gamma energy of 2.225 MeV. Note that the mean free path of the gammas are averaged out in the position resolution.

The charge-based fitter reconstructs the vertex employing the charge and the relative detection efficiency per ATWD channel that are determined utilizing the ^{60}Co calibration data. It calculates χ^2 for the observed charge and the expected charge for a given position. By minimizing the value of χ^2, the vertex is then determined for a given event. The accuracy of vertex reconstruction utilizing the charge-based fitter is similar to that of vertex reconstruction utilizing the time-based fitter.

Fig. 4.5 shows the vertex reconstruction example employing the time-based fitter.

For muons traversing the inner detector, the energy and vertex reconstruction algorithms are the same as described above. Since the accuracy of the energy estimator has not been checked for energies far above 10 MeV and the energy deposit is essentially an extended line segment instead of a point for a muon, the energy and vertex returned by the algorithms are to be interpreted as an effective energy and an effective vertex, respectively.
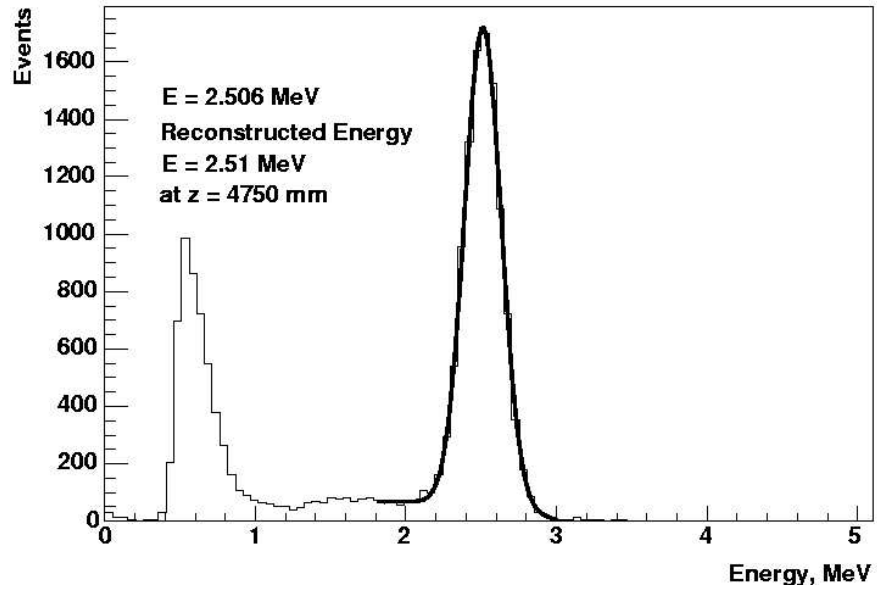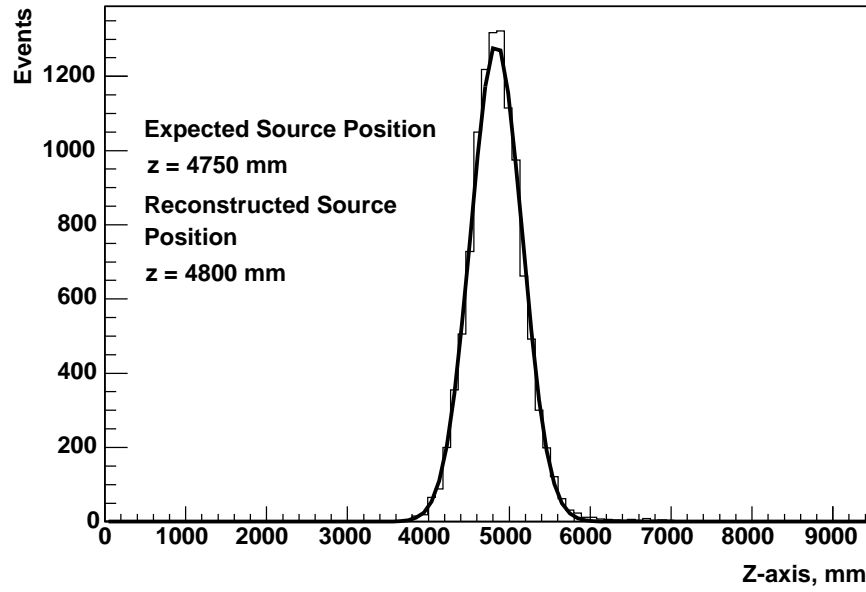
Figure 4.5. Event vertex reconstruction at z = 4.75 m above the center of the detector along the z-axis. It is plotted using the ^{60}Co calibration data. The distance is in the unit of millimeters.
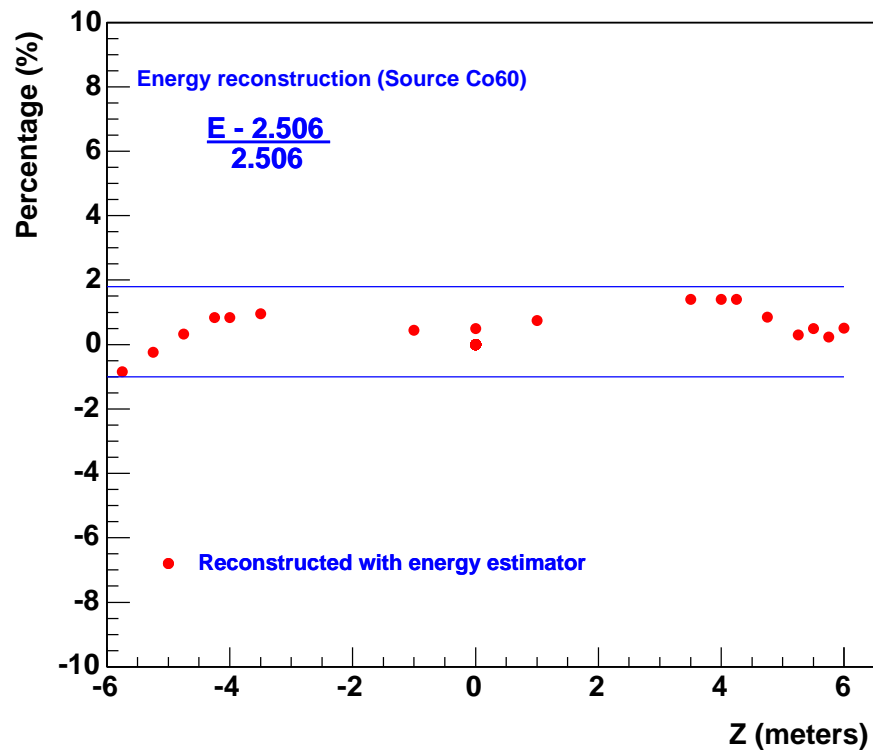
CHAPTER 5

COSMIC-RAY MUONS SIMULATION

Muons crossing the detector produce neutrons. To measure neutron production, it is critical to know the muon rates when muons cross the different media of the detector. A proper Monte Carlo simulation for muon rates when muons transverse the detector volume is necessary.

5.1 Calculation of muon intensity

5.1.1 Calculation of the through-going muon intensity

The relation between muon intensity and depth underground has been measured by several different underground experiments. To figure out the muon intensity at the depth of the KamLAND, the straightforward way is to look at these measured results, fit them with a guessed function, and then calculate muon intensity. The fitted function used here is originally proposed by Groom [49] for deep depths (1000 - 10000 hg/cm^2, 1hg/cm^2 = 100 g/cm^2). It can be expressed as

$$I_v(h) = (I_1 e^{(-h/\lambda_1)} + I_2 e^{(-h/\lambda_2)}) sec^{-1} cm^{-2} sr^{-1} \qquad (5.1)$$

where I$_v(h)$ is the muon intensity at the vertical direction corresponding to the depth of h, I$_1$ = 12.8 × 10^{-6} sec^{-1}cm^{-2}sr^{-1}, I$_2$ = 1.13 × 10^{-6} sec^{-1}cm^{-2}sr^{-1},

$\lambda_1 = 0.366 \times 10^3$ hg/cm^2, $\lambda_2 = 0.794 \times 10^3$ hg/cm^2 and h is the depth. To calculate the through-going muon intensity at the depth of the KamLAND, let $I_{th}(h,\theta)$ denote the through-going muon intensity at the slant depth of h in the direction of zenith angle θ. It can be expressed as [60]

$$I_{th}(h, \theta) = I_v(h)G(h, \theta) \tag{5.2}$$

where $G(h,\theta) = \sec(\theta)$ for the deep underground [60], $h(\theta) = h_0\sec(\theta)$ is the slant depth at zenith θ and $I_v(h)$ is the vertical intensity at depth h, which is expressed in equation (5.1). Putting the expressions of $G(h,\theta)$ and equation (5.1) into equation (5.2, one obtains

$$I_{th}(h, \theta) = (I_1 e^{(-h_0 sec(\theta)/\lambda_1)} + I_2 e^{(-h_0 sec(\theta)/\lambda_2)})sec(\theta) \tag{5.3}$$

where h_0 is the vertical depth in the unit of hg cm^{-2}. For the KamLAND experiment, $h_0 = 2700$ hg/cm^2. Note that this is a flat-earth approximation. Since KamLAND is not below the sea level underground (indeed, it is located inside a mine under a mountain area), the through-going muon flux calculated using this formula is an approximation. According to equation 5.3, the vertical intensity at the vertical depth of the KamLAND is about 4.57×10^{-8}cm^{-2}sr^{-1}s^{-1}. This equation can fit experimental data very well for large depths, from 1000 hg/cm^2 to 10000 hg/cm^2. Fig. 5.1 shows a global fit of muon flux for all underground experiments. Another comparable model in computing the through-going muon flux for large depths is proposed by the LVD experiment [51]. The fitted function is obtained from the best fit of the LVD data as can be seen in Fig. 5.2. At the KamLAND vertical depth, the vertical intensity is obtained to be 4.27×10^{-8}cm^{-2}sr^{-1}s^{-1}. The difference of the muon flux at the depth of the KamLAND between the two models is about 7%.
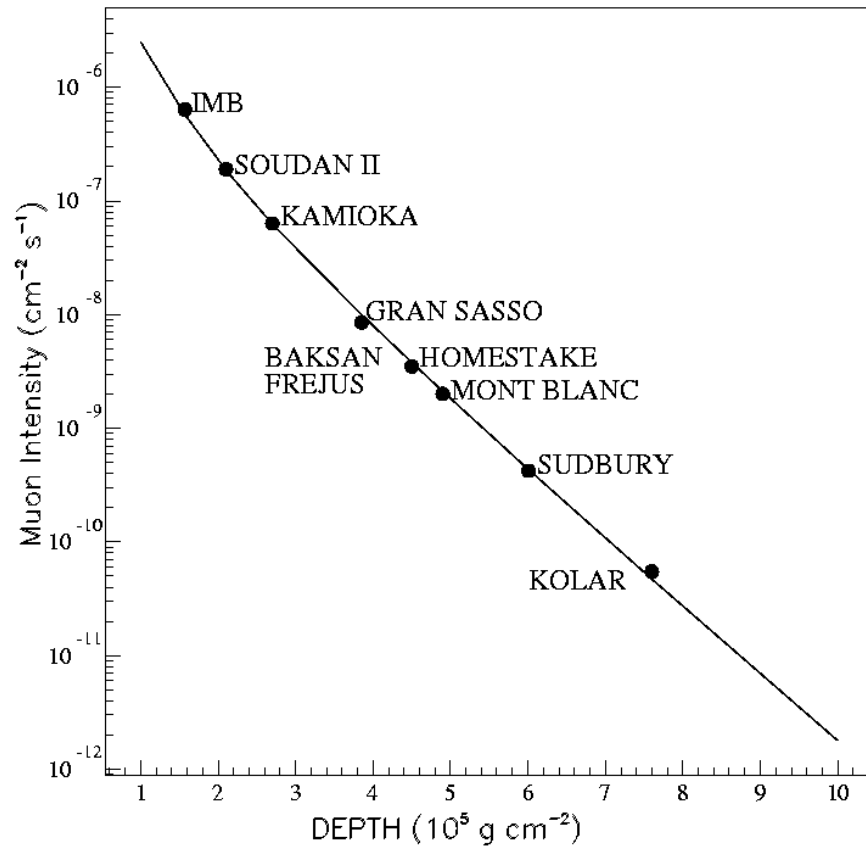
Figure 5.1. The global fit of muon flux for all underground experiments.
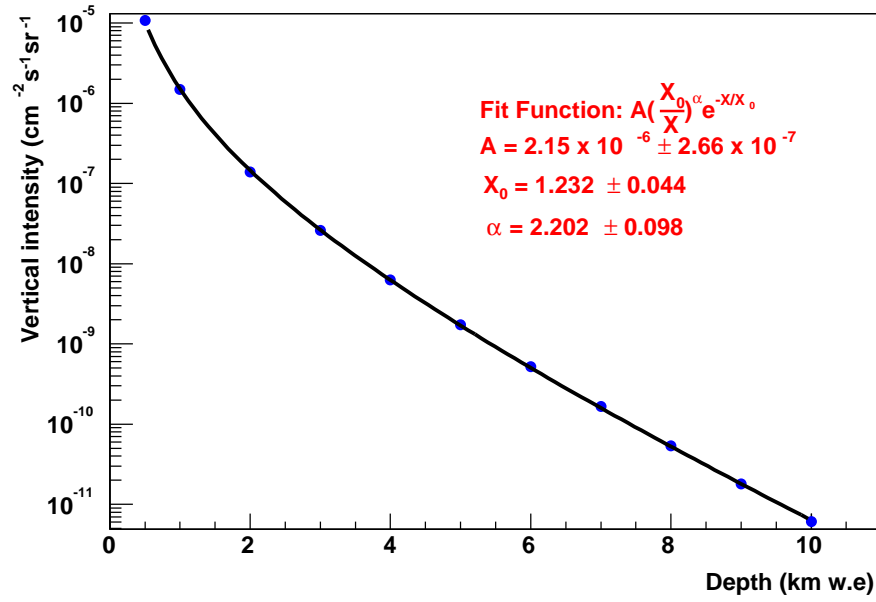
Figure 5.2. The best fit function of muon flux obtained from the LVD data. The data points are the measured muon flux corresponding to each slant depth.

5.1.2   Calculation of the stopping-muon intensity

The stopping-muons are also the source of neutron production. For example, the μ^- capture on carbon produces neutrons. The calculation of the stopping-muon rate is based on the following sources [60]: (1) cosmic-ray muons coming to the end of their range, (2) muons from the decay of slow pions and generated locally by the interactions of fast muons (due to virtual-photo interactions with nuclei), and (3) local muon production by real photons (π_0-decay in the electromagnetic case). It is customary to quote results in terms of the ratio R of stopping muons to through-going muons. The detailed calculation is provided by Cassiday et al. [60]. The total ratio $R(X)$ of stopping-muons to through-muons (vertical direction) at the depth of the KamLAND can be parameterized as [52]

$$R(X) \approx \gamma_\mu \frac{\Delta E}{\epsilon_\mu} \tag{5.4}$$

where $\gamma_\mu = 3.6$ for $E_\mu \geq 1$ TeV [61], $\Delta E \approx \alpha X$, $\alpha = 2.68 \times 10^{-6}$ TeV g^{-1} cm^2 [62] for $E_\mu \geq 1$ TeV [61], X is the effective thickness of different media, which is calculated for different media by a Monte Carlo simulation code (see below), and ϵ_μ = 0.618 TeV [61].

5.1.3   Cosmic-ray muon event simulation

A clear prerequisite to assessing cosmic-ray muon-induced backgrounds for KamLAND is to estimate the muon flux through the experiment setup. A Monte Carlo simulation code has been developed for this purpose. The simulation consists of three parts: (1) generation of the cosmic-ray muon at a surface layer, (2) generation of the cosmic-ray muon angular distribution, and (3) forward tracking through the KamLAND detector. Fig. 5.3 shows the generation of muons at a surface layer and the zenith angle distribution. The generator setup consists of a horizontal disk and the geometry of the KamLAND detector, separated by a
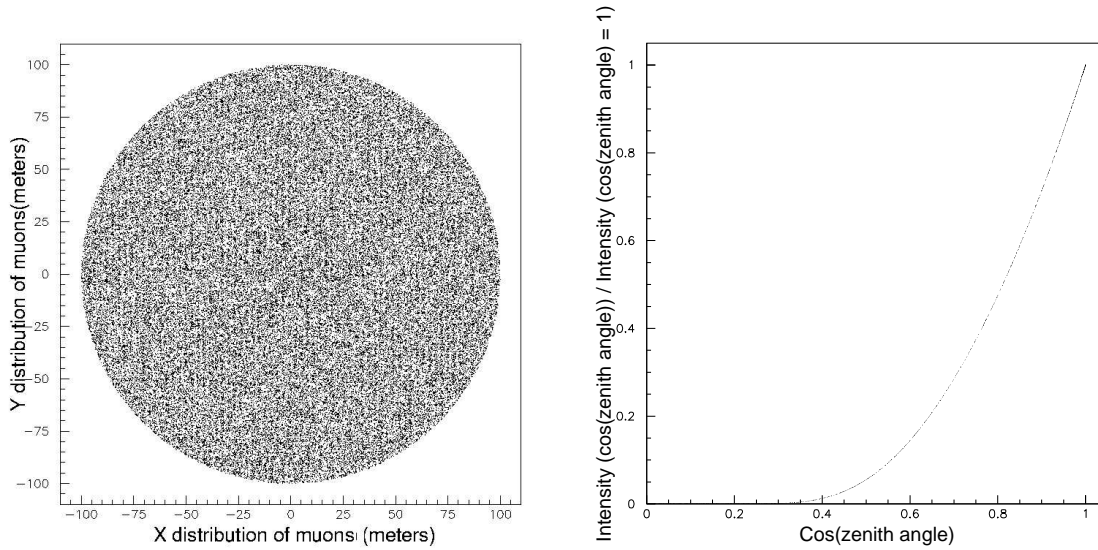
Figure 5.3. Generation of muons at surface layer (the left plot) and the zenith angle distribution of the generated muons (the right plot).

vertical distance $h = 13.5$ meters. The KamLAND detector is centered below the middle of the disk. Tracks are generated on the disk. An event is accepted if a straight track passes through the detector. The muons passing through the scintillator must pass through the other three media (paraffin oil, water and rock). However, the muons passing through rock may not pass through water, or muons passing through water may not traverse paraffin oil and so on. Therefore, it is necessary to distinguish muon tracks for different media. The way to obtain relative acceptance for different media is to use the exact geometrical configuration for each medium. For instance, the scintillator is a sphere with a radius of 6.5 meters with a "chimney" region extending upward from the top. The paraffin oil fills a spherical shell with an inner radius of 6.5 m and an outer radius of 9.0 m

(actually, a small fraction of the volume, which is occupied by two chimneys, is neglected.). Water fills a volume outside the paraffin oil; the outer boundary of this volume is a cylinder with 9.5 meters in radius and 19 meters in height. The effective rock is a 1-meter-thick shell outside water. The neutrons produced more than 1 meter inside rock cannot reach the central detector. With this geometrical setup, the Monte Carlo generator can be coded easily. One "shoots" tracks from a point on the disk toward the different media and calculates the distance in z-direction (DIZ) which satisfies the locus equation with respect to the origin of the coordinate of the generator setup. For example, the scintillator and paraffin oil are spherical loci, and water and rock are cylindrical loci. Table 5.1 shows the results of defined relative acceptance (the ratio of the number of muons crossing different media to the number of muons generated in the disk with a correct angular distribution) and average thickness given in g/cm^2 for different media using this Monte Carlo generator. The densities for rock, water, paraffin oil and the scintillator are 2.7 g/cm^3, 1 g/cm^3, 0.777 g/cm^3 and 0.778 g/cm^3, respectively. The surviving probability factor is the correction for muons stopping in the materials between the disk and different parts of the detector.

Table 5.1. The relative acceptance and effective thickness for different media at the KamLAND.

Medium	X g/cm^2	Relative acceptance	Surviving probability
Rock	1283.85	0.050	1.000
Water	989.60	0.041	0.995
Paraffin oil	503.88	0.025	0.990
Scintillator	667.21	0.015	0.980

5.1.4   Calculation of the total muon intensity

The total muon intensity (through-going and stopping) for any medium can now be calculated once we know the total flux through the disk. This can be computed from

$$I_{th} = 2\pi \int (I_1 e^{(-h_0 sec(\theta)/\lambda_1)} + I_2 e^{(-h_0 sec(\theta)/\lambda_2)}) sec(\theta) sin(\theta) d\theta \qquad (5.5)$$

Integrating over the upper space, $I_{th} = 6.2 \times 10^{-8} cm^{-2} s^{-1}$ (note that $I_{th} = 6.32 \times 10^{-8} cm^{-2} s^{-1}$ is obtained using the measured mountain overburden). From the MC generator, the area of disk is $\bar{A} = 3.14 \times 10^8$ cm^2. Thus, the event rate $R_{disk} = \bar{A} I_{th}$ = 19.3 Hz. We have obtained the same result with our Monte Carlo program. For the different media, the event rate can be calculated as $R_i = (R_{disk}) \times$relative acceptance$\times$surviving probability. The surviving probability represents the probability that muons pass through the material between the disk and the medium of interest. For example, in the case of the scintillator, $R_{tot} = (19.3) \times 0.015 \times 0.98$ = 0.284 Hz. Table 5.2 shows the results for the total muon rate for the different media of the KamLAND. Note that the ratio of stopping-muons to through-going muons $(R(X))$ is used to calculate the stopping-muon rates. This calculation is important to neutron production at KamLAND.

5.2   Calculation of the residual energy of muons

Underground muons are mainly from the interactions of primary cosmic rays with air nuclei in the atmosphere. The production of muons in the atmosphere is via $\pi \rightarrow \mu\nu$ and K $\rightarrow \mu\nu$ decays.

Table 5.2.   The total muon rate calculation for different media of the KamLAND detector.

Medium	Through muon rate (Hz)	Stopping muon rate (Hz)	Total muon rate (Hz)
Rock	0.96	19.2×10^{-3}	0.98
Water	0.79	12.5×10^{-3}	0.80
Paraffin oil	0.473	3.9×10^{-3}	0.48
Scintillator	0.284	3.1×10^{-3}	0.29

5.2.1   Simple Model

The muon energy spectrum at the Earth surface when muon decay is negligible ($E_{\mu0} > 100/cos(\theta)$ GeV) and the curvature of the Earth can be neglected ($\theta < 70^o$) is [52]

$$\frac{dN_\mu}{dE_{\mu0}} \approx \frac{0.14E_{\mu0}^{-2.7}}{cm^2 \ s \ sr \ GeV} \times \{\frac{1}{1+\frac{1.1E_{\mu0}cos(\theta)}{115GeV}} + \frac{0.054}{1+\frac{1.1E_{\mu0}cos(\theta)}{850GeV}}\} \tag{5.6}$$

where the two terms give the contribution of pions and kaons. $E_{\mu0}$ is the muon energy at the surface. Equation (5.6) neglects a small contribution from charm and the heavier flavors which are negligible except at a very high energy. Even within the limit of high energies, an approximate expression of the muon surface energy spectrum has the simple form:

$$\frac{dN_\mu}{dE_{\mu0}} = A \cdot E_{\mu0}^{-\gamma} \tag{5.7}$$

where $\gamma = 3.6$ and A is a constant.

The muon energy spectrum of underground can be derived by taking into account the process of energy loss in the rock. The total muon energy loss can be expressed as a function of the amount of matter traversed:

$$\frac{dE_\mu}{dX} = -(a + bE_\mu) \tag{5.8}$$

where dX is a thin rock slab (g/cm^2), a is the ionization loss and b is the fractional energy loss by the three radiation processes (bremsstrahlung , pair production and photo-nuclear interaction). The quantity $\epsilon = a/b$ is called the critical energy and is defined as the energy below which the ionization energy loss is more important than the radiative energy losses.

To the extent that the mild energy dependence of a and b can be neglected, the general solution of equation (5.8) is:

$$E_\mu = (E_{\mu 0} + \epsilon)e^{-bX} - \epsilon \tag{5.9}$$

where E_μ is the muon energy after crossing the rock slant depth X (g/cm^2). Using the relationship:

$$\frac{dN}{dE_\mu} = [\frac{dN}{dE_{\mu 0}}] \cdot \frac{dE_{\mu 0}}{dE_\mu} = [\frac{dN}{dE_{\mu 0}}]e^{bX} \tag{5.10}$$

and equations (5.7, 5.9, 5.10), we have

$$\frac{dN}{dE_\mu} = Ae^{-bX(\gamma - 1)} \cdot (E_\mu + \epsilon(1 - e^{-bX}))^{-\gamma} \tag{5.11}$$

where A is a constant.

From equation (5.11), the average muon energy at depth X is thus given by:

$$< E_\mu >= \frac{\epsilon(1 - e^{-bX})}{\gamma - 2} \tag{5.12}$$

Using the parameters for the depth of KamLAND: X = 2700 mwe, b = 4 $\times 10^{-6} cm^2/g$ and $\epsilon \approx 540$ GeV [54], we then obtain $< E_\mu >$ = 222 GeV. Note that these parameters are quite sensitive to the chemical composition of the rock, which must be evaluated for the experimental location. However, the chemical composition of the rock at KamLAND is similar to that of the rock in the Ref. [54].

5.2.2 Sophisticated model

A more sophisticated model is used to compute the average muon energy using the slant depth, muon angular distribution and muon flux. We employ the map of

the mountain overburden to calculate the slant depth for a given point (h_0, r, θ, ϕ), where h_0 is the vertical depth at the measured point, r is the distance from the measured point to the detector, θ is the zenith angle and ϕ is the azimuth angle. The slant depth h $= \sqrt{h_0^2 + r^2}$. The number of the measured points are 2880. They are defined on a plane that is formed by a circle. The circle is divided into 72 sectors using 72 rays. Each sector covers 5 degrees between the rays in the 360 degree of azimuth angle. The length of a ray in the circle is 3950 meters. The number of the measured points on each ray is 40. The distance between the points on each ray is 100 meters for 39 positions and 50 meters from the center for the first position . Fig. 5.4 is a sketch of the measured points. The local muon energy
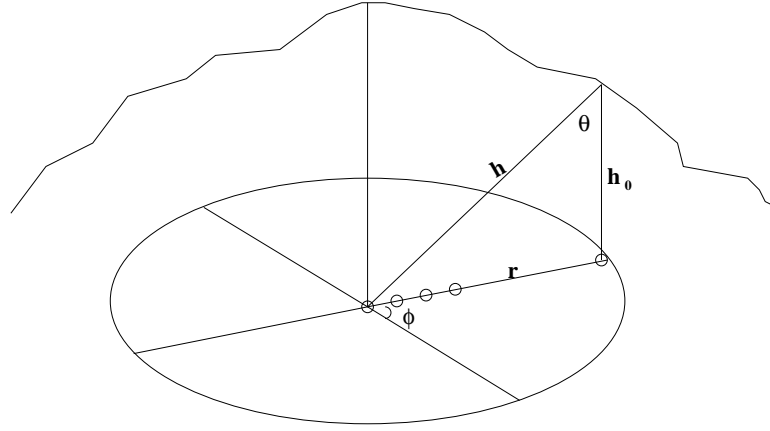
Sketch of the measured points of the mountain overburden

Figure 5.4. Sketch of the measured points of the mountain overburden.

spectrum derived from the above equations is [60]:

$$\frac{dN(E_\mu, h)}{d(E_\mu)} = Ce^{-bh(\gamma-1)}(E_\mu + \epsilon(1 - e^{-bh}))^{-\gamma} \tag{5.13}$$

where $\gamma = 3.6$, b $= 4 \times 10^{-6} \ cm^2/g$, $\epsilon \approx 540$ GeV [54] and C is a normalization constant. Fig. 5.5 shows the local differential muon energy spectrum at the Kam-LAND depth and the depth of 3000 mwe. In the simulation, muons are generated
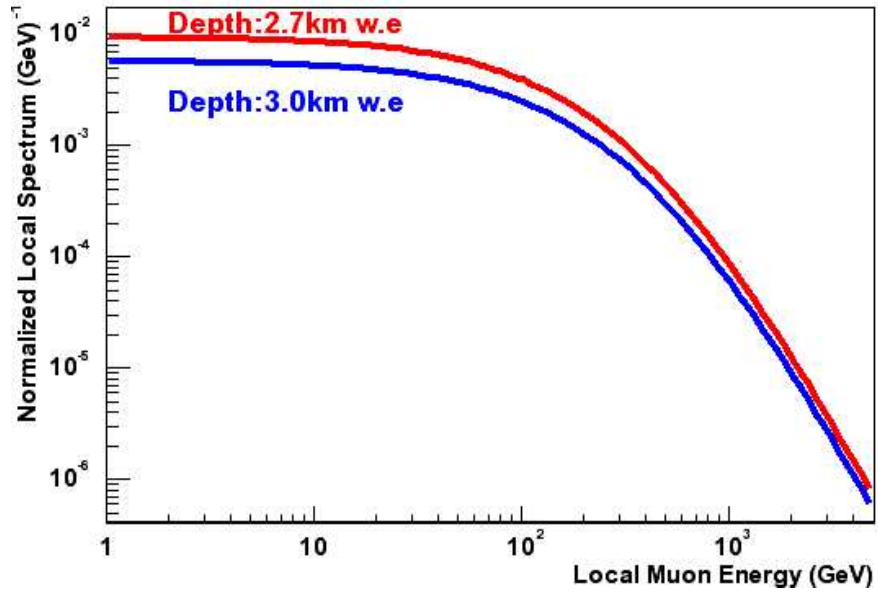
Figure 5.5. Local differential energy spectrum of muons at the KamLAND depth. The areas under the curves are normalized to the vertical muon intensity at each underground depth shown. The depth of 2.7 km.w.e corresponds to the depth of the KamLAND. The depth of 3.0 km.w.e [52] is shown to compare with the depth of the KamLAND.

according to the probability function shown in Fig. 5.5. Each muon energy distribution corresponding to a slant depth has a mean value. Therefore, the average muon energy $(\bar{E}_\mu(h))$ is obtained for each slant depth (2880 points). The muon flux $(I_i(h))$ is calculated by using Groom's model (5.1.1) for each slant depth. The integral range of θ is determined by using two points along a ray of the circle.

There are 5 degree in the integral range between the rays for the azimuth angle. The total muon flux ($I_{tot} = \sum_i I_i(h)$) is the sum of all the measured points. We use the average muon energy weighed by the muon flux at each slant depth to calculate the final average muon energy for the KamLAND:

$$< E_\mu >= \sum_i \bar{E}_{\mu,i}(h)P_i(h), \qquad (5.14)$$

where $P_i(h) = \frac{I_i(h)}{I_{tot}}$ is the weighted factor. Equation 5.14 yields $< E_\mu > = 220$ GeV.

5.2.3 Comparison with other experiments

We have obtained the average muon energy ($\bar{E}_\mu = 220$ GeV) for the depth of the KamLAND using the above three methods. It is compared to other experiments [42, 55, 43]. Fig. 5.6 shows the comparison. As can be seen, our calculation is consistent with the other experiments. The consistency is within 5% obtained using a fitted function. The fitted function has the same form as the equation (5.12). The chemical composition of the rock at KamLAND is similar to that of the chemical composition of the rock in Ref. [42, 55, 43]; the average muon energy is $\bar{E}_\mu = 220 \pm 11$ GeV.
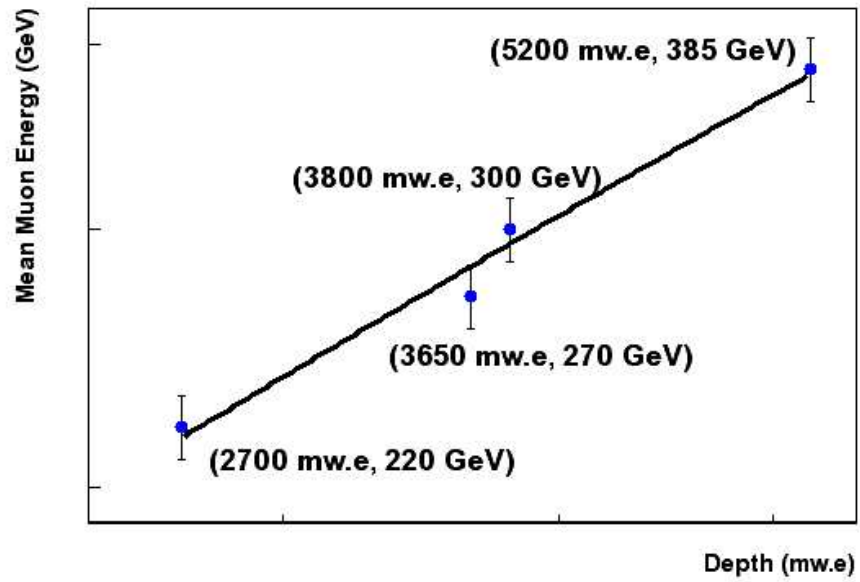
Figure 5.6. The average muon energy comparison. It is plotted using four experimental depths, namely, KamLAND, LVD, MACRO and LSD. The points other than KamLAND in the plot are reported by the LVD, MACRO and LSD experiments. The line is a fit. Both vertical and horizontal axises are in the logarithmic scale.

CHAPTER 6

NEUTRON PRODUCTION

6.1   Neutron production mechanism

Fast neutrons are produced mainly in nuclear and electromagnetic cascades due to δ-electrons, pair production and bremsstrahlung. The processes are:

Spallation process: the nuclear showers are produced due to muon interactions with nuclei via a virtual photon producing a nuclear disintegration, which is the so called muon spallation. Fig. 6.1 shows the lowest-order Feynman diagram for this interaction.

Photo-nuclear interactions: the main process by which neutrons and pions are generated in electromagnetic showers is photo-production. The main contribution to the cross-section for the interaction of γ ray (real photon) with production is from the (γ,n) reaction, which has a giant resonance. In addition to the (γ,n) reaction, the multiple photo-production reactions (γ,in) are also important, where i is an integer. For instance, negative pion capture via a pseudodeuteron in a ^{12}C nucleus is: $\pi^- + d \rightarrow n + n$.

Elastic scattering: The bound neutrons escape nuclei due to muon scattering with such neutrons.

Secondary neutrons: Cascade neutrons are capable of further multiplications

in nuclear reaction. Therefore, the neutrons produced following any of the above processes are important.

Underground neutrinos could also induce muons and neutrons, but because the rate is negligibly small at the depths considered, they are not discussed here. Neutrons can be produced anywhere in the KamLAND cavity. The neutrons are

Figure 6.1. The Feynman diagram of a muon spallation process.

detected as follows:

Fast neutrons generated inside the detector or entering from outside undergo scattering on carbon and hydrogen. In the scintillator, the recoil protons can be detected by their ionization. Eventually the neutrons become thermal and capture on hydrogen: $n + p \rightarrow d + \gamma$ (2.225 MeV). The thermalization time is short.

The mean capture time is $\tau = 203\ \mu s$. The neutron signature employed in this analysis is a delayed coincidence in time between the nuclear recoil or the parent muon track and the capture gamma. Multiple neutron events are identified by the detection of multiple capture γ's.

The criteria for the selection of fast neutron events are:

1. a time correlation between the prompt and the delayed sub-event of $150\ \mu s\ <\ \Delta T\ <\ 660\ \mu s$

2. (a) activity in the OD consistent with a muon or (b) a prompt energy cut of $E_{prompt} > 7.5$ MeV.

cut 2 (b) is used to select events in which a fast neutron was produced by a muon that was not tagged due to the OD inefficiency; the energy cut is set as low as possible and yet it avoids contributions from reactor anti-neutrinos and (α,n) reactions induced by natural radioactivity.

We identify two kinds of backgrounds for the analysis of muon-induced neutrons: (a) accidental coincidences due to radioactivity; and (b) neutrons created by radioactivity contained in the materials surrounding the scintillator. These are mainly due to the spontaneous fission of ^{238}U and (α,n) reactions with elements in the nearby environment.

The contribution of random coincidences to the event sample is estimated from the analysis of a displaced time window at 1.8–2.31 ms. Inspection of the time distribution shows a flat spectrum for the accidentals. The background due to neutrons from natural radioactivity is estimated to be negligible after the prompt energy cut ($E_{prompt} >7.5$ MeV).

6.2 Measurement of neutron production

6.2.1 Neutron production properties

The detected number of neutrons, N_d, can be expressed as:

$$N_d = \frac{N_\mu \cdot X}{C_d} \cdot <n> \cdot \varepsilon_d \cdot f_d \cdot t_d^{daq}. \tag{6.1}$$

N_μ is the number of muons traversing the detector. In terms of the muon crossing rate R_μ and the detector integrated livetime t_{live}, $N_\mu = R_\mu \times t_{live}$. X denotes the effective thickness, in g/cm^2, of the scintillator or the entire detector, depending on the analysis performed. $<n>$ stands for the average neutron production yield per muon per g cm^{-2}. ε_d represents the average neutron detection efficiency. f_d accounts for the lowered detection efficiency when multiple neutron captures (two or more) are coincident on the time scale of the ATWD digitization time. t_d^{daq} is the dimensionless DAQ live time correction due to the 150 μs DAQ deadtime after a muon. Finally C_d is a correction factor to correct for neutrons generated by muons in media other than the scintillator. N_d, N_μ and f_d are determined directly from the data. X, C_d and t_d^{daq} are determined by a data-constrained Monte Carlo simulation. ε_d is obtained solely by Monte Carlo. The determination of each of the quantities on the right hand side of equation (6.1) is described in detail in the following section.

6.2.2 Determination of R_μ, X, C_d, ε_d, f_d, and t_d^{daq}

6.2.2.1 Muon rate and average path length

The muon count N_μ is measured using the segmented OD. We apply the following criteria to select muon candidates: (1) at least one segment has more than 7 PMT hits, or (2) the number of PMT hits in any combination of the four segments is greater than 14.

The time difference between muons is measured using these criteria. We obtained a rate of 0.78 ± 0.05 Hz muons crossing the OD by fitting the time difference distribution between the muons in Fig. 6.2 (dotted line). The fitted function is a single exponential function and the slope is the event rate. The systematic error is from the time variation of the OD inefficiency. Since the muons crossing the ID must cross the OD, the ratio of the coincidence between the OD and the ID events provides the OD inefficiency when a prompt energy cut ($E_{prompt} > 7.5 MeV$) in the ID is applied. This ratio varies from 98.5% (March-October, 2002) to 89% (November-December, 2002).
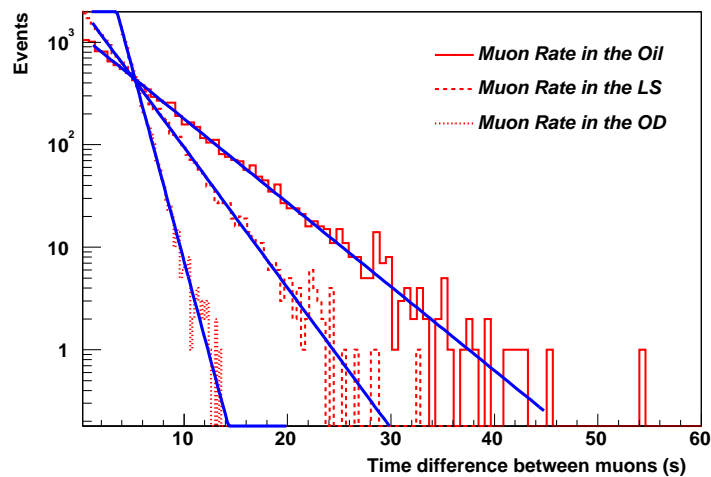
Figure 6.2. The time difference between the muons for which the muons pass through the detector volume. The histograms and corresponding exponential fits correspond to muons passing through the OD ("OD"), muons passing through the OD and buffer oil but not the scintillator ("Oil"), and muons passing through the OD, buffer oil, and the scintillator("LS") with muons crossing different media separately.

Plotting the effective muon energy against the effective vertex for the prompt event, there are three main concentrations of events as can be seen in Fig. 6.3.

The vertex position R_d is given in terms of its radial position normalized to the nominal radius of the central detector. This scenario allows us to separate the muons crossing buffer oil and the scintillator from the muons crossing buffer oil only.
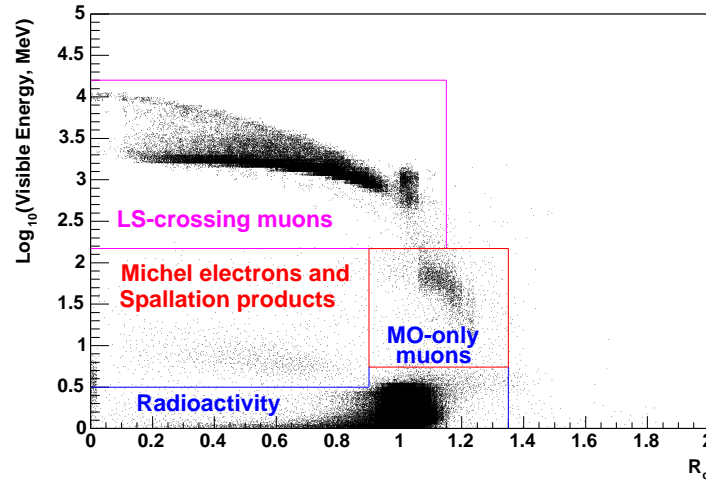
Figure 6.3. The effective energy versus the effective vertex position for the prompt event. Three main concentrations of events can be distinguished. The lowest concentration is due to natural radioactivity. See the text for discussion of the other concentrations.

The muons are identified according to the regions that they pass through. The divisions of muons crossing the ID are:

- **Region I: muons crossing buffer oil and the scintillator (LS-crossing muons)** –effective energy greater than 148 MeV and $R_d < 1.15$.

- **Region II: muons crossing buffer oil only (MO-only muons)**–effective energy greater than 7.5 MeV and less than 148 MeV and $0.9 < R_d < 1.35$.

Therefore, the muon rate is measured separately for the muons crossing region I and the muons crossing region II. The fitted lines in Fig. 6.2 are the measured

time difference distributions between the muons for the cases in which the muons pass through region I and the muons pass through region II. The muon rate is measured using the slope from the fitted single exponential function.

The muon rates obtained from the time-based fitter are 0.28 Hz for the muons crossing region I and 0.19 Hz for the muons crossing region II. With the charge-based fitter, the muon rates are measured to be 0.31 Hz for region I and 0.19 Hz for region II. A 10.7% systematic error for the muon rate in region I is obtained utilizing the difference of the muon rate that is observed between the charge-based vertex fitter and the time-based vertex fitter due to the event vertex reconstruction systematic errors at balloon edge. Adding the muon rate in region I and region II, one obtains 0.47± 0.03 Hz for the muons crossing the ID. The systematic error is obtained by adding the systematic errors of the muon rates that are measured in region I and region II in quadrature.

The measured and simulated results (see Chapter 5 for details) for the muon rates are shown in Table 6.1.

Table 6.1. Muon rate summary.

Medium	Muon rate (data)	Muon rate (MC)
Water	0.78 ± 0.05 Hz	0.80 ± 0.06 Hz
ID	0.47 ± 0.03 Hz	0.48± 0.03 Hz
LS	0.28 ± 0.03 Hz	0.29± 0.02 Hz

Taking the measured muon rates as the final results and adding the systematic errors from the measured muon rate and the simulated muon rate in quadrature as the final systematic error, we obtain $R_\mu^{water} = 0.78 \pm 0.08$ Hz, $R_\mu^{ID} = 0.47 \pm 0.04$ Hz and $R_\mu^{sci} = 0.28 \pm 0.04$ Hz. Note that the quoted muon rates for the different media of the KamLAND detector are single muon rates. The multiple

muon rates are negligible in terms of the depth and geometry of the KamLAND detector.

The average residual energy of muons is computed utilizing a proposed model [60] (see Chapter 5 for details). With a measured mountain overburden, we obtain an average muon energy of about 220 GeV.

The average path length of muons crossing the scintillator is computed by employing both the measurement and the MC. In the measurement, it is measured using the muon energy deposit in the scintillator. The visible muon energy in the LS is estimated utilizing the registered charge per PMT. Since all PMTs are launched for a muon crossing the LS with a spherical symmetry, the visible muon energy depends weakly on the position along the muon track. Therefore, the visible muon energy is accurately reconstructed. An approximate numerical formula for ionization loss of muons in the scintillator is $\frac{dE}{dX} \approx$ -[$1.9 + 0.08 \ln(E_\mu/m_\mu)$] [52], where E_μ is taken to be the mean energy of muons at the KamLAND depth ($\sim$ 220 GeV). A fit to the peak–interpreted as being due to muons losing energy solely by ionization–in Fig. 6.4 yields an average value of X = 849.8 cm $\times$ 0.78 g/cm^3 = 662.8 g/cm^2. In the MC, our calculation gives X = 667.21 g/cm^2 in the scintillator (see Chapter 5 for details). This simulation shows that the average path length in the entire ID is X = 874.01 g/cm^2. Considering the difference between the measurement and the MC as the systematic error, X = 667.21 $\pm$ 4.37 g/cm^2 in the scintillator and X = 874.01 $\pm$ 5.72 g/cm^2 in the entire ID.

6.2.2.2 Neutron detection efficiency

Equation (6.1) contains three factors, ε_d, f_d, and t_d^{daq}, describing the probability that a neutron will be detected. The quantity ε_d is the probability, averaged over the neutrons produced in the muon spallation event and subsequent cascades, that the neutron will capture on a proton and the capture gamma will be fully absorbed in the central detector. The estimation of ε_d is the subject of this sec-
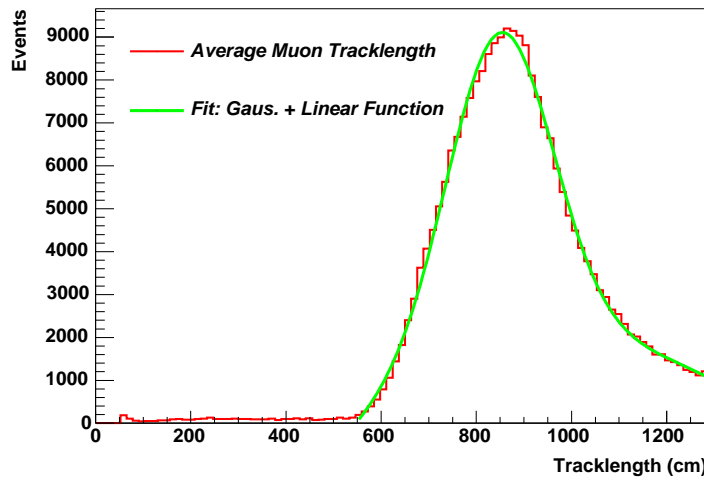
Figure 6.4. Distribution of muon path lengths in the scintillator calculated under the assumption that the peak in muon energy loss is due to ionization.

tion. The estimations of f_d and t_d^{daq}, which incorporate effects of the DAQ and event reconstruction on neutron detection efficiency, are described in the following sections.

To evaluate the detection of neutrons in the central detector, a Monte Carlo simulation code has been developed based on the GEANT. GEANT is a system of detector description and simulation tools. The GEANT program simulates the passage of elementary particles through matter. In view of the applications, the GEANT system allows to: (a) describe an experimental setup by a structure of geometrical volumes; (b) accept events simulated by the Monte Carlo generators; (c) transport particles through the various regions of the setup, taking into account geometrical volume boundaries and physical effects according to the nature of the particles themselves, their interactions with matter and magnetic field; (d) record particle trajectories and the response of the sensitive detectors; (e) visualize the detectors and particle trajectories.

The MC is used to calculate the detection efficiency for the neutrons gener-
ated in different media. In the MC code, the detector geometry, material and
electromagnetic interactions are simulated using the GEANT [72]. Hadronic in-
teractions are simulated by NMTC [73] (Nucleon Meson Transport Code), while
the low energy neutrons transportation code is GCALOR [73]. The initial single
neutrons are produced homogeneously in different media.

The energy spectrum of neutrons produced in muon spallation is uncertain [38,
44, 56, 57, 58]. This is illustrated in Fig. 6.5, which exhibits the energy spectrum
of neutrons from the three models suggested by the experiments and the Monte
Carlo simulation. Among them, Khalchukov's model [56]

$$\frac{dN}{dE} \sim E^{-1.86} \tag{6.2}$$

and LVD's model [43]

$$\frac{dN}{dE} \sim E^{-1.0} \tag{6.3}$$

are obtained by measurements and Wang's model [44]

$$\frac{dN}{dE} \sim \frac{e^{-7E}}{E} + 0.4543e^{-2E} \tag{6.4}$$

is obtained by the FLUKA simulation.

The neutron spectrum following equation (6.2) [56], as measured at acceler-
ators for photo-nuclear interactions, seems to be on a more solid experimental
footing. Hence, the initial single neutron energy spectrum ($E^{-1.86}$) is utilized to
generate neutrons in the MC; the neutron angular distribution (peak forward with
respect to the muon direction) is generated according to Ref. [59]. Since the neu-
tron detection efficiency depends on the assumed neutron energy spectrum, we
have estimated the uncertainty due to the energy spectrum as the following: (1)
we vary the index in a power function E^{-x} over the range $1<x<2$; (2) the energy
spectrum with two exponential functions proposed by Ref. [44] is employed to
evaluate the neutron detection efficiency; (3) the energy spectrum proposed by
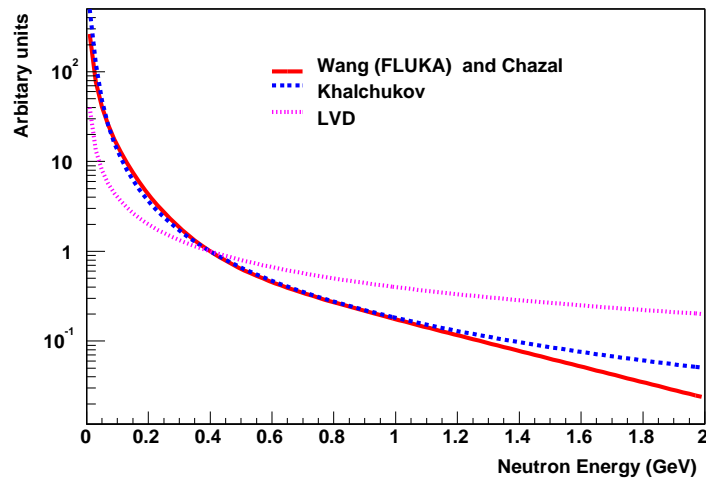
Figure 6.5. The comparison of neutron energy spectra suggested by different models [43, 44, 56]. Note that each model is normalized to unity at 400 MeV.

Ref. [44] harden or soften in the MC; (4) two different methods in the tracking of neutrons are used to computed the neutron detection efficiency. All of these distributions result in similar efficiencies. To determine the neutron detection efficiency, neutron candidates in the MC output are selected by the following criteria:

1. The neutrons capture on protons and the capture gamma is fully absorbed in the central detector volume.

2. The capture time falls in the range of 0.5 μs to 660 μs.

As already mentioned, the neutron detection efficiency is an efficiency averaged over all the neutrons produced in the spallation event and subsequent cascades. Given the uncertainty in the energy and multiplicity distribution of the neutrons produced in the spallation process, we have evaluated the average efficiency for a range of energy and multiplicity distributions. The spread in the efficiencies obtained is used as the basis for estimating the systematic uncertainty in ε_d.

For a particular assumed energy distribution and neutron multiplicity, the average efficiency is evaluated as follows:

$$\varepsilon_d = \frac{N_{tot,d}}{N_{tot,g}} \tag{6.5}$$

where ε_d is the total neutron detection efficiency, $N_{tot,d}$ is the total number of neutrons detected and is counted as

$$N_{tot,d} = N_{1,d} + 2N_{2,d} + 3N_{3,d} + \cdots \tag{6.6}$$

where $N_{1,d}$ is the one-neutron events, $N_{2,d}$ is the two-neutron events, $N_{3,d}$ is the three-neutron events and so forth. $N_{total,g}$ is the total number of neutrons generated. It is defined to be (1) the total number of neutron disappearances in the simulation process and (2) the total number of initial neutrons. Method (1) tracks the total number of neutrons including the secondary neutrons that are produced in the MC and method (2) tracks primary neutrons only. Two methods give a 6% difference in the neutron detection efficiency. Since the initial neutrons are capable of producing secondary neutrons by hadronic interactions (nuclear cascades), the tally of $N_{total,g}$ in method (1) is subtle. Care must be taken to avoid double counting. We have used two different methods to count the number of neutrons that are generated in the MC. The primary method (GEANT method) is to track a neutron until it disappears in the medium and the final state particle is stable, for example, p(n,γ)d and so on. The second method is to count the number of neutrons produced after a hadronic interaction by tracking secondaries, during which if the secondary neutrons are more than 1, then the increment is one less than the number of the total secondary neutrons; if the secondaries are not neutrons but their sub-particles are, then the increment is the number of neutrons that are produced. The two methods give the same number of neutrons that are generated in the MC process.

We describe in turn each energy distribution and multiplicity assumed for estimating ε_d and the corresponding result for the detection efficiency.

For the case of just one neutron initially, the overall detection efficiency is 0.75 ± 0.04 for the neutrons produced in the scintillator and 0.37 ± 0.02 for the neutrons produced in the ID but are detected in the scintillator. The errors are systematic arising from the uncertainty in the energy distribution of the initial neutron. Fig. 6.6 shows how the events are distributed according to the number of detected neutrons.
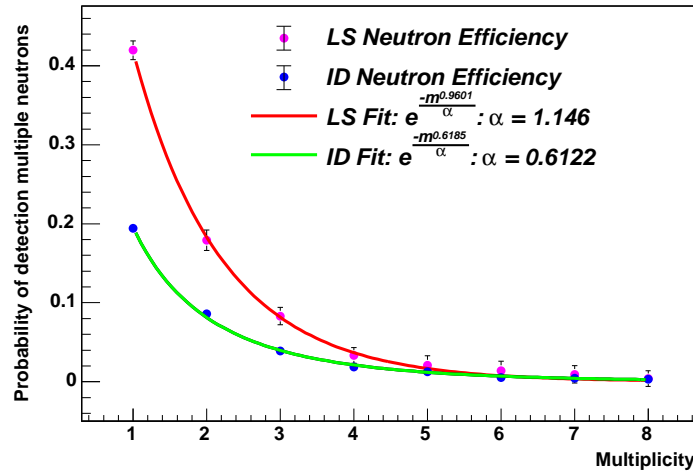
Figure 6.6. Contributions to ε_d broken down according to the number of detected neutrons. Two cases are shown: one for neutrons generated in the scintillator and the other for neutrons generated throughout the entire ID.

The correlation in energy and direction between the two neutrons is unknown. Therefore, two extremes are considered. In the first extreme, the energy for each event is generated according to $E^{-1.86}$. The generated energy is then shared equally between the two neutrons. The two neutrons are also given the same direction. The overall detection efficiency is found to be 0.79 ± 0.04 for the neutrons generated in the scintillator and 0.35 ± 0.02 for the neutrons generated in the ID but are detected in the scintillator. In the second extreme, the energy and direc-

tion of each neutron are generated independently with the energy drawn from the distribution $E^{-1.86}$. For this case, the overall detection efficiency is found to be 0.72 ± 0.04 for the neutrons generated in the scintillator and 0.39 ± 0.02 for the neutrons generated throughout the ID.

At the depth of the KamLAND, production of 3 or more neutrons in the spallation process is plausible. Therefore, we generate 3 neutrons initially, 4 neutrons initially and 5 neutrons initially in the scintillator to inspect the total neutron detection efficiency for each case. The energy of each neutron is generated according to $E^{-1.86}$ with the constraint that the total energy of the neutrons could not exceed the parent virtual photon energy. For each case, the average detection efficiency is found to lie in the same range as the efficiencies for the cases of one neutron initially and two neutrons initially. This is the result expected when the correlations between the initial neutrons are taken to be weak, and consequently simulations of higher neutron multiplicities are unnecessary.

In summary, using the spread of the estimated efficiencies due to different assumptions on the energy dependence and initial multiplicity as a gauge of the systematic error, one obtains $\varepsilon_d = 0.37 \pm 0.04$ for the neutrons generated throughout the entire ID and $\varepsilon_d = 0.75 \pm 0.08$ for the neutrons generated in the scintillator.

6.2.2.3   Evaluation of f_d

If two or more neutrons are captured within the ATWD digitization time, the capture energy for the second, third, fourth, fifth, $\cdots$ neutron would be distorted because both ATWDs for some PMTs would be busy digitizing the waveforms due to the capture of the first neutron and the prompt event or thermal noise. Consequently, the second and subsequent captures may not be detected due to distortions in the reconstructed energy. The magnitude of this effect may be estimated using the PMT hit distribution (NsumMax) because the number of hits is not affected by digitization.

Figures 6.7 and 6.8 show the delayed energy and the delayed NsumMax distributions before and after the subtraction of accidentals.
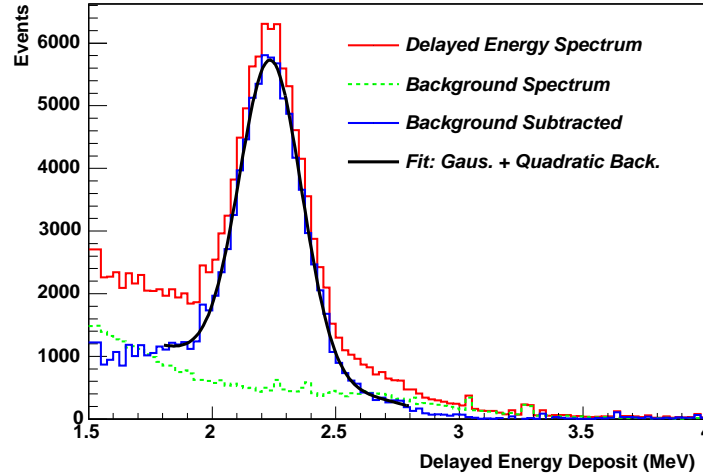
Figure 6.7. This plot shows the delayed energy distribution. The solid line is the whole spectrum and the dashed line is the accidental coincidence distribution. The delayed energy distribution after the accidental coincidence subtraction is also shown in this plot. The fitted function is a Gaussian plus quadratic background function.

The contribution of an accidental background to these distributions is obtained by applying the neutron selection criteria except with the delayed coincidence window offset to 1.8–2.31 ms. After the subtraction of accidentals, the NsumMax distribution shows a clean peak with position and width as expected for detection of 2.225 MeV gammas throughout the central detector volume. A clear peak is also evident in the delayed energy distribution but has a low–energy tail due to capture while both ATWDs are digitizing previous captures.

To measure the impact of the distortion on the detection efficiency, the ratio of the number of events under the Gaussian in the delayed energy distribution to the number of events in the NsumMax distribution is calculated (prior to this
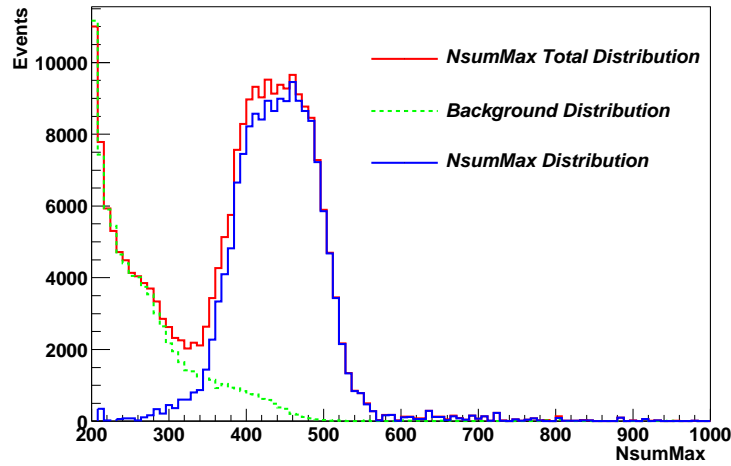
Figure 6.8. The NsumMax distribution measured from the trigger data, where the solid line is the whole distribution and the dashed line is the distribution for accidentals. The NsumMax distribution measured after the accidentals subtraction is also shown.

calculation, an additional cut of $300 < \text{NsumMax} < 600$ is applied to further suppress background.). The result of the calculation is $f_d = 0.40 \pm 0.02$. The systematic error is estimated from the spread in the results of the different methods used to calculate N_d (see below).

6.2.2.4   The correction factor C_d

In equation (6.1), C_d represents a correction factor for the detected neutrons generated outside the medium of interest. The calculation of C_d for the ID is based on the detection of the neutrons created mainly in the water. For the liquid scintillator, the calculation of C_d is based on the detection of the neutrons created mainly in the oil. Both the MC and the measurements are employed for the C_d evaluation.

In the MC, assume that the neutron production rate is 2.26×10^{-4} neutrons

per muon per g/cm^2 and use the Monte Carlo to estimate the detection efficiencies for the neutrons generated in the water or in the oil. About 2832 ± 200 neutrons are predicted for the case in which the LS is the target. For the case in which the ID is the target, the prediction is about 1130 ± 80. The total measured number of neutrons in the LS is about 66400. Therefore, C_d^{mc} is 0.96±0.003 for the LS and 0.983±0.001 for the ID. The stated uncertainties are mainly due to the uncertainties of the neutron detection efficiency.

In the measurement, the prompt energy cut is applied to estimate C_d^{data} for different targets. For the LS target, the MC shows that the visible energy of the detected neutrons that are produced in the buffer oil, water and rock is less than 500 MeV. In the case in which the ID is the target, the visible energy of the detected number of neutrons that are produced in the water and rock is less than 148 MeV based on the MC. As is shown in Fig. 6.9, the prompt energy cuts are chosen according to the prompt energy deposition features of the prompt events that correspond to the different origins based on the MC.
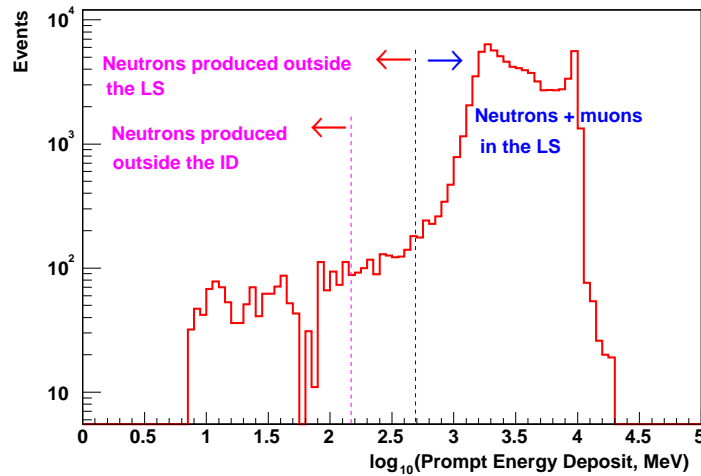
Figure 6.9. The prompt energy deposition in the LS.

Apart from the prompt energy deposition features, the neutrons that are produced in different regions that are measured in the LS have the following radial distribution features: (1) the neutrons uniformly distribute in the LS if they are produced there; (2) the neutrons distribute mostly along the balloon edge if they are produced outside the LS. Fig. 6.10 shows the neutron radial distribution when they are produced in the LS.
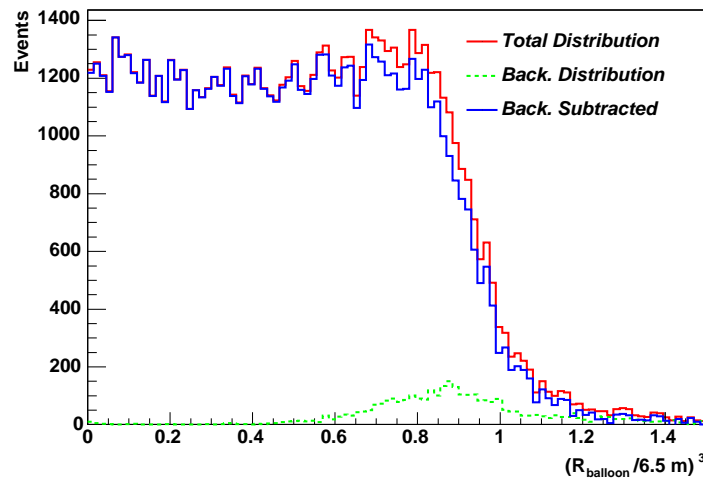
Figure 6.10. R^3 vertex distribution of 2.2 MeV neutron capture γ's. The energy cut is $E_{prompt} > 500$ MeV.

Since there is no veto requirement, the neutrons that are generated outside the LS measured this way are all neutrons that are produced outside the LS regardless of the veto. Fig. 6.11 shows the distribution of the neutrons that are produced outside the LS but are detected in the LS. The measured number of neutrons is about 2930 $\pm$ 235. Fig. 6.12 shows the distribution of the neutrons that are produced outside the buffer oil but are detected in the LS. About 1210 $\pm$ 100 are detected in this case.

The systematic error for the case in which the LS is the target is mainly the
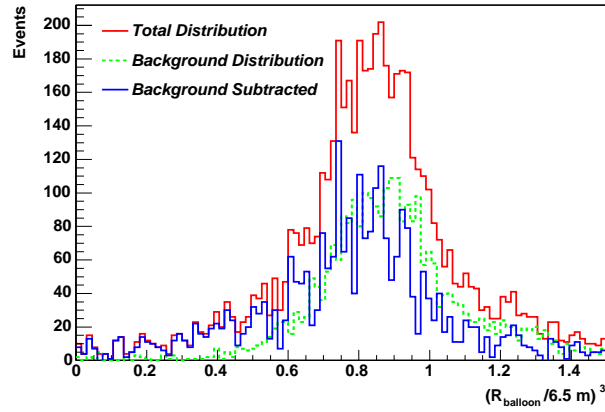
Figure 6.11. R^3 vertex distribution of 2.2 MeV neutron capture γ's. The prompt energy cut is $E_{prompt} < 500$ MeV at which the neutrons produced in the LS ($E_{prompt} = E_\mu + E_{p-recoil} > 500$ MeV) are largely excluded.

Figure 6.12. R^3 vertex distribution of 2.2 MeV neutron capture γ's. The prompt energy cut is $E_{prompt} < 148$ MeV at which the neutrons that are created in the buffer oil are largely excluded.

contamination of the neutrons that are produced in the LS. The systematic error for the case in which the ID is the target is mainly the contamination of the neu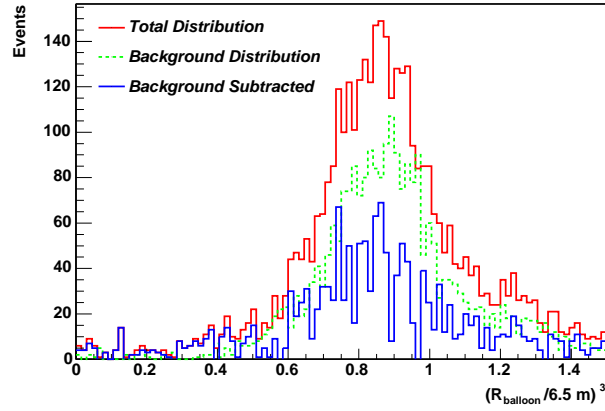trons that are produced in the buffer oil. The contaminations for both cases are obtained by varying the energy cuts. As is expected, most such neutrons distribute along the balloon edge. Using the measured total number of neutrons in the LS ($N_d = 66400$), C_d^{data} is then calculated to be 0.96 ± 0.004 for the case in which the LS is the target. In the case in which the ID is the target, C_d^{data} is 0.982 ± 0.002.

The measured results confirm the MC results. The final results are: (1) $C_d = 0.96 \pm 0.005$ for the case in which the LS is the target; (2) $C_d = 0.983 \pm 0.002$ for the case in which the ID is the target. The stated uncertainties are obtained by adding the uncertainty in the MC and the uncertainty in the measurement in quadrature.

6.2.2.5   DAQ live time correction

Muons release about 2 GeV energy, on average, as they traverse the scintillator. 2 GeV energy corresponds to about 6×10^5 photoelectrons. It takes the DAQ about 150 μs to digest such an event. This is evident in Fig. 6.13, which shows the time difference between the prompt event and the delayed event where the prompt event is due to a muon crossing the detector. To account for the neutrons captured within 150 μs after the muon but not detected, we use the neutron capture time distribution. This distribution is obtained from the spallation neutron measurement and the MC, which has been checked against our neutron source (moderated Am–Be) calibration data. Fig. 6.14 displays the capture probability as a function of time as measured and simulated for the Am–Be source.

The mean capture time for the Am-Be neutrons is about 195.3 ± 2.5 μs from data and 195.7 ± 2.6 μs from the MC. The capture probability between 150 μs to 1 ms is about 0.46 ± 0.005, which means in equation (6.1), $t_d^{daq} = 0.46 \pm$
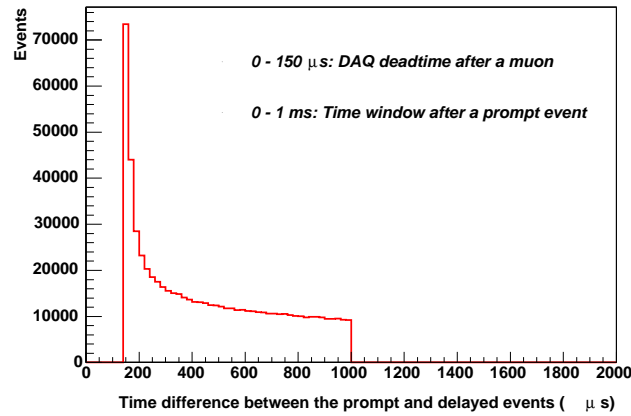
Figure 6.13. The time difference between the prompt event and the delayed event after muons. The decrease in events at 1 ms is due to the end of the 1 ms delayed coincidence window opened with a lower trigger threshold after a prompt event trigger.
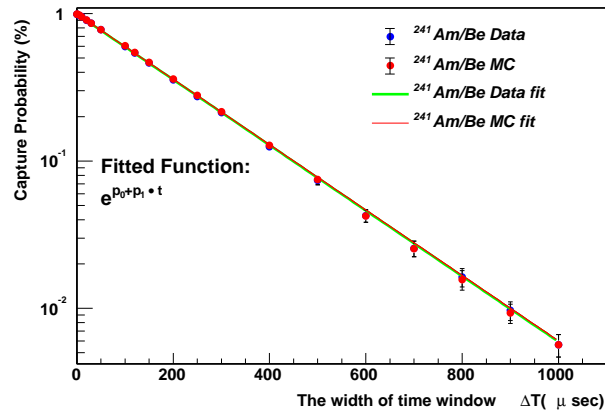
Figure 6.14. The neutron capture probability as a function of time obtained from the Am-Be calibration data and Monte Carlo simulation.

0.005. Note that the capture time from a moderated Am-Be source is expected

to be smaller than a "naked" Am-Be source because the moderator has a higher density (0.92 g/cm^3) than the liquid scintillator. (0.78 g/cm^3). This can be confirmed by comparing the capture time distributions for the Am–Be neutrons and the neutrons produced by muons. Fig. 6.15 shows the capture time distribution obtained for the detected neutrons due to spallation. The capture time is 202.9 ± 4.1 μs. The fast neutron capture time obtained from the MC is 201.0 ± 2.8 μs. Taking the average of capture time from the spallation neutron measurement and the MC to calculate the capture probability and adding the systematic errors obtained from the spallation neutron measurement and the MC in quadrature, one obtains 0.48 ± 0.01.
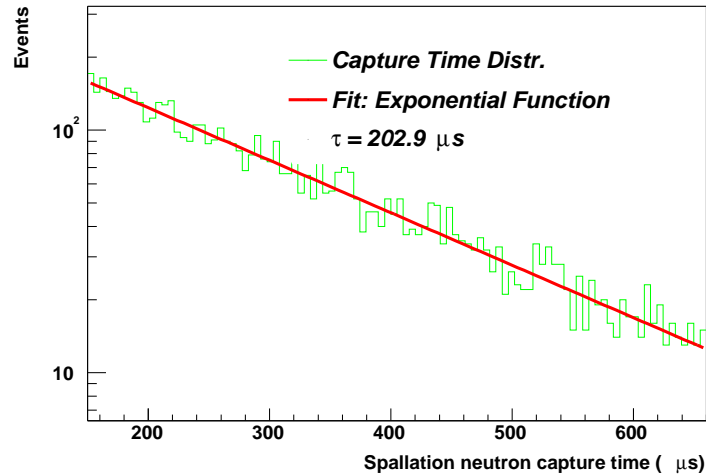
Figure 6.15. Distribution of the spallation neutron capture times.

6.2.2.6   The number of detected neutrons N_d

Three methods are used to determine the value of N_d. The primary method uses the entire detector volume with the events tagged by muons and the contribution from coincidences estimated and subtracted using an offset delayed coinci-

dence window. The number of detected neutrons is equal to the number of events under the Gaussian in Figure 6.7.

The second method utilizes the entire detector without requiring a muon tag (cut 2 (b)). Fig. 6.16 shows the resulting delayed energy spectrum in this approach before and after subtracting of the accidental background. As for the primary method, the number of detected neutrons is equal to the number of events under the fitted Gaussian function.
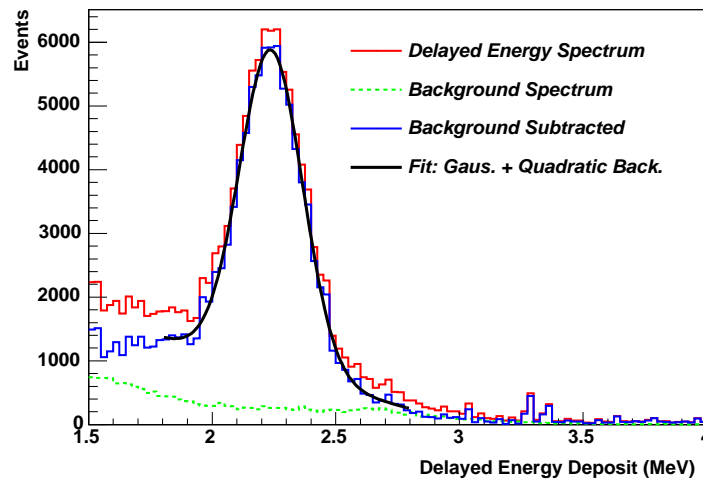
Figure 6.16. The delayed energy spectrum measured for the entire detector with no requirement of a muon tag.

The third method employs a smaller fiducial volume (5.5 m radius) but is otherwise identical to the primary method. Fig. 6.17 shows the result. The number of detected neutrons is scaled to the entire central detector assuming that the fast neutrons are uniformly distributed in the detector. The results from these three methods are consistent with each other to about 5%. Table 6.2 shows the results.

Using the measured number of neutrons from the primary method as the final
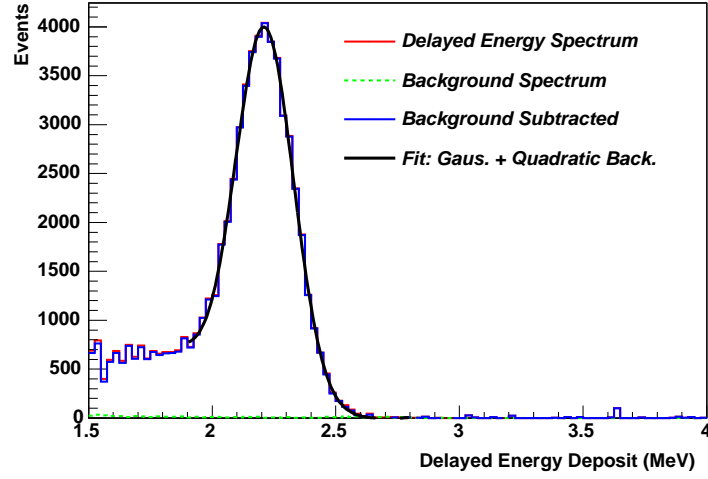
Figure 6.17. The delayed energy spectrum obtained applying a 5.5 m (radius) fiducial volume cut.

Table 6.2. Summary of the detected neutrons using three methods.

Method	The detected neutrons
Primary	66400
Second	68400
Third	65100

result, we obtain $N_d = 66400 \pm 3300$, where the error is dominantly systematic and is based on the differences in results between the three methods. Note that f_d is also measured utilizing these three methods. This uncertainty is consistent with the OD inefficiency. The systematic error on the f_d value in the above section is the spread in the results of these three methods.

6.2.2.7 Neutron production rate

We can now use equation (6.1) to compute the neutron production rate. For the case in which the scintillator is the target and the case in which the entire ID is the target, Table 6.3 and Table 6.4, respectively, list the values for the variables in equation (6.1) and the corresponding systematic errors. Note that N_d is the

Table 6.3. Neutron production rate summary for the LS.

Variables	Estimated value	Systematic uncertainty
N_d	66400	3300
R_μ^{sci} (Hz)	0.28	0.04
$X(g/cm^2)$	667.2	4.4
C_d	0.96	0.005
t_d^{daq}	0.48	0.01
$t_{live}(days)$	118.09	0.1
f_d	0.40	0.02
ε_d	0.75	0.08
$<n>(n/\mu g\ cm^{-2})$	2.32×10^{-4}	0.45×10^{-4}

Table 6.4. Neutron production rate summary for the ID.

Variables	Estimated value	Systematic uncertainty
N_d	66400	3300
R_μ^{ID} (Hz)	0.47	0.04
$X(g/cm^2)$	874.01	5.72
C_d	0.983	0.002
t_d^{daq}	0.48	0.01
$t_{live}(days)$	118.09	0.1
f_d	0.40	0.02
ε_d	0.37	0.04
$<n>(n/\mu g\ cm^{-2})$	2.20×10^{-4}	0.34×10^{-4}

sum of all the detected neutrons. $N_\mu = R_\mu \times t_{live} \times 86400$ is the total number of

muons. Taking the average of the two values as the central value and the average of the systematic errors as the final systematic error we obtain our final result for the neutron production at the KamLAND depth,

$$< n >= (2.26 \pm 0.01(stat.) \pm 0.40(syst.)) \times 10^{-4} n/\mu \ g \ cm^{-2} \qquad (6.7)$$

where 0.01 is the statistic error obtained using 66400 neutrons.

6.2.2.8 Neutron multiplicity

The neutron multiplicity is measured using the NsumMax data. For each event in which the first capture occurred between 150–660 μs after the muon, the number of times that NsumMax fell in the range of 300–600 hits is counted over an interval of 3 ms; this count is taken to be the neutron multiplicity. To estimate the background contribution, the same procedure is carried out for the events in which the first neutron capture candidate occurred 1.8–2.31 ms after the muon. Fig. 6.18 shows the multiplicity distributions before and after the background subtraction. The mean multiplicity is 3. The visible multiplicity is reduced from the actual multiplicity by the average neutron detection efficiency ε_d and the factor t_d^{daq} due to the 150 μs deadtime following each muon. Correcting the visible multiplicity distribution for these effects, the distribution in Fig. 6.19 is obtained with an average multiplicity of 8±1 neutrons. The error comes from the uncertainty in the DAQ live time correction and detection efficiency correction.

The multiplicity can be fitted using the following function:

$$\frac{dN}{dM} = P_0(e^{-P_1 M} + P_2 e^{-P_3 M} + P_4 e^{-P_5 M}) \qquad (6.8)$$

where $P_0 = 332\pm61$ is a normalization constant, $P_1 = 0.0015\pm0.0003$, $P_2 = 41\pm8$, $P_3 = 0.0083\pm0.0015$, $P_4 = 792\pm145$ and $P_5 = 0.3354\pm0.0614$ are all related to the muon energy, and M is the multiplicity. This function has the same form as a proposed universal empirical parameterization in Ref. [44], but has an additional term to account for the multiplicity between 100 and 200.
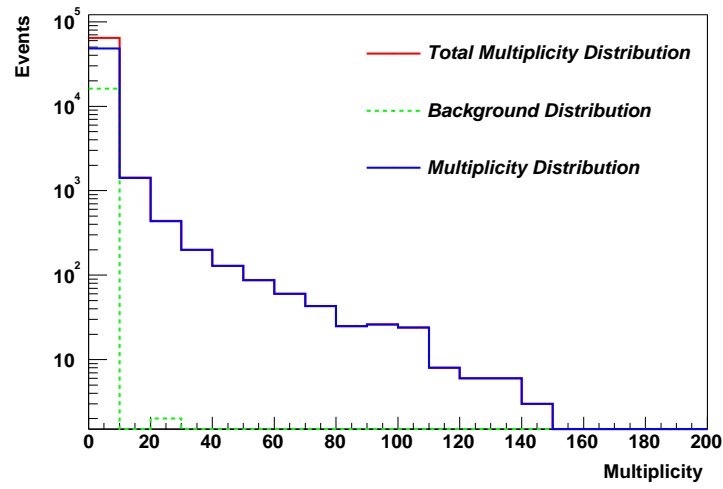
Figure 6.18. Visible neutron multiplicity.
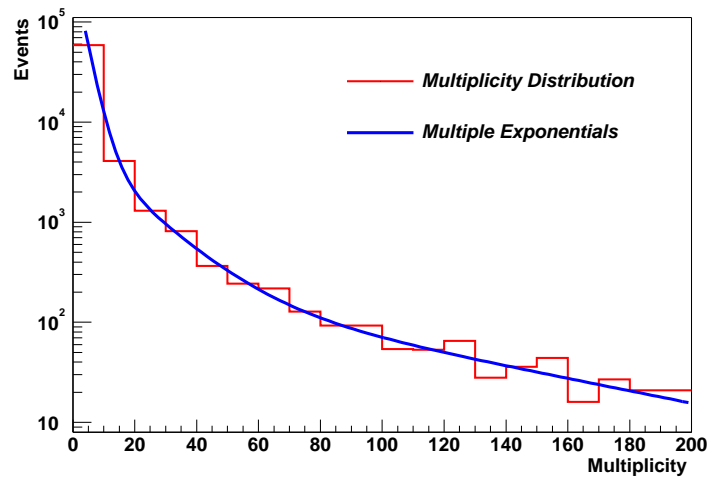
Figure 6.19. Neutron multiplicity after correcting for 150 μs deadtime and neutron detection efficiency. The solid curve is a fit. See text for its description.

We observe from our data that 2% of the muons crossing the detector produce neutrons. It is computed using the observed muons that are associated with the production of neutrons divide by the total number of muons that cross the LS.

The contribution to neutron multiplicity due to the neutron-induced nuclear cascades is large at large depths. Fig. 6.20 shows the neutron multiplicity as a function of the neutron kinetic energy in the nuclear cascades. It implies that the nuclear cascades following muon spallation dominate neutron production at large depths.
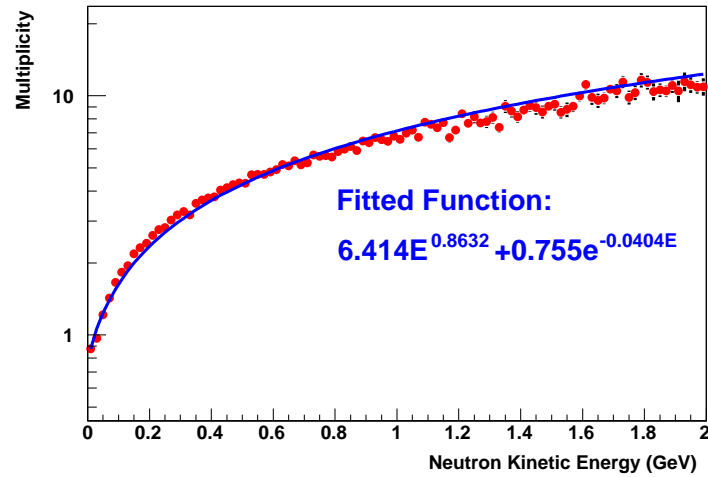
Figure 6.20. Neutron multiplicity as a function of the neutron kinetic energy obtained from the MC.

6.2.3 Comparison with results from other experiments

6.2.3.1 Neutron production rate at different depths

Eight measurements, including the new measurement from KamLAND, of the total neutron production rate are shown in Fig. 6.21 versus the respective depths at which the measurements were made. The range of depths is shallow to deep underground. At more than 2000 mwe, there exist now three measurements, with KamLAND's result falling between the other two. The solid curve is a power law fit to all the measurements.
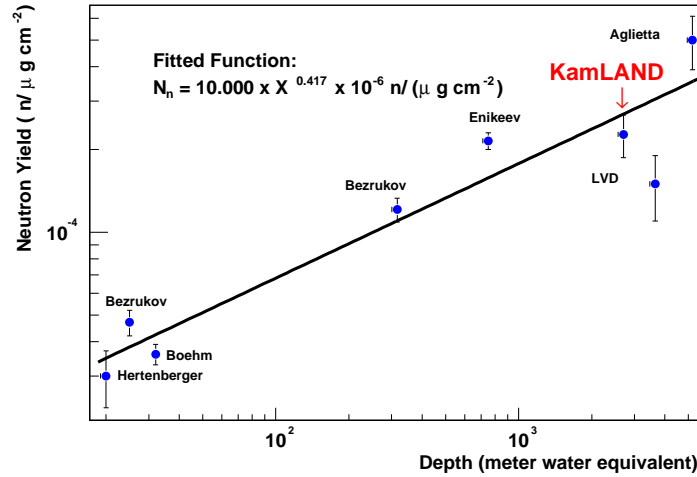
Figure 6.21. Measurements of the average neutron production rate by cosmic muons versus depths in mwe. The solid curve is the fit of a power law function to the measurements.

6.2.3.2 Neutron production rate as a function of muon energy

To directly compare the experimental results with the Monte Carlo calculations performed in Ref. [44] and Ref. [70], we also report a global fit for neutron production rate in terms of mean local muon energy E_μ for the eight existing

measurements. For experiments which did not provide the mean muon energy, we used the experimental depth and the muon energy loss rate [62] to estimate the mean muon energy. As is shown in Fig. 6.22, the fitted function is $N_n = (5.84 \pm 0.89) \times E_\mu^{0.71\pm0.04} \times 10^{-6}$ n/ μ g cm^{-2}. This function is consistent with a power law model suggested by Ref. [44] and Ref. [56]. The KamLAND result agrees with Wang $et\ al.$'s FLUKA [44] and Kudryavtsev $et\ al$'s FLUKA [70] simulation prediction $(2.24 \times 10^{-4} n/\mu\ g\ cm^{-2})$.
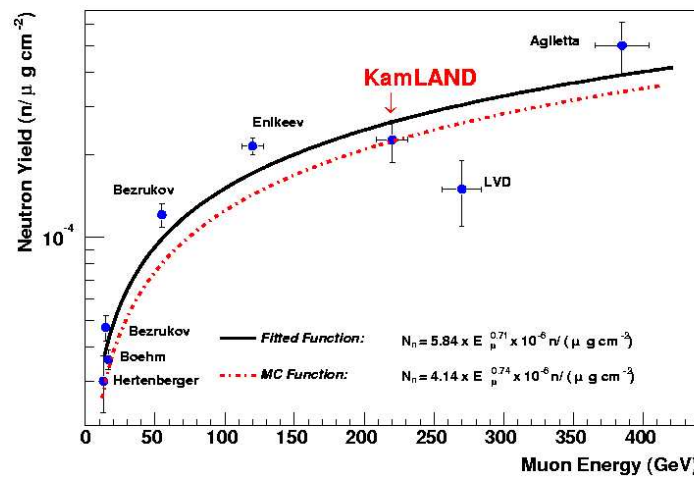
Figure 6.22. Measurements of the average neutron production rate versus the mean muon energy. The solid curve is a fit of a power law function to the measurements and the dashed curve is a prediction described in the text.

6.2.3.3 Neutron multiplicity

The average neutron multiplicity per muon spallation event measured by Kam-LAND, namely 8±1, is compared with the FLUKA simulation [44], in which an average multiplicity of 7 is reported for a muon energy of 385 GeV. Also, as is already noted, the multiplicity distribution can be well–parameterized by a

functional form suggested by the FLUKA simulation. Clearly, still more measurements are desirable to understand the full neutron multiplicity with respect to the neutron energy.

6.3 Summary

We have measured the properties of the neutron production by cosmic muons at the depth of the KamLAND (2700 mwe). The average number of neutrons produced per muon per g/cm^2 is $2.26 \pm 0.01 \pm 0.40 \times 10^{-4} n/\mu \ g \ cm^{-2}$. Per spallating muon, the neutron multiplicity distribution has been measured with the average multiplicity determined to be 8 ± 1. Our measurement of the average neutron production rate is in agreement with the rough trend established by previous measurements and in good agreement with a calculation using the FLUKA simulation package. The FLUKA expectation for the multiplicity distribution is also in agreement with our measurement. We find that about 2% of muons spallate neutrons when they pass through the scintillator.

APPENDIX A

DETECTOR ENERGY CALIBRATION

Proper energy calibration of the KamLAND detector is an important and difficult task. The detector energy response depends on the understanding of the following:

- The PMT efficiency, gain factor and gain stability

- The hardware threshold

- The light transport in the scintillator and the buffer oil

- The scintillation quenching effect and $\check{C}$erenkov light yield

First, each PMT is required to have a proper calibration on a constant time basis to ensure that the recorded time and charge are well understood. A constant monitoring of the PMT provides information on the PMT gain stability. Second, a constant calibration is required to understand the detector components, such as the scintillator and the buffer oil. A continuous measurement of the scintillator and the buffer oil transparency is needed to properly correct the light collection for long-term variations in the scintillator and the buffer oil quality. Third, calibrations are responsible for converting the event charge into the energy. Therefore, different well known energy sources are required to conduct such experiments. Finally, a calibration data-constrained Monte Carlo simulation is needed to understand the scintillation quenching effect and the $\check{C}$erenkov light yield. Hence, the energy scale functions for different types of particles can be obtained.

The general energy calibration goal is to understand the detector response with respect to the different energy sources. Current calibrations are done with

the z-axis deployment. Off-axis calibration is accessible via fast neutrons capture gamma (2.225 MeV) induced by cosmic ray muons. In this appendix, the energy calibration is detailed.

A.1   PMT gain calibration

A.1.1   The calibration sources

Several radioactive gamma sources have been used for the detector energy calibration. The energy ranges from 1.022 MeV to 7.65 MeV. The sources are ^{68}Ge, ^{65}Zn, ^{60}Co, ^{241}Am/Be. Table A.1 shows the source properties for the energy calibration.

Table A.1. The various gamma sources for the energy calibration.

Nuclide	Half-life	Gamma Energy	Emission Probability
^{68}Ge	0.742 y	0.511 MeV	90%
		0.511 MeV	90%
^{65}Zn	0.65 y	1.116 MeV	50%
^{60}Co	5.271 y	1.172 MeV	100%
		1.333 MeV	100%
^{241}Am/Be	432.7y	4.43 MeV	66.7%
		7.65 MeV	∼2%
		2.225 MeV	100%

In the inverse beta neutron decay reaction: $\bar{\nu}_e + \mathrm{p} \rightarrow \mathrm{e}^+ + \mathrm{n}$, there are two critical calibration points:

1. The minimum energy from a positron is two annihilation gammas. The total energy from two annihilation gammas is 1.022 MeV. It would be good to have an energy source to do the calibration at this energy level. ^{68}Ge is a positron source and the end-point positron energy is about 1.9 MeV. With

a sealed thin stainless steel housing, the positron will be annihilated inside the source volume and two annihilation gammas will then come out.

2. Since the highest geo-neutrino visible energy is about 2.49 MeV, the reactor neutrino analysis threshold can be chosen to be 2.6 MeV. Therefore, ^{60}Co provides 2.506 MeV per event to the reactor neutrino threshold calibration for a full absorption detector.

^{241}Am/Be is a compound source in which there are three gamma energies that can be used for the energy calibration. Two prompt gammas (4.43 MeV and 7.65 MeV) are from the ^{9}Be(α,n)^{12}C reaction. The gamma with 2.225 MeV energy is from neutrons capture on proton. The detailed discussion about this source can be referred to Ref.[47] and Ref.[48].

A.1.2 The PMT calibration and the calibration charge

The event builder is used to reconstruct events for the registered time and charge per PMT based on the trigger conditions and a certain time window. After the event building, the time and the charge per waveform are analyzed using a waveform analyzer (discussed in Chapter 4), in which the time and the charge are properly extracted from each waveform. To obtain the event charge (visible energy) according to the number of PMT hits, the random coincidence hits due to the PMT noise have to be subtracted from the total charge. The procedures to obtain the visible energy per event are:

1. The number of background hits is estimated as

$$N_{bg} = (t_3 - t_2) \times \frac{N_{hit}(t_1 : t_2) + N_{hit}(t_3 : t_4)}{(t_2 - t_1) + (t_4 - t_3)} \qquad (\text{A.1})$$

where $N_{hit}(t_i : t_j)$ is number of hit-PMT in the time interval between t_i and t_j, and t is as shown in Fig. A.1, t_1 and t_4 are the beginning and the

end of the event, and t_2 and t_3 are the limits of the time window under consideration.

2. Effective hits N_{eff}

$$N_{eff} = N_{hit}(t_2 : t_3) - N_{bg} \qquad (\text{A.2})$$

3. Effective charge Q_{eff}

$$Q_{eff} = Q_{tot}(t_2 : t_3) - \frac{Q_{tot}(t_2 : t_3)}{N_{hit}(t_2 : t_3)} \times N_{bg} \qquad (\text{A.3})$$

Fig. A.1 shows the determination of the effective hits and the effective charge using the time window. After the noise charge subtraction, the calibration charge (effective charge) is obtained. Since ^{60}Co outputs the energy of 2.506 MeV per event which corresponds to about 560 PMTs hits and is far above global trigger threshold of 200 PMTs hits for the prompt events, we choose ^{60}Co as a calibration standard source to estimate the event energy. Fig. A.2 shows the mean charge distribution per PMT per channel from the ^{60}Co source at the center of the detector. Note that we use the arbitrary charge unit AKat (American KamLAND analysis tool). The mean charge per PMT per channel can be used to estimate the SPE gain. For the purpose of studying the light transport, the mean charge plays a very important role.

It is also important to examine the uniformity of the PMT response: the gain uniformity and the relative detection efficiency (the detection efficiency of PMT per event) uniformity. In Fig. A.2, we see that the gain uniformity is about 14.1% for the ATWD-A and 13.2% for the ATWD-B. The gain difference between the ATWD-A and the ATWD-B is in an expected range due to the slightly different gain factor between the two channels. Fig. A.3 shows the mean charge difference between the two channels. The average difference is about 1%, which is acceptable. The relative detection efficiency uniformity is expected to be much better than the
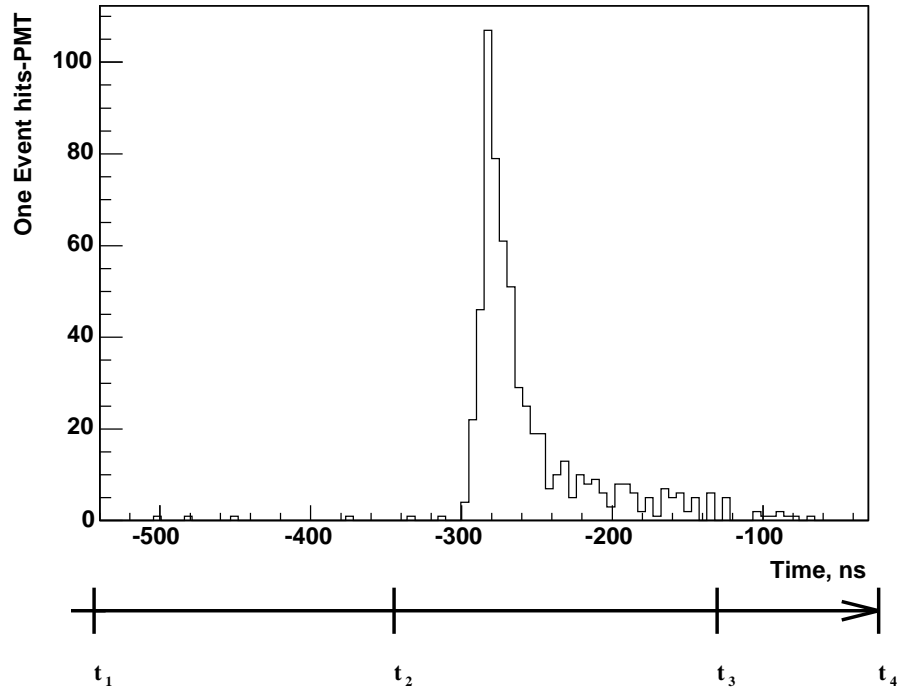
Figure A.1. The timing distribution of hits-PMTs in one event. The time, which is the horizontal axis, is the relative timing of each hit-PMT obtained from the ATWD data.

gain uniformity. Fig A.4 displays the uniformity of the ATWD-A and the ATWD-B. In Fig. A.4, we obtain a 5.4% of uniformity for the relative detection efficiency for the ATWD-A and a 5.2% of uniformity for the relative detection efficiency for the ATWD-B. The difference between the ATWD-A and the ATWD-B is shown in Fig. A.5. As can be seen, the difference is negligible as expected.

Figure A.2. The mean charge distribution per PMT per channel. The upper plot shows the mean charge distribution from the ATWD-A and the lower plot shows the same from the ATWD-B.
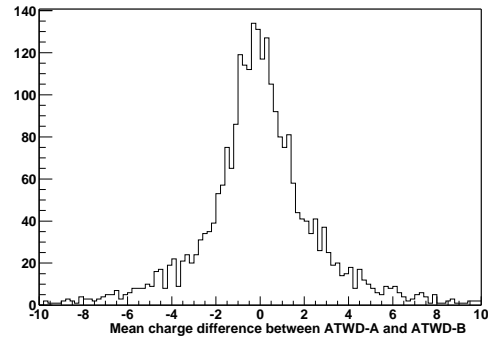
Figure A.3. The mean charge difference between the two channels.
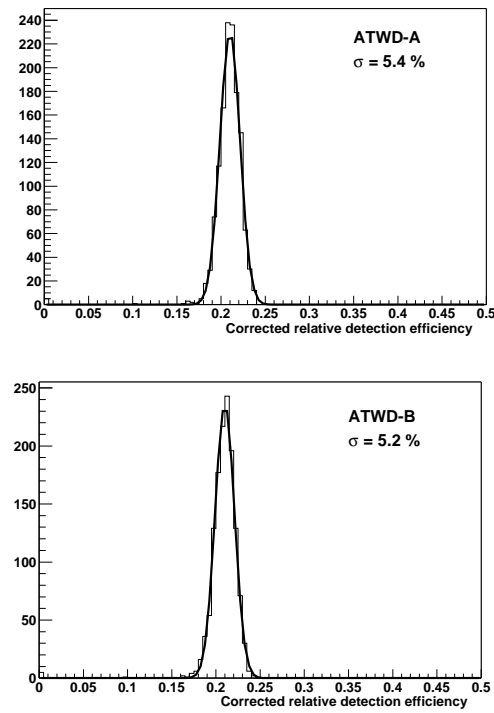
Figure A.4. The relative detection efficiency distribution per PMT per channel. The upper plot shows the relative detection efficiency distribution from the ATWD-A and the lower plot shows the same from the ATWD-B.
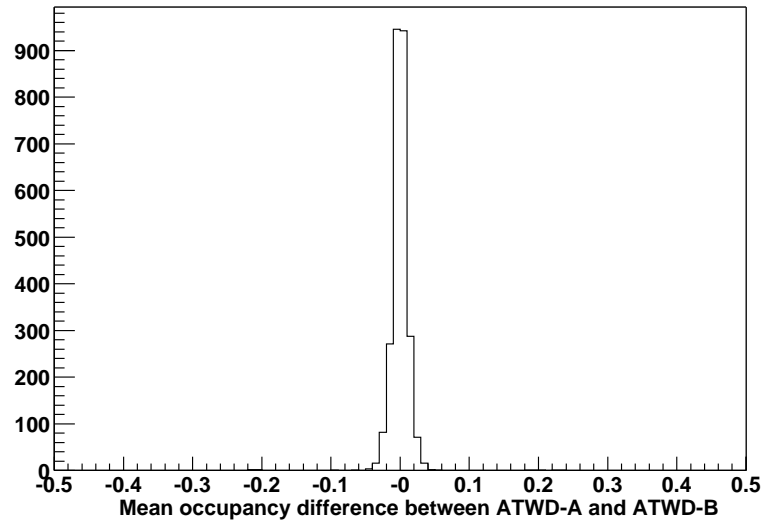
Figure A.5. The mean relative detection efficiency difference between the two channels.

The uniformity of PMT is shown in Fig. A.6. Both the gain uniformity and the relative detection efficiency uniformity are checked and are in a good status. By doing such an analysis, we know that there are about 6 bad PMTs. Five of them are completely dead PMTs and one has a lower detection efficiency. These bad PMTs or bad channels have to be taken into account for the normal data analysis.
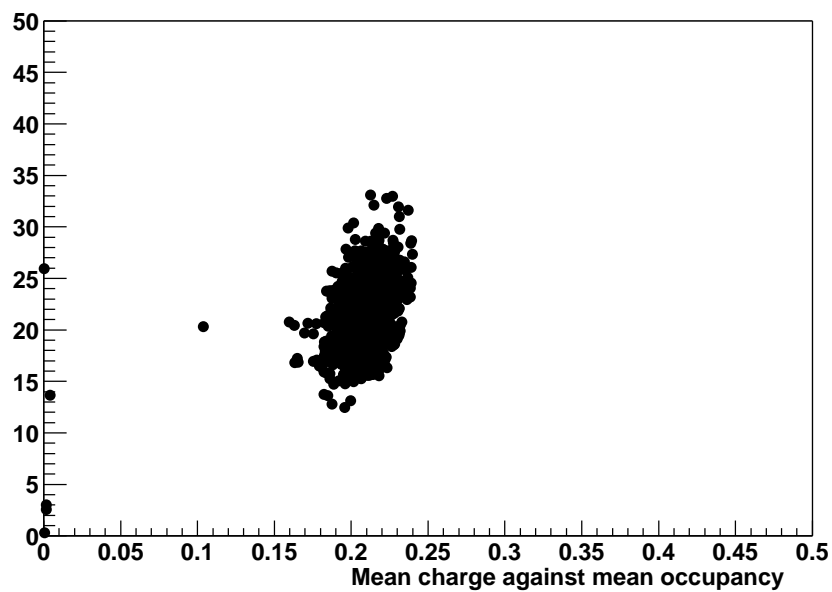
Figure A.6. The mean charge per PMT per channel against the relative detection efficiency per PMT per channel. The horizontal axis represents the relative detection efficiency. The vertical axis represents the mean charge.

A.1.3   Single photoelectron charge

The single photoelectron (SPE) charge is extracted from the mean charge and the relative detection efficiency. Assuming that the number of photoelectrons distribution per PMT per channel is a Poisson distribution, then

$$P_0 = e^{\mu}, \qquad (\text{A.4})$$

where P_0 is the probability of zero photoelectrons (PE) detected, and μ is the mean of Poisson distribution. On the other hand,

$$P_0 = 1 - \epsilon, \qquad (\text{A.5})$$

where ϵ is the relative detection efficiency (occupancy). Thus, the mean value μ = - log(P_0). Furthermore, we assume that P_1, P_2, P_3 and P_4 are the probabilities of one PE, two PEs, three PEs and four PEs registered, respectively. These probabilities can be calculated using a Poisson probability function,

$$P_N = \frac{\mu^N e^{-\mu}}{N!} \qquad (\text{A.6})$$

where N represents the number of photoelectrons. For the ^{60}Co calibration source at the center of the detector, the probability of more than four PEs registered is negligible. Once we calibrate the detector, ϵ and the mean charge ($\bar{q}$ does not include q = 0) will be known. Then we can calculate the SPE gain (q_{spe}) using the equation:

$$q_{spe} = \frac{\bar{q}}{r_1 + 2 \cdot r_2 + 3 \cdot r_4 + 4 \cdot r_4 + \cdots} \qquad (\text{A.7})$$

where $r_1 = \frac{P_1}{\epsilon}$, $r_2 = \frac{P_2}{\epsilon}$, $r_3 = \frac{P_3}{\epsilon}$, and $r_4 = \frac{P_4}{\epsilon}$ are normalization factors. Fig. A.7 shows the SPE charge distribution extracted from the mean charge displayed in Fig. A.2. Note that the above equations assume that the PMT is linear and neglect the threshold effect. The SPE is useful to the vertex and energy reconstruction.
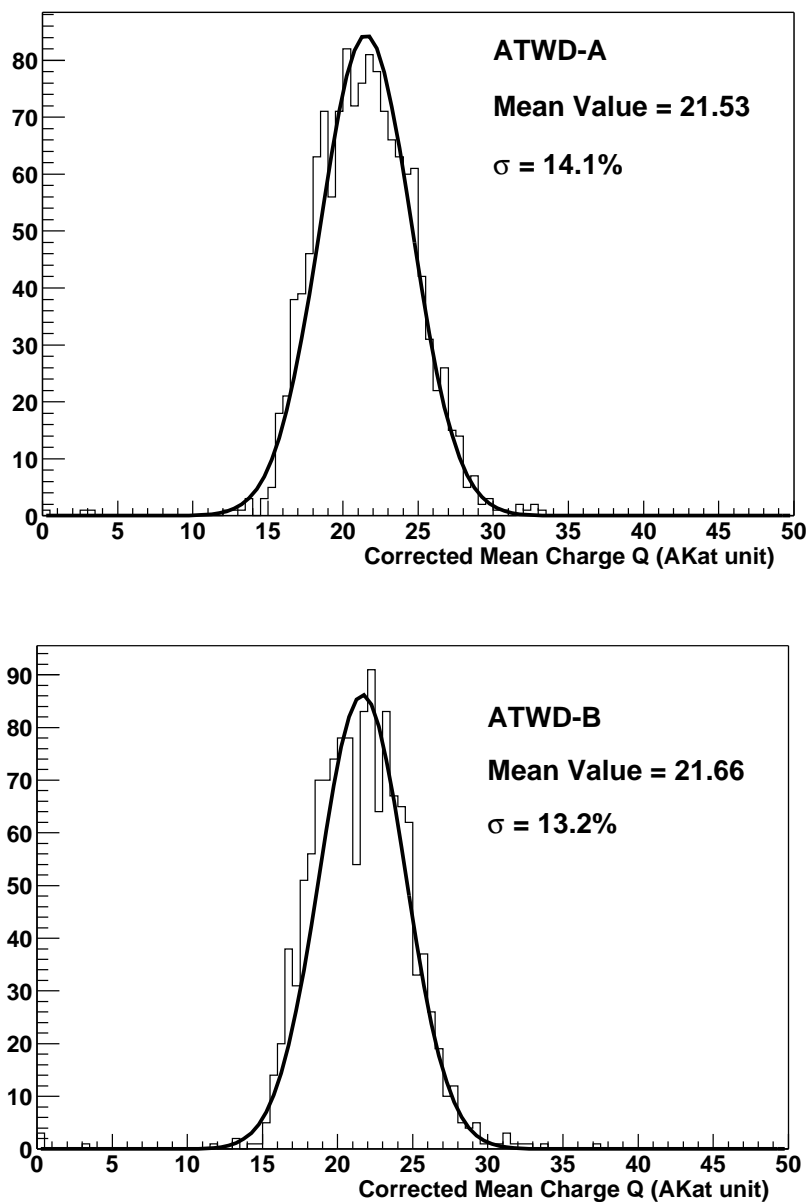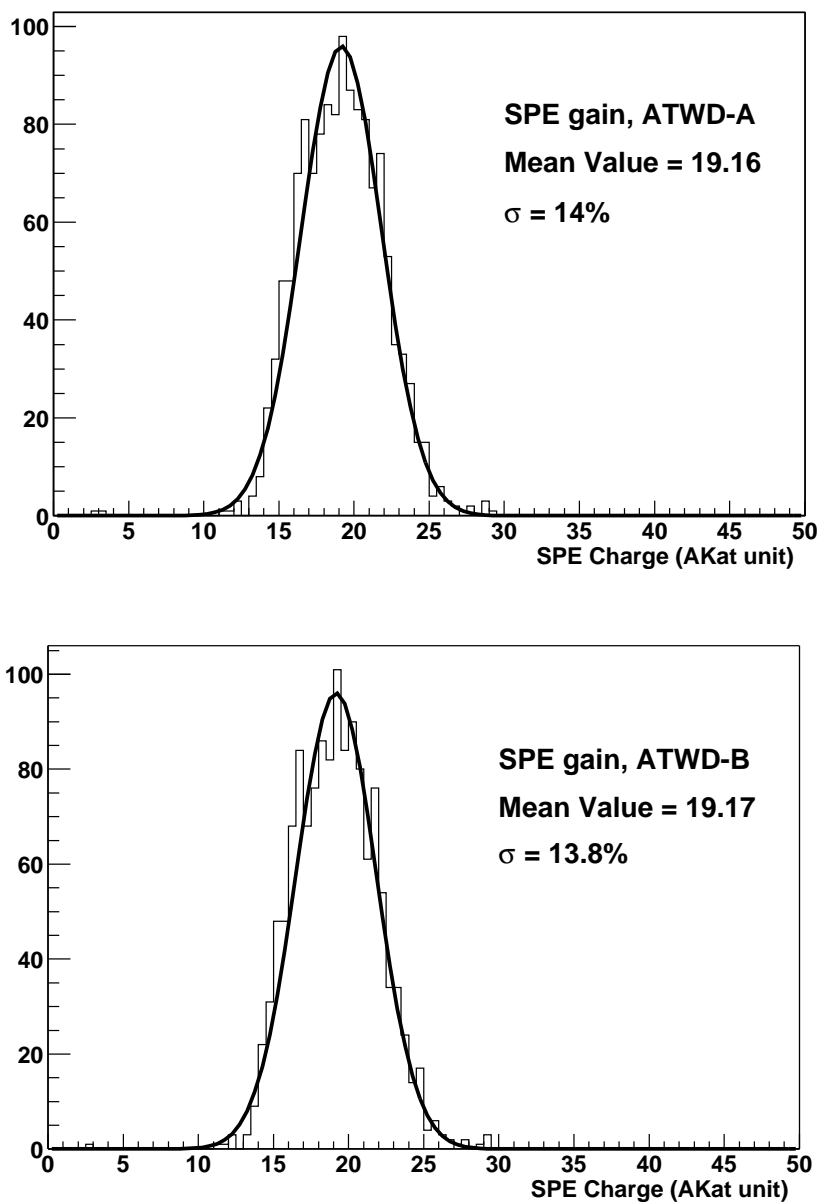
Figure A.7. The SPE charge distribution per PMT per channel. The upper plot shows the SPE charge distribution from the ATWD-A and the lower plot shows the same from the ATWD-B.

## A.1.4 Time variation of the mean charge

Using the calibrations that were performed from March to November of 2002, we have found that there is a time variation in the mean charge. The magnitude of variation is about 2.5% between March and April, and about 0.5% between April and July. After July, we began weekly calibrations to closely monitor the detector. Fig. A.8 shows the mean charge versus the run number. The time period covered in this plot is from March to November. The causes of the time variation were
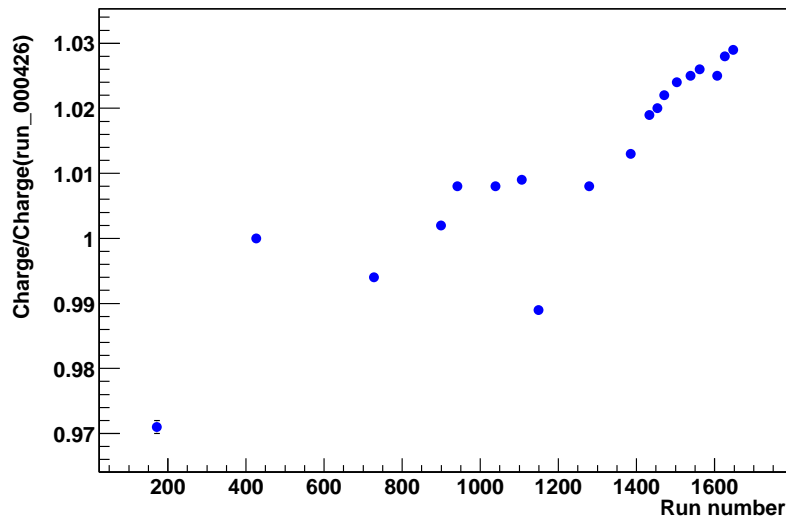
Figure A.8. The time variation of the mean charge from March to November. The ^{60}Co calibration runs at the center of the detector are used for this plot.

investigated based on the following reasons: (1) Some of the PMT's gain vary from time to time due to the high voltage varying because of the board work and the board swap. If this is the reason, then using the mean charge obtained in April minus the mean charge obtained in March, the difference between the PMTs would have some positive values and negative values. The average difference should be positive to explain the shift up during this period of time. (2) The transparency

of the scintillator and the buffer oil has become better during this period of time. If this is the case, then the mean charge difference between the PMTs would show a positive value for almost all of the PMTs. The investigation results are shown
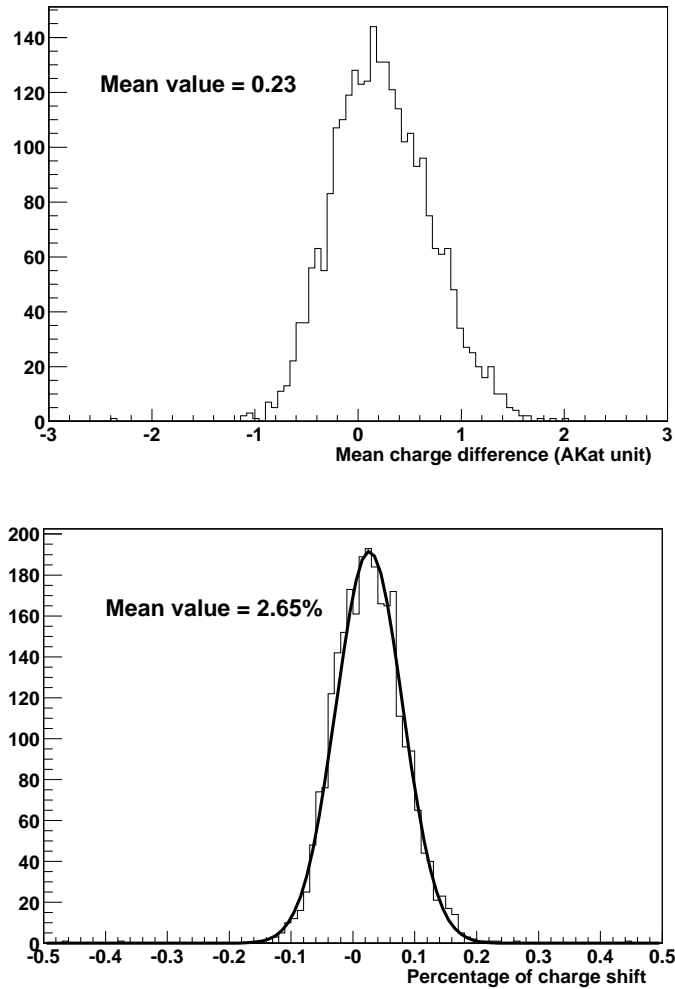
Figure A.9. The investigation of the time variation of the mean charge from March to April. The upper plot shows the mean charge difference for the same channel between March 5 and April 6. The lower plot shows the ratio of the mean charge difference to the mean charge of March 5 for the same channel.

in Fig. A.9. The upper plot in Fig. A.9 shows the mean charge difference for the

same channel between March 5 to April 6 and the lower plot shows the ratio of the mean charge difference to the mean charge of March 5 for the same channel. As we expected, the shift up of the mean charge was due to some of the PMT's behavior because the overall mean value in both plots is a positive value, but some negative values for the part of the PMTs are also observed.

The time variation of mean charge is weekly monitored. The calibration tables which contain the mean charge and the relative detection efficiency per ATWD per PMT are stored in the database for the energy reconstruction.

## A.2 Energy calibration

The energy calibration is essential to the experiment. It is also the most difficult task for the calibration. The energy response of the KamLAND detector and the light transport in such a large detector can be very complicated and involve many aspects. Therefore, doing a good energy calibration requires a good understanding of the results obtained from the data using the Monte Carlo simulation. In this section, the light transport model and the energy estimator are discussed. Some of the energy calibration results are compared with the Monte Carlo simulation.

A.2.1 Scintillation mechanism

The liquid scintillator utilizes the ionization produced by charged particles to generate optical photons, usually in the blue to green wavelength regions. A charged particle traversing the liquid scintillator leaves behind it a wake of excited molecules. Certain types of molucules release a small fraction ($\approx 3\%$) of this energy as optical photons. This process is the so-called scintillation. The optical photons emitted this way is isotropically distributed.

A.2.2 Light transport model

The light transport in the scintillator and the paraffin oil is important to the interpretation of the data obtained with the KamLAND detector. It reflects the optical properties of the scintillator. It also tests the models of the light emission process and the models of the light interaction inside the scintillator volume. Because the correct interpretation of the data requires a detailed understanding of the optical properties of the scintillator (data analysis), the detailed models of the light emission process and the detailed models of the light interaction inside the scintillator volume (MC), it is very important to study the light transport mode with a source of known energy and position.

It is well known that the energy deposition from the gamma source in the PC+PPO medium leads to the ionization and excitation mostly of the PC molecules. The PC excited molecules transfer their energy to the PPO ones and the radiative decay of the PPO excited molecules from the first excited state to the ground state is responsible for the observed fluorescence. According to the Borexino CTF study[71], the wavelengths less than 350 nm will be strongly absorbed by the fluor (PPO) and re-emitted with a longer wavelength. The reemission probability is equal to the quantum efficiency of the absorbing molecular which is around 0.8 for the PPO. This absorption-reemission process could occur several times until either the photon escapes the scintillator volume or its wavelength falls in the region where the PPO absorption probability is negligible. This fact indicates that most of the absorption and the reemission process is close to the primary scintillation position. However, the photon's interaction with the PC is mostly via Rayleigh scattering. If the photons are absorbed by the PC, then the reemission probability would be 0.34. Based on these facts, the attenuation length in the PC+PPO medium must be longer than in the PC medium because of the reemission of the PPO (the light almost doesn't escape since the KamLAND is a 4π detector). We

have built a light transport model to obtain the attenuation functions of the light in the scintillator and the paraffin oil, separately. This model is called the two functions approach.

We know that the number of photoelectrons measured per PMT per event $(\bar{n}_i)$ or charge measured per PMT per event $(\bar{\mu}_i)$ is proportional to the light transport. The equation for the point-like source at a given vertex can be expressed as

$$q_{i1} = G_i \cdot qe_i \cdot th_i \cdot \phi \cdot \chi \cdot E \cdot \Omega_{i1} \cdot T_{i1} \qquad (\text{A.8})$$

where

- G_i is the gain factor of the i-th PMT.

- q_{i1} is the observed charge for the PMT given an event vertex.

- qe_i is the quantum efficiency of the i-th PMT.

- th_i is the effect of the discriminator threshold for the i-th PMT.

- ϕ is the light yield of the scintillator per unit of energy.

- χ is the quenching factor of the light of the scintillator per unit of energy deposit.

- E is the energy deposit per event in the scintillator per event.

- Ω_{i1} is the solid angle for the i-th PMT subtend to the vertex.

- T_{i1} is the attenuation function for the light transport from the vertex to the i-th PMT which includes the combination effect of the transparency of the i-th PMT window and the transparency of the balloon.

If the point-like source is at the center, then the equation will have the same form with a different light path and a solid angle. It can be expressed as

$$q_{i0} = G_i \cdot qe_i \cdot th_i \cdot \phi \cdot \chi \cdot E_0 \cdot \Omega_{i0} \cdot T_{i0} \qquad (\text{A.9})$$

A.2.3   The solid angle and the light pathlength calculation

The solid angle assumed is that of a hemispherical surface in the farfield approximation such that the explicit expression can be written as below

$$\Omega_i = \frac{A}{2}(\frac{1 - \vec{N_i} \bullet \vec{R_i}}{R_i{}^2})$$ (A.10)

where

- A is the detector area of the PMT,

- $\vec{N_i}$ is the unit normal from the i-th PMT to the origin, and

- $\vec{R_i}$ is the unit normal from the vertex to the i-th PMT.

In calculating the light path for the light transport in different regions (scintillator and paraffin oil), we assume that the balloon is a sphere so that the constrained equation would be a spherical equation. In other words, the boundary points to distinguish the scintillator from the paraffin oil are the points which satisfy a spherical equation. Using the above method, we can calculate the solid angle for each PMT for a given vertex and the light path in the scintillator and the paraffin oil, respectively. Note that the solid angle calculated this way is an approximation.

A.2.4   Light transport functions

The light transport functions in equation (A.8) and equation (A.9) can be determined using the mean charge obtained from ^{60}Co at many positions. The procedures are the following:

Position dependence due to PMT's acceptance

PMT has different acceptance for different source positions. It is a function of the distance of the PMT from the source.
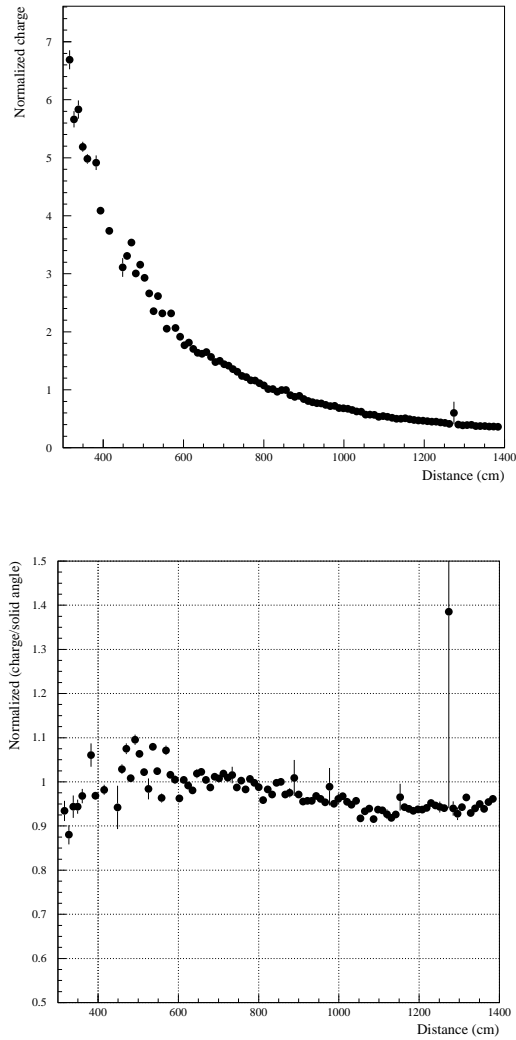
Figure A.10. The upper plot shows the position dependence plot as the PMT mean charge versus the distance of the PMT from the source. The lower plot shows the results after removing the position dependence using the solid angle of the PMTs.

- Plot the mean PMT charge (Co-60 calibration data) versus the distance of the PMT from the source (the upper plot in Fig. A.10). The mean charge for each PMT is normalized so that it is 1 for the source at z=0.

- Remove, using the far–field approximation, the position dependence due to the finite solid angle of the PMT. The lower plot in Fig. A.10 shows the result.

- The position dependence–after dividing out the solid angle dependence (to first order)–has three main features:

  1. Very weak dependence at large distances

  2. Approximately exponential dependence in the range of intermediate distances.

  3. Turns over and decreases at short distances

The shadowing of ropes and stripes on the balloon

There are some ropes and stripes to support the balloon. Although they are reflective, they are still capable of blocking some light. The shadowing due to the ropes and stripes is a function of the density of ropes (stripes) and pathlength. Fig. A.11 shows the calculation of the shadowing.

The shadowing function is given by

$$f_{i1} = p_0 \cdot tanh(p_1 \cdot (p_2 - x_{path}));$$ (A.11)

where p_0 = 0.99302, p_1 = -0.0021077 and p_2 = -616.56 are the constants, and x_{path} is the pathlength in the scintillator for the position off-center.
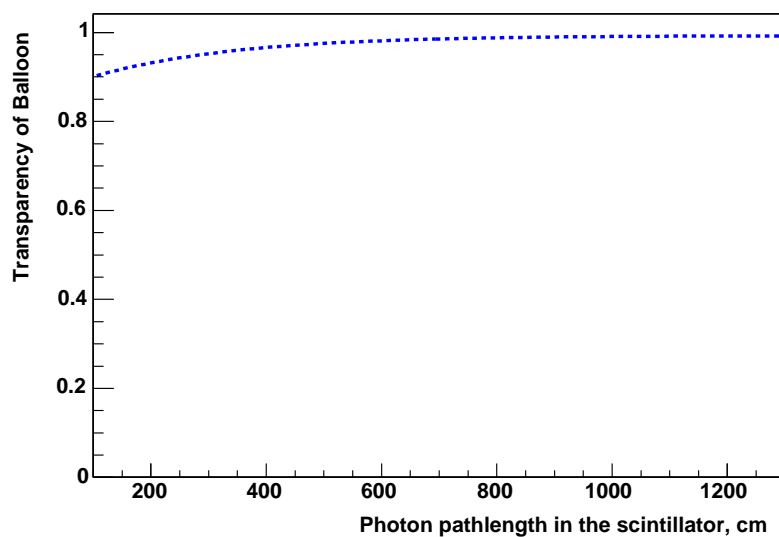
Figure A.11. The transparency of the balloon calculated based on the density of ropes (stripes).

Position dependence due to light transport

- Adopt the parametric approach to describe the remaining position dependence. Assume a product of two functions, one of which depends only on the direct optical pathlength in the paraffin oil and the other depends only on the direct optical pathlength in the scintillator. Assume further that the balloon is spherical.

- Look at the mean PMT charge as a function of the direct optical pathlength in the paraffin oil for source positions and PMT positions such that there is a relatively large variation in the paraffin oil pathlength for a narrow range of pathlengths in the scintillator. The line is a simple exponential fit. The exponential constant is $0.0013437 \ cm^{-1}$. The fitted function is

$$f_{i2} = e^{p_3 - p_4 \cdot x_{path}} \qquad (\text{A.12})$$

where $p_3 = 0.25459$ and $p_4 = 0.0013437$ are constants, and x_{path} is the pathlength in the buffer oil for the positions off-center.

- To remove the dependence of the mean charge on the direct pathlength in the paraffin oil, divide out by the fitted function described in the previous point. The plot of the result against the direct optical path length in the scintillator is shown by the points in the lower plot in Fig. A.12. Fit these points to a constant plus the product of a polynomial and an exponential. The result is indicated by the line. The fit describes the trend of the data well, but a better functional form is needed to describe the behavior at a short distance. The fitted function can be expressed as

$$f_i 3 = p_5 + p_6 \cdot x_{path}^{p_7} \cdot e^{\frac{-(x_{path} - p_8)}{p_9}} \qquad (\text{A.13})$$

where $p_5 = 0.89098$, $p_6 = 0.0001181$, $p_7 = 0.75$, $p_8 = 941.95$ and $p_9 = 220.92$ are constants, and x_{path} is the pathlength in the scintillator for the positions off-center.
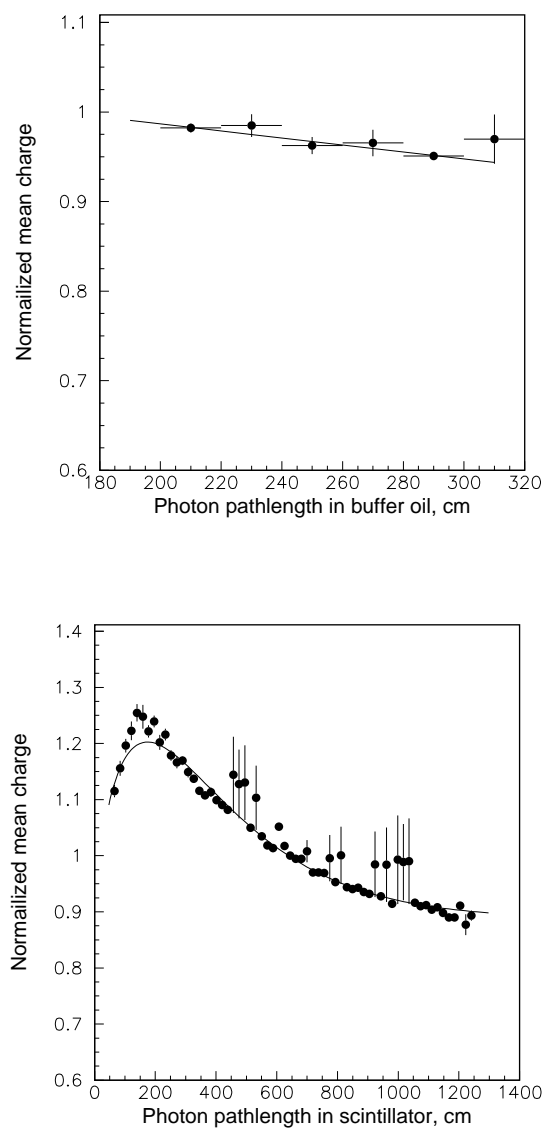
Figure A.12. The upper plot shows the position dependence. It is plotted as the PMT mean charge versus the pathlength in the buffer oil. The lower plot shows the same. It is plotted as the PMT mean charge versus the pathlength in the scintillator.

Removal of position dependence

- Finally, the last plot shows the mean charge after dividing out the solid angle dependence and the remaining dependence on direct pathlengths in the paraffin oil and the scintillator as parameterized by the product of the two fitted functions. The result is independent of distance except at short distances where our functional fit is a little poor.
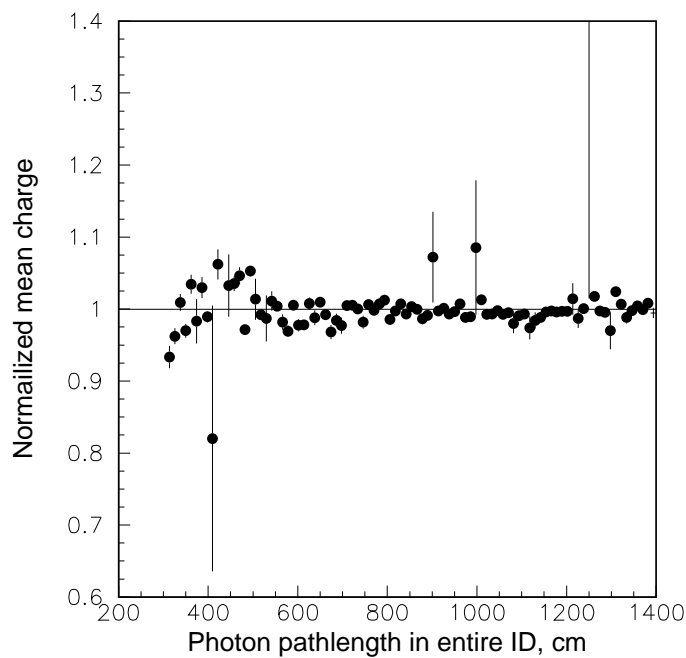

Figure A.13. The position dependence plot as the PMT mean charge versus the distance of the PMT from the source.

A.2.5 Estimation of the energy

Based on the above discussion, the formula of the energy estimation can be obtained as

$$E = \frac{E_0 \cdot \sum_i q_{i1}}{\sum_i q_{i0} \cdot \frac{\Omega_{i1} T_{i1}}{\Omega_{i0} T_{i0}}} \qquad (A.14)$$

where E_0 is the energy of the calibration source,

$$T_{i1} = f_{i1} \cdot f_{i2} \cdot f_{i3} \qquad (A.15)$$

for the positions off-center, and

$$T_{i0} = f_{01} \cdot f_{02} \cdot f_{03} \qquad (A.16)$$

for the positions at the center. T_{i1} and T_{i0} are in the same form but have different pathlengths. Equation (A.14) is the so-called energy estimator. As can be seen in this equation, the energy is reconstructed based on the light transport model and the calibration charge for the ^{60}Co source at the center of the detector. The critical conditions for using this energy estimator to reconstruct the event energy are the following:

- The calibration charge per ATWD channel per PMT must be obtained from the ^{60}C0 source at the center of the detector. This calibration should be done weekly to account for the time variations of the PMT gain and the transparency of the detector.

- The parameters of the light transport model should be obtained utilizing the ^{60}Co calibration source along the z-axis.

- In this energy estimator, we use the expected 2.506 MeV from ^{60}Co to reconstruct the event energy. The quenching effect and the $\check{C}$erenkov light yield are not included. Therefore, the visible energy of ^{60}Co needs to be understood using the MC constrained by several different gamma sources.

- A post correction of the event energy is required based on the understanding of the quenching effect and the $\check{C}$erenkov light yield by the MC.

A.2.6 ^{65}Zn and ^{60}Co source calibration

^{65}Zn and ^{60}Co are regular gamma sources to monitor the detector response. From different positions of the deployment, we can see the position dependence of the event charge and the asymmetry of the z-axis. Fig. A.14 shows the event charge position dependence along the z-axis.

After applying the light transport model, the position dependence is removed. As can be seen in Fig. A.15, the position dependence is removed effectively. The remaining z-axis position dependence is 1.4% maximum as is shown in Fig. A.15. We have also checked the run time dependence utilizing the γ source's calibration. Fig. A.15 shows the run time dependence for the sources at the center. A about 2.5% of the shift up of the total has been reported for the period of early March to early April. From April to July, the detector was relatively stable. After June, we have weekly calibration data, and the variation from week to week is normally less than 0.3%. The time variation on the long time scale is about 0.5%.

A.2.7 Energy reconstruction using ^{65}Zn ans ^{60}Co

The energy estimator is applied to reconstruct energy based on the exact source position to test the light transport model and the energy estimator. Fig. A.16 shows the percentage of difference between the reconstructed energy and the exact energy for ^{60}Co and ^{65}Zn at different positions along the z-axis. The largest deviation is about 0.7%.
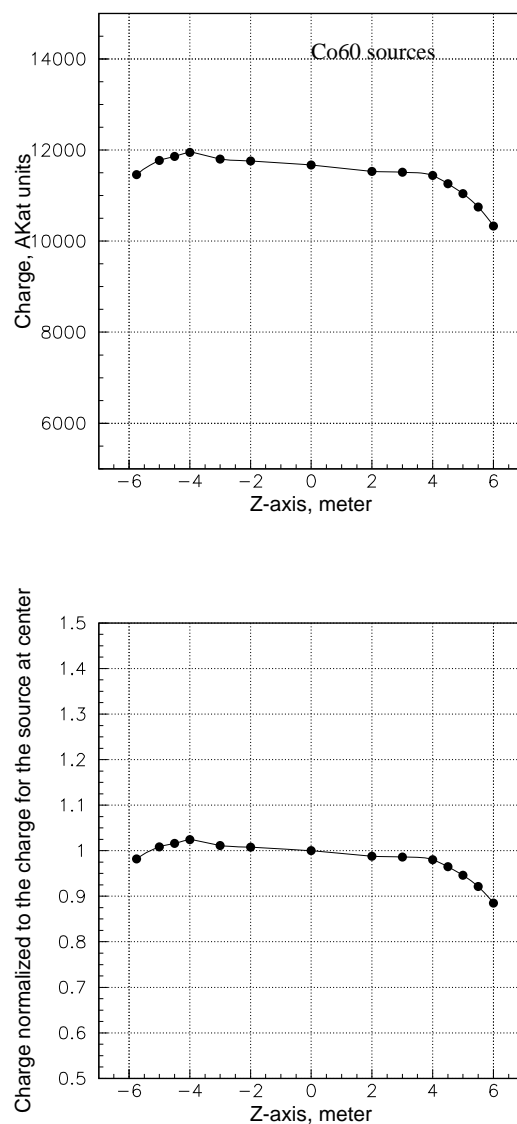
Figure A.14. The upper plot shows the centroid of the event charge distribution along the z-axis. The charge unit is in AKat unit. The lower plot shows the event charge at various positions, in which the charge is normalized to the event charge at the center for the same source.
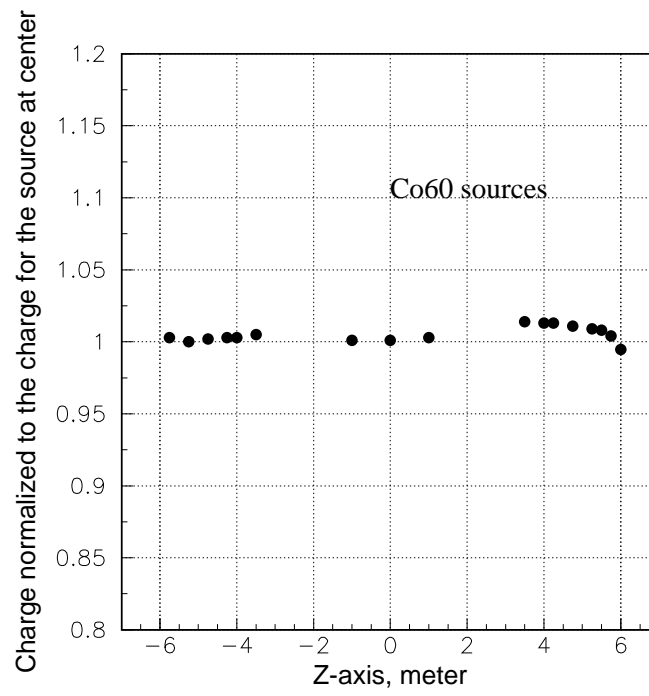
Figure A.15. The plot shows the position dependence which has been effectively removed by applying the light transport model.

Figure A.16. Energy reconstruction accuracy plot for the exact source positions.

As an example, Table A.2 shows the results of the energy estimation using the energy estimator. The fitted plot can be seen in Chapter 4.

Table A.2. Summary of the energy estimation using the energy estimator for the sources at different positions along the z-axis. The calibration runs shown in this table are the data between April and May, 2002.

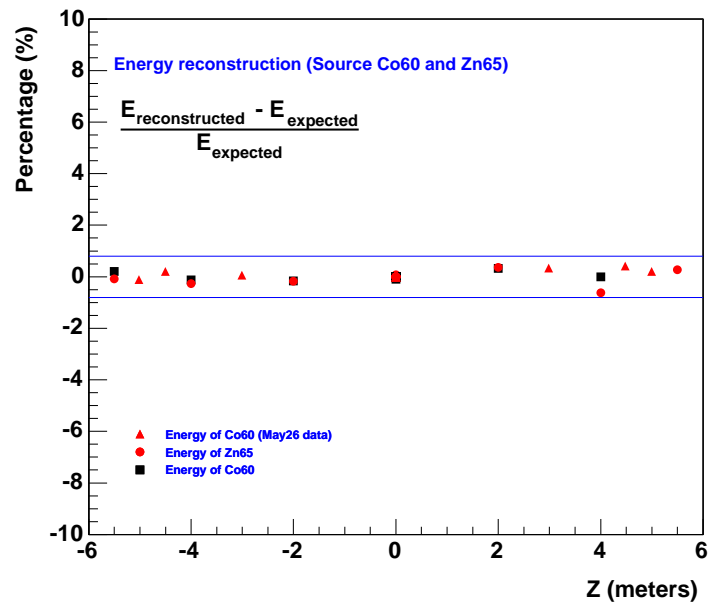| run	Z (m)	E (MeV)	Resolution (%)	Percentage Difference (%)
426	0	2.503±0.002	5.1	-0.119
557	0	1.116±0.002	7.7	0
430	2	2.514±0.002	5.1	0.319
559	2	1.12±0.002	7.7	0.358
429	-2	2.502±0.002	5.0	-0.159
566	-2	1.114±0.002	6.9	-0.179
731	3	2.514±0.004	5.0	0.319
733	-3	2.507±0.004	4.8	0.040
431	4	2.506±0.002	5.2	0
562	4	1.109±0.002	7.7	-0.627
428	-4	2.503±0.002	5.0	-0.119
565	-4	1.113±0.002	7.6	-0.269
730	4.5	2.516±0.004	5.0	0.399
734	-4.5	2.511±0.004	4.8	0.199
729	5	2.511±0.005	5.2	0.199
735	-5	2.503±0.004	4.9	-0.119
563	5.5	1.119±0.003	8.7	0.269
432	-5.5	2.511±0.002	5.2	0.199
564	-5.5	1.115±0.002	8.1	-0.089

A.2.8 Moderated ^{241}Am/Be source calibration

To understand the detector energy response, we need to have at least three different gamma energies with the energy range up to a few MeV. ^{65}Zn and ^{60}Co provide 1.116 MeV and 2.506 MeV, respectively. ^{241}Am/Be provides a higher energy, 4.4 MeV, which is desirable for the energy scale calibration. Since every 4.4

MeV gamma comes with a fast neutron with kinetic energy of a few MeV[47], it is necessary to moderate fast neutrons so that the 4.4 MeV gamma can be seen clearly. Therefore, the ^{241}Am/Be source is designed with a polyethylene moderator to slow down the fast neutrons from the source. Fig. A.17 shows the design of the moderator. Since this is a mildly complicated source with a relatively large
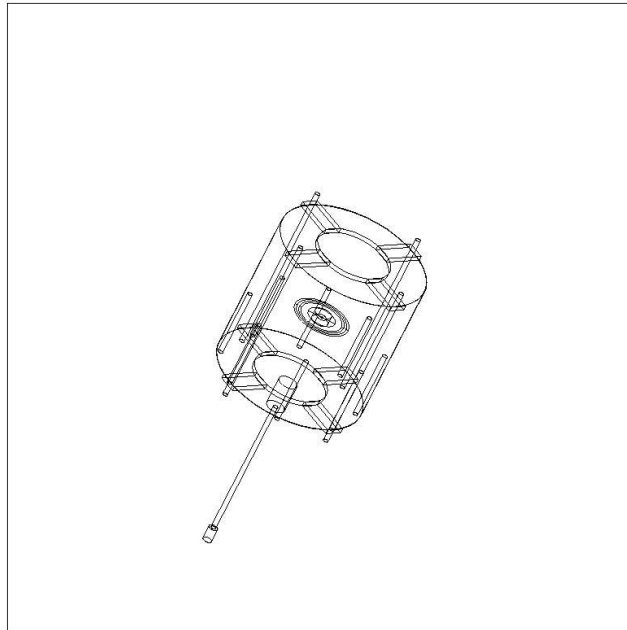
Figure A.17. The plot shows the geometrical design of the moderator.

size, the shadowing due to the moderator is expected. To find out the shadow-

ing, a full Monte Carlo simulation is required. The neutron transport code is GCALOR[73]. Fig. A.18 shows the prompt energy distribution of the moderated ^{241}Am/Be source and the comparison between the MC and the measurement. The
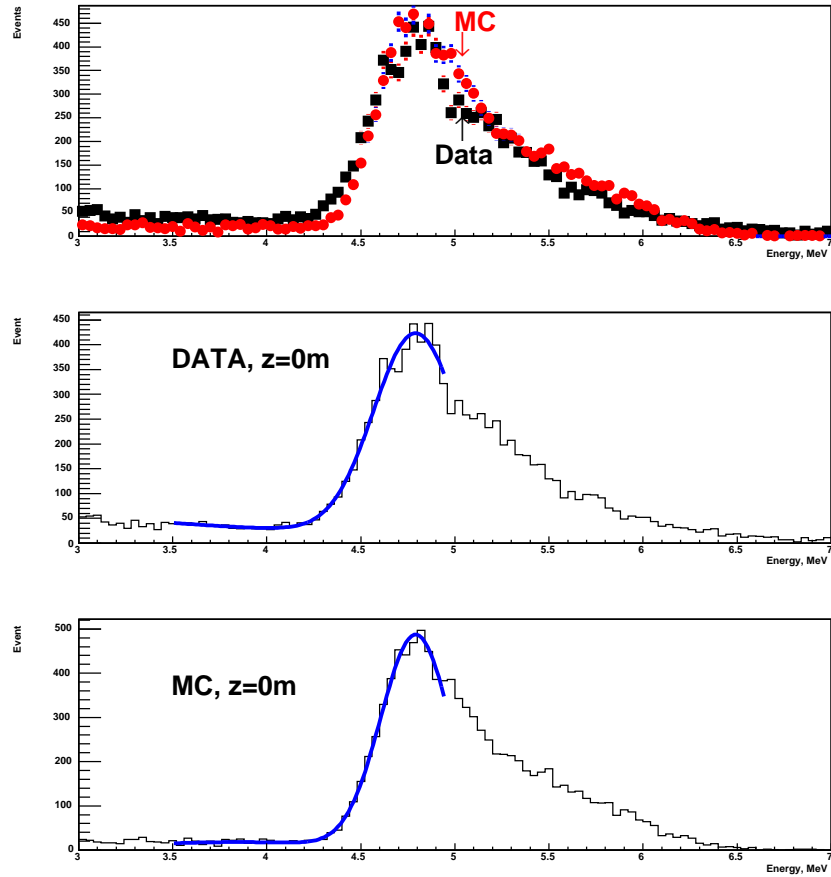
Figure A.18. The prompt energy distribution of the moderated ^{241}Am/Be source. In the upper plot, the squares represent the measurement and the circles represent the MC. The plot in the middle is the result obtained from the data. The lower plot shows the result obtained from the MC.

shadowing for the photons due to the 4.43 MeV gamma energy deposit is about

1.2%. However, the shadowing for the photons due to the 2.225 MeV capture gamma is about 2%. Fig. A.19 shows the delayed energy distribution of the moderated ^{241}Am/Be source obtained from the data and the MC. As can be seen, the measured results agree with the Monte Carlo results very well.
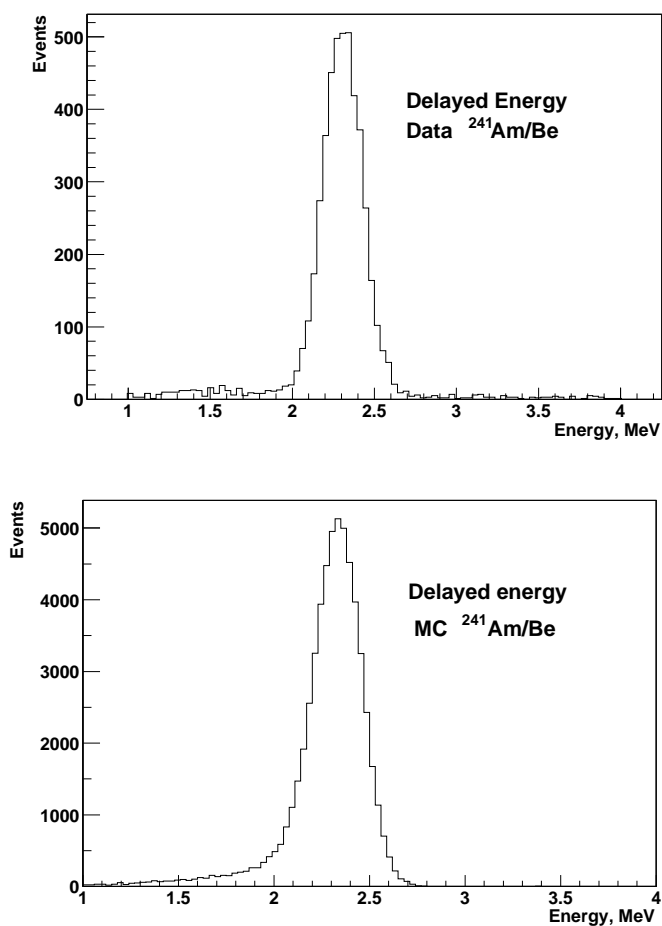
Figure A.19. The upper plot shows the delayed energy distribution of the moderated ^{241}Am/Be source from the measurement. The lower plot shows the delayed energy distribution of the moderated ^{241}Am/Be source from the MC.

A.2.9 ^{68}Ge source calibration

^{68}Ge is a positron annihilation gamma source and provides two annihilation gammas per event. Fig. A.20 shows the energy reconstruction for the annihilation gammas from the ^{68}Ge source. The upper plot shows the result from the measurement and the lower plot shows the result from the MC. As can be seen, the difference between the MC and the measurement is less than 1%.
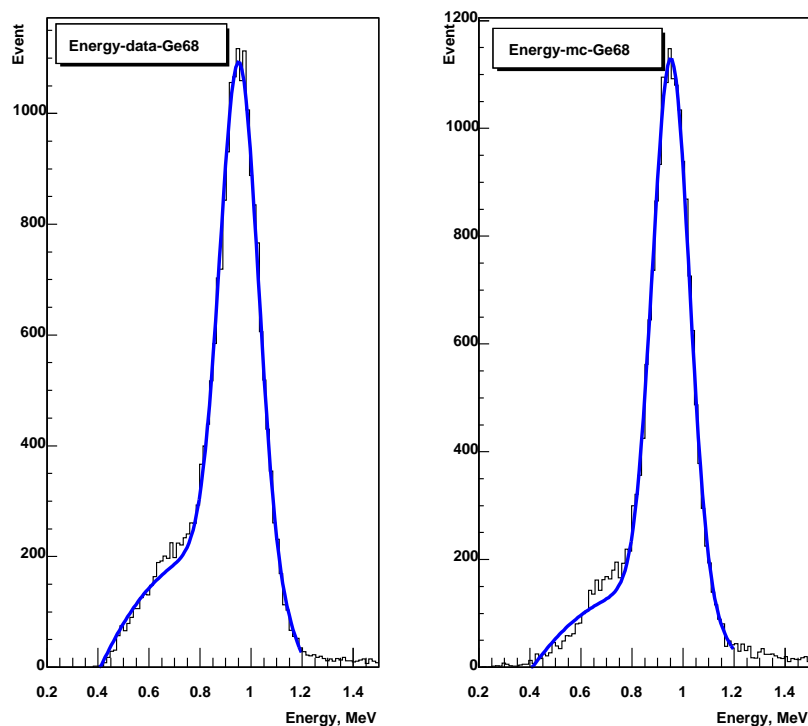

Figure A.20. The left plot shows the energy distribution of annihilation gammas from the measurement. The right plot shows the same from the MC.

A.2.10 Spallation neutron as an off-axis calibration

Spallation neutrons induced by cosmic ray muons are distributed uniformly in the entire detector. This feature allows us to study the energy position dependence off the z-axis. The signal channel is $n + p \rightarrow d + \gamma$ (2.225 MeV). The criteria for selecting events are detailed in Chapter 6. Fig. A.21 shows the reconstructed energy distribution. Table A.3 shows the energy reconstruction uniformity utilizing the capture gammas from spallation neutrons. The critical calibrations are (1) the distribution uniformity in the entire detector, (2) the width of the distribution in the entire detector, and (3) the centroid of the distribution comparing to the expected value. In order to achieve the above calibration goals, we divide the detector into some slices in terms of the radius. The conclusions that can be made from Table A.3 are: (1) the distribution uniformity in the entire detector is about 0.4% and 1% with and without weighting by the number of events, (2) the width of the distributions result the energy resolution is about 5.2%, and (3) the centroid of the distribution is about 2.38 MeV, which is about 7% higher than the expectation (2.225 MeV). The causes for this 7% energy shift up will be discussed in detail in the next section.

Table A.3. Spallation neutrons energy uniformity and the energy resolution in the entire detector.

Radius (m)	Centroid (MeV)	Width (MeV)	Resolution (%)
R< 2	2.375±0.005	0.122±0.005	5.1
$2 < R <4$	2.370±0.002	0.125±0.002	5.3
$4 < R <5.5$	2.385±0.002	0.124±0.001	5.2
R<5.5	2.384±0.001	0.125±0.001	5.2
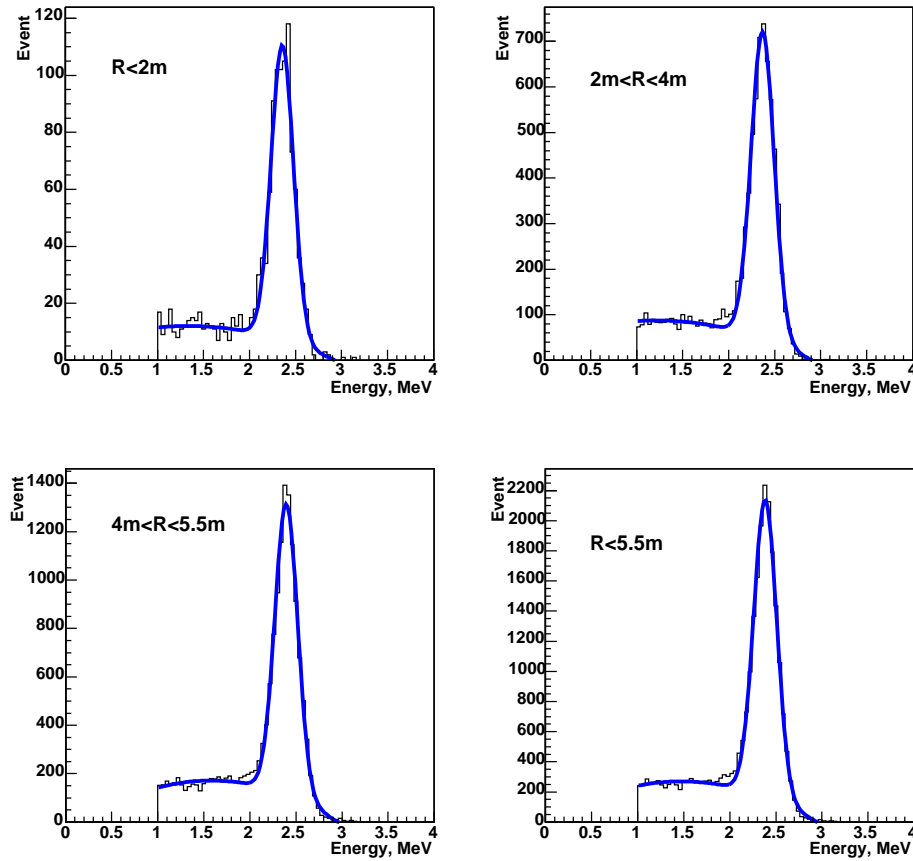
Figure A.21. Spallation neutron induced 2.225 MeV gamma energy distribution with different radius cuts.

A.2.11   Summary of the energy calibration

As can be seen from the above discussion, the energy response of the detector is not in a linear relationship between various energies. In other words, the visible energies from different gamma sources show a non-linear energy scale which has to be understood. Table A.4 shows a summary of the energy calculation.   If one

Table A.4. Summary of the energy reconstruction with various energy sources.

Energy sources	Kinetic energy	reconstructed energy
^{68}Ge	0.511 MeV	0.474 MeV
^{65}Zn	1.116 MeV	1.12 MeV
^{60}Co	1.173 MeV	1.173 MeV
	1.333 MeV	1.333 MeV
n(p,d)γ	2.225 MeV	2.38 MeV
^{241}Am/Be	4.43 MeV	4.87 MeV
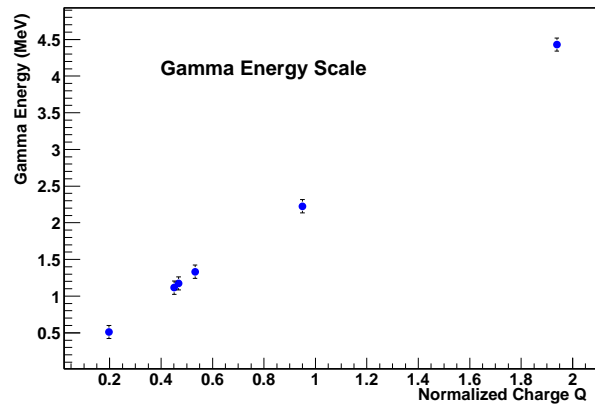
Figure A.22. The non-linearity of the energy response obtained from various energy sources.

normalizes all of the reconstructed energies to ^{60}Co with an expected kinetic energy of 2.506 MeV, a linear function of energy will not explain all of the reconstructed energies within a 2% accuracy. Instead, a maximum deviation of 7% error will be found. This can be seen in Fig. A.22. The cause of this non-linearity will be discussed in detail in the next section.

A.3   Energy scale

It is well known that the scintillator does not respond linearly to the ionization density. Very dense ionization columns emit less light than expected on the basis of dE/dX for a minimum-ionizing particle. Birk's law is widely used to describe the quenching effects between the excited molecules that reduce the light yield[74]. A charged particle radiates Čerenkov light if its velocity is greater than the velocity of light[75] in the medium; the light yield of Čerenkov radiation is energy dependent. The quenching effects and Čerenkov radiation are responsible for the non-linear energy scale of the detector. To understand the detector energy scale, several different gamma sources were deployed. The energy range covers from 1.022 MeV through 7.65 MeV. The results from the data were compared to the Monte Carlo simulation. In this section, the energy scale and the systematic errors are understood with the Monte Carlo simulation.

A.3.1   Quenching and Čerenkov effect

The overall energy response of the detector derived from the calibration data along the z-axis and spallation neutrons in the entire detector volume is a non-linear function. The non-linearity can be explained by the quenching effect and the Čerenkov effect. In this section, we use the Monte Carlo to study the non-linearity. The neutron transport code is GCALOR. The code is basically the same as the one we used for the ^{241}Am/Be source study. In studying the quenching effect, we adopt the first order of Birk's law. The constant $k_b = 0.012$ g cm^{-2} MeV^{-1} is from a KamLAND internal measurement, where k_b is determined by α quenching measurement. The Čerenkov production in the PC and PPO based scintillator has to consider the shorter wavelengthed photons (below 350 nm), which are usually cut off by the PMT cathode. In the scintillator, when photons interact with the PC and the PPO, the absorption happens strongly for the photons with

wavelengths below 350 nm. The PPO absorbs photons with wavelengths below 350 nm at about a distance of 10 cm and re-emits these photons with longer wavelengths with a probability of 80% (Borexino CTF study[71]). The PC absorbs photons with wavelengths below 350 nm at a distance of about 3 m and re-emits these photons with longer wavelengths with a probability of 34% (Borexino CTF study[71]). Therefore, in the $\check{C}$erenkov light yield model, we need to take the wavelengths below 350 nm into account to calculate the photon production. From the KamLAND PMT information, we know that the quantum efficiency of the PMT cuts off photons with wavelengths longer than 650 nm. The upper limit of the wavelength of a photon is 650 nm. The formula for calculating the $\check{C}$erenkov light production is:

$$\frac{dN^c}{dx} = 2\pi z^2 \alpha sin^2\theta_c \int_{\lambda_1}^{\lambda_2} \frac{d\lambda}{\lambda^2} \qquad (\text{ A.17})$$

We know that the photon interaction with PC and PPO can be described as

$$N(x,\lambda) = N_{0,\lambda}(a_1(\lambda)e^{\frac{-x}{l_1}} + a_2(\lambda)e^{\frac{-x}{l_2}}) \qquad (\text{ A.18})$$

where $a_1(\lambda) + a_2(\lambda) = 1$ and $N_{0,\lambda} = \int I_0 \, d\lambda$. In our conditions, $l_1 \sim 10$ cm is mostly due to the interaction with PPO and $l_2 \sim 3$ m is dominated by the effect of the interaction with PC. Taking the reemission probability of PC and PPO into account, the final $\check{C}$erenkov light yield formula in our MC is

$$N = 2\pi z^2 \alpha sin^2\theta_c(\alpha(\lambda) \int_{\lambda_1}^{\lambda_2} \frac{d\lambda}{\lambda^2} + \beta(\lambda) \int_{\lambda_3}^{\lambda_4} \frac{d\lambda}{\lambda^2}) \qquad (\text{ A.19})$$

where $\alpha(\lambda)$ is the overall surviving probability for photons with wavelengths below λ_2 interaction with PC and PPO, and $\beta(\lambda)$ is the overall surviving probability for photons with wavelengths between λ_3 and λ_4 interactions with the PC and the PPO.

A.3.2   The raw charge distribution from data and MC

Using the above $\check{C}$erenkov light yield model and the first order of Birk's law, we reproduced the gamma sources calibration data. Fig. A.23 shows the charge
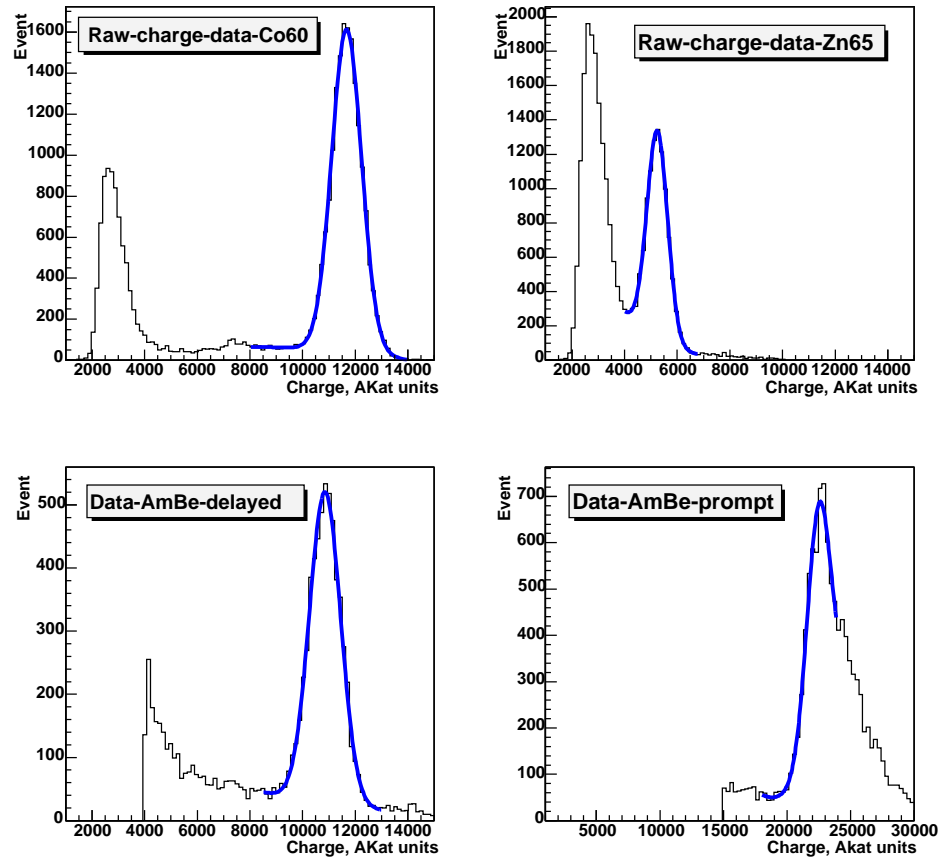
Figure   A.23.   The raw charge distribution from the measurement for gamma sources calibration.

distribution from the measurement and Fig. A.24 shows the charge distribution from the MC. Notice that for the ^{241}Am/Be source simulation, the shadowing

effects due to the moderator are corrected in the MC. The shadowing effect are ~2% for 2.225 MeV gamma and ~1.2% for 4.43 MeV gamma.
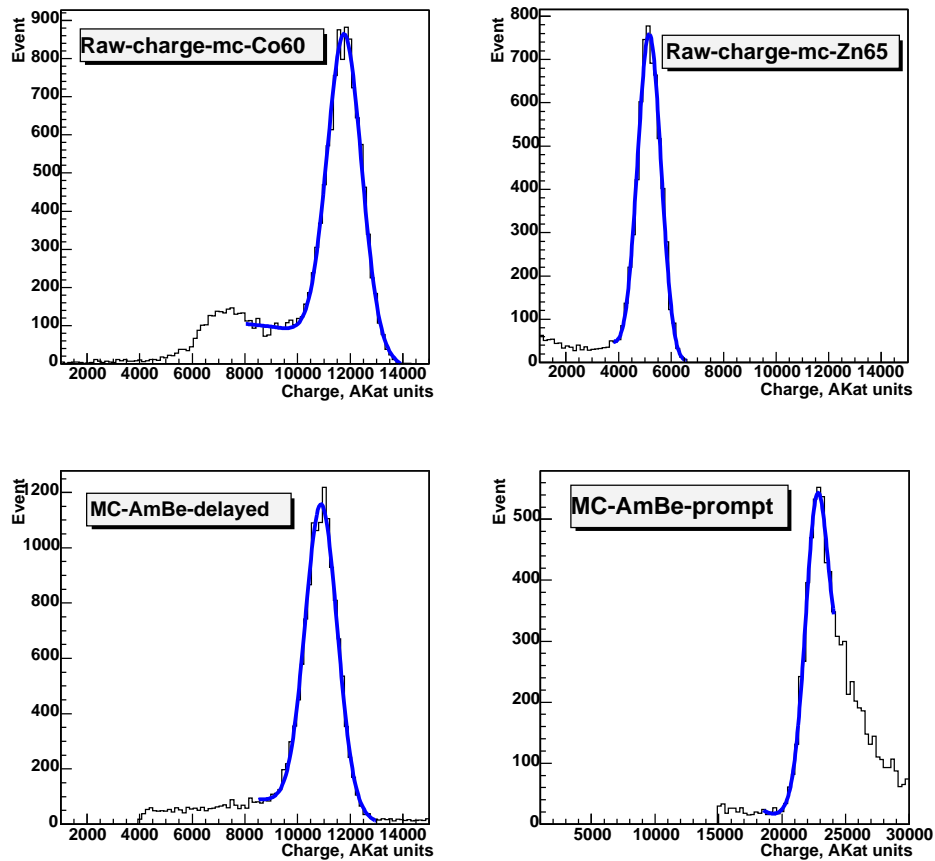
Figure A.24. The raw charge distribution from the Monte Carlo simulation for gamma sources calibration.

Fig. A.25 shows the comparison of the raw charge distribution between the MC and the measurement.
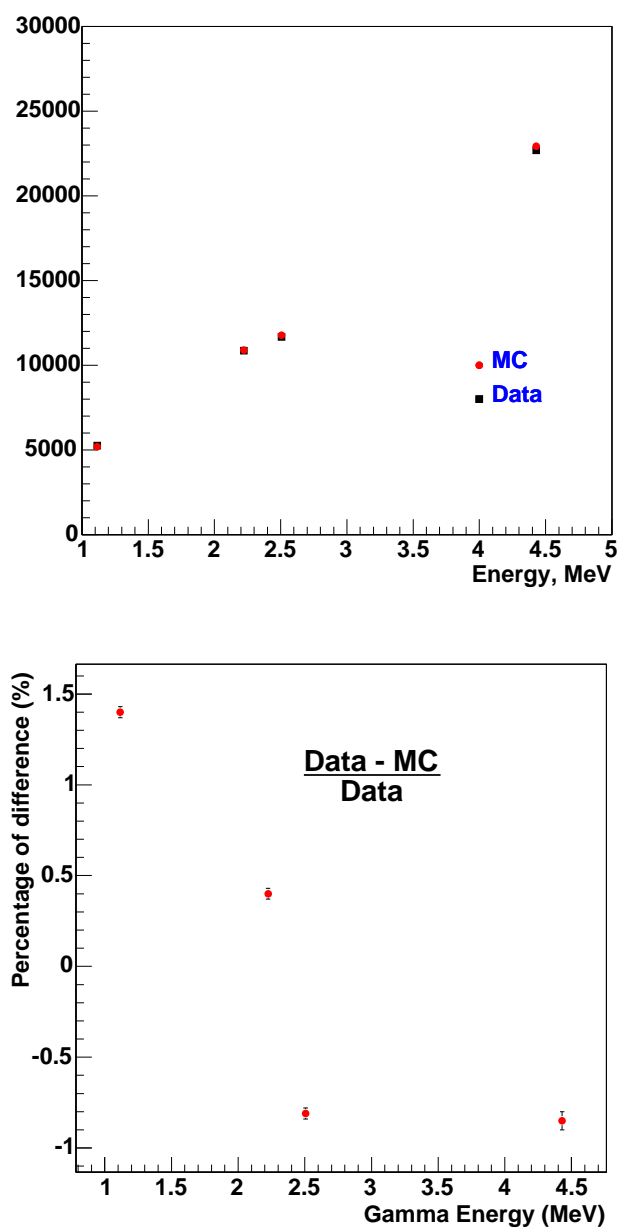
Figure A.25. The upper plot shows the agreement between the MC and the measurement. The lower plot shows the difference between the MC and the measurement.

As can be seen, the difference between the MC and the measurement is about 1.4% maximum.

We also compared the ^{68}Ge raw charge distribution between the data and the MC. Fig. A.26 shows the raw charge distribution for annihilation gammas from the ^{68}Ge source. The upper plot shows the result from the measurement and the lower plot shows the result from the MC. As can be seen, the difference between the MC and the measurement is less than 1%.

Figure A.26. The left plot shows the charge distribution of annihilation gammas from the measurement. The right plot shows the same from the MC.

A.3.3 Energy scale functions

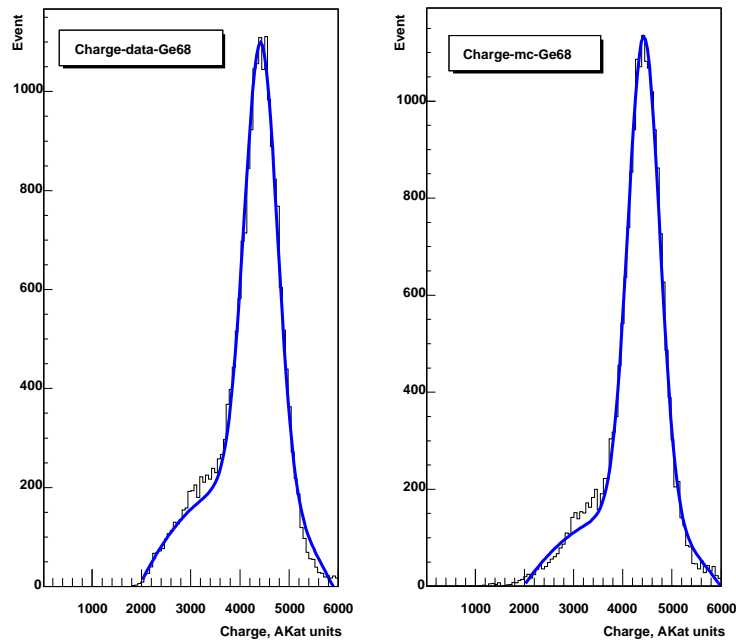Since the MC can reproduce the gamma source calibration with about 1% accuracy, it can be trusted to study the positron energy scale for inverse beta decay. Under this motivation, we have generated several mono-energetic positrons, electrons, gammas with the same energies, 1 MeV, 3 MeV, 5 MeV, 7 MeV at the center of the detector to obtain the energy scale functions for different types of particles.

- Energy scale function for gamma sources calibration

  The current energy estimator returns the energy per event without correcting the quenching effect and the $\check{C}$erenkov effect. The energy scale is not linear for the energy response of the detector. To get real energy per event, we need a scale function which determines the energy in terms of the event charge after the light transport correction. In the current energy estimator, the event charge can be returned as

$$Q_0 = \frac{E_{akat}}{2.506} \qquad (\text{ A.20})$$

  where Q_0 is the normalized event charge, in which $Q_0 = 1$ for ^{60}Co, E_{AKat} is the reconstructed energy from the American KamLAND analysis tool (AKat). Fig. A.27 shows the gamma energy scale function. The function can be expressed as

$$E_{real} = \frac{p_0 \times Q_0}{1 + \frac{p_1}{\sqrt{Q_0}} + p_2 \times Q_0} \qquad (\text{ A.21})$$

  where E_{real} is the real energy of the particle, $p_0 = 2.108$, $p_1 = -0.095769$ and $p_2 = -0.0012051$ are constants from the fitted parameters.
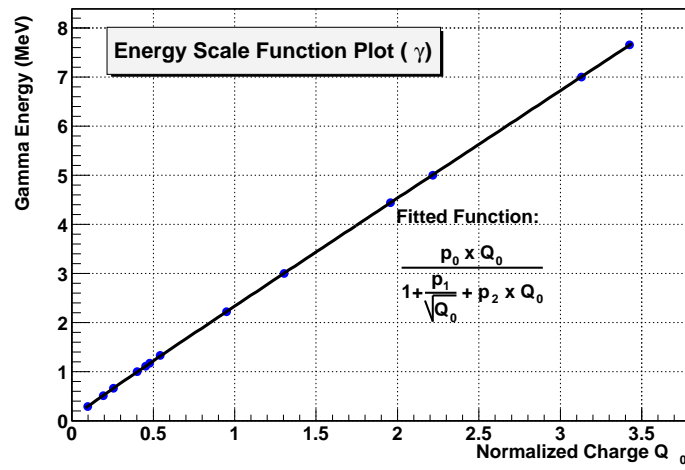
Figure A.27. The gamma energy scale function obtained from the data and the MC.

- Energy scale function for electrons

  To obtain the energy scale function for β^- particles, we have performed the Monte Carlo simulation for β^- particles at different energies. The normalized charge is from equation (A.20). Fig. A.28 shows the electron energy scale function.
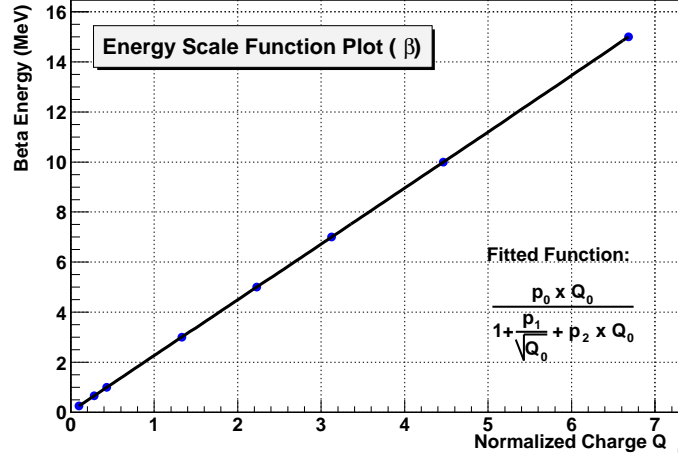
Figure A.28. The electron energy scale function obtained from the MC.

The function can be expressed as

$$E_{real} = \frac{p_0 \times Q_0}{1 + \frac{p_1}{\sqrt{Q_0}} + p_2 \times Q_0} \qquad (\text{A.22})$$

where E_{real} is the real energy of the particle, $p_0 = 2.168$, $p_1 = -0.0416945$ and $p_2 = -0.0027297$ are constants from the fitted parameters.

- Energy scale function of positron

  Using the MC, we have studied the energy scale function for positron. As

we have discussed previously, there is a significant difference between the gammas and positrons because of the quenching and the Čerenkov effect. Therefore, the energy reconstruction is, indeed, particle ID dependent. The positron energy scale function is determined based on the MC and the ^{68}Ge positron source. Fig. A.29 shows the positron energy scale function. The
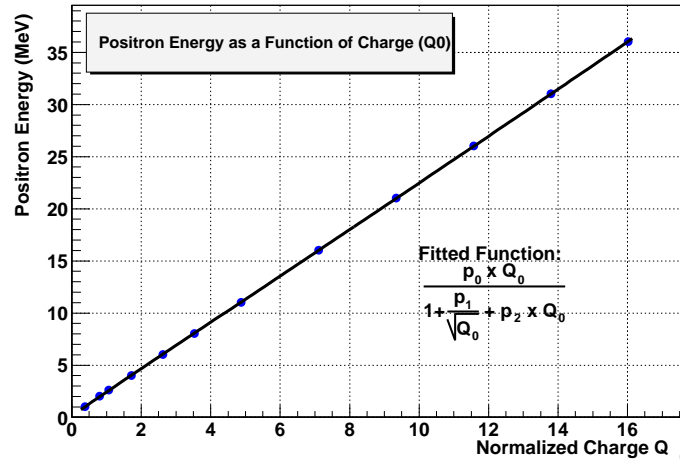
Figure A.29. The positron energy scale function obtained from the MC.

function can be expressed as

$$E_{real} = \frac{p_0 \times Q_0}{1 + \frac{p_1}{\sqrt{Q_0}} + p_2 \times Q_0} \qquad (\text{A.23})$$

where E_{real} is the real energy of the particle, $p_0 = 2.127$, $p_1 = -0.12072$ and $p_2 = -0.00153837$ are constants from the fitted parameters.

A.3.4 Energy scale systematics

- Energy scale systematic error for the γ-based energy estimator

  Using the currently available gamma sources calibration data along the z-

axis, we have checked the position dependence with the vertex reconstruction and without the vertex reconstruction (taking the calibration position as the vertex). The position dependence without the vertex reconstruction is about 0.7%. With the vertex reconstruction, the position dependence is about 1.4% maximum. With the spallation neutron signature, the radial dependence is about 1.3% on average. In addition to the spatial dependence, there is 0.5% of time variation in the long time scale. By understanding the non-linear energy response with the quenching effect and the Čerenkov effect, the energy scale function for gammas introduces about 1% error. Therefore, the energy scale systematic error for the gamma-based energy estimator can be calculated as

$$\Delta E_\gamma = \sqrt{position_{dep}^2 + time_{dep}^2 + scale_f^2} \qquad (\text{A.24})$$

where $position_{dep}$ is the z-axis dependence with vertex reconstruction from the ^{60}Co and the ^{65}Zn gamma sources combined with the radial dependence from the spallation neutron capture (the off z-axis dependence), $time_{dep}$ is the time variation of long time scale, $scale_f$ is the scale function error based on the centroid of the source. Putting the values into the above formula, $\Delta E_\gamma = 1.79$ %.

- Energy scale systematic error for e^+

  The MC for positron is based on our understanding of the gamma sources calibration data, which has 1% of energy scale error. Therefore, this error is propagated into the positron simulation. There are other uncertainties: high energies and light transport particle independence. First, above the 4.4 MeV energy, the result is only based on a simulation, it could introduce the systematic error. Second, in our MC model, we assumed that the long-distance light transport is independent of the particle ID. It may have

another small error with this in the wavelength which is not strongly absorbed and re-emitted by PPO/PC. In evaluating the systematic error for the positron energy scale, we are facing the following issues:

1. Uncertainty on Birk's constant

    We have the experimental value k_b from the measurement of α, for which we believe that there is no $\check{C}$erenkov effect. Therefore, this k_b can be used to study the quenching on γ (Compton electrons). However, α particle has 2 units of charge. According to Birk's law, k_b could be different to 1 unit of charge particle (Compton electron).

2. Uncertainty on the $\check{C}$erenkov light yield model

    Without PPO and PC in the scintillator, the $\check{C}$erenkov light yield is well understood. However, with PPO and PC, and the absorption and reemission of the photons as a major feature of the PPO and PC based scintillator, the $\check{C}$erenkov light yield could be extended down to the UV range and become an important part of the total signal. We know that the $\check{C}$erenkov light yield is a non-linear function of energy. Therefore, the non-linear energy response of the detector could be largely due to this effect. Since we don't know the exact wavelength cutoff of the $\check{C}$erenkov photons in the PPO and PC based scintillator, there is a major uncertainty about the wavelength range for the lowest wavelength cutoff in the $\check{C}$erenkov light yield model.

To minimize the uncertainty in the e^+ systematic error calculation, we varied the MC parameters in the $\check{C}$erenkov light yield model and Birk's constant to observe the variation in E_{e+} at 2.6 MeV when the variation in E_γ is less than 1%. In equation (A.19), the nominal of λ_1 is 120 nm, $\lambda_2 = \lambda_3 = 350$ nm, $\lambda_4 = 650$ nm, $\alpha(\lambda) = 0.9$, and $\beta(\lambda)$=1.0. The nominal $k_b = 0.012$ g cm^{-2} MeV^{-1}. We have varied λ_1 at 100 nm, 150 nm, 175 nm, and 200nm. We

have also varied $\alpha(\lambda)$ in equation (A.19) at 0.8 and 0.9. Except for varying the parameters in the $\check{C}$erenkov light model, we have varied k_b from 0.012 g cm^{-2} MeV^{-1} to 0.007 g cm^{-2} MeV^{-1}, 0.02 g cm^{-2} MeV^{-1} by holding λ_1 = 120 nm and $\alpha(\lambda)$ = 0.9. Table A.5 shows the variation of the charge of gamma sources due to the varied parameters in the MC model.

Table A.5. The variation of the charge by varying k_b and the $\check{C}$erenkov parameters.

Parameters	$(Q^{MC}-Q^{Data})/(Q^{Data})$				
	^{68}Ge	Zn65	^{60}Co	2.2MeV	4.43MeV
Nominal	0.3%	-0.6%	0.3%	-0.1%	-0.5%
λ_1=100	0.3%	-0.4%	1.7%	1.9%	2.0%
λ_1=150	0.1%	-1.7%	-0.9%	-1.9%	-3.0%
λ_1=175	0.1%	-1.8%	-0.9%	-2.2%	-3.5%
λ_1=200	-0.1%	-2.8%	-2.0%	-3.86%	-5.5%
$\alpha(\lambda)$=0.8	0.2%	-1.2%	-0.4%	-0.8%	-1.5%
$\alpha(\lambda)$=1.0	0.4%	-0.5%	0.5%	0.6%	0.8%
k_b=0.007	3.9%	1.6%	2.4%	1.7%	0.8%
k_b=0.02	-4.7%	-4.4%	-3.3%	-2.6%	-2.5%

As can be seen in Table A.5, the variation of the charge of gammas within 1% for all sources is nominal values and $\alpha(\lambda)$=1.0 with other nominal values. Corresponding to this valid variation of $\alpha(\lambda)$, the maximum variation at 2.6 MeV positron energy is about $\delta E_{2.6MeV}$= 0.8% due to the above variation of parameters. Therefore, the systematic error at the 2.6 MeV positron energy threshold is

$$\Delta E_{2.6MeV} = \sqrt{\Delta E_\gamma^2 + \delta E_{2.6MeV}^2} = \sqrt{1.79^2 + 0.8^2}\% = 1.97\%. \qquad (A.25)$$

The maximum variation for the positron energy scale that we have seen is 1% at 7 MeV kinetic energy. Therefore, the overall systematic error of

positron energy scale is 2.07%, which is slightly larger than the 2.6 MeV threshold. For the varied parameters in the MC, we have not studied the correlation of these parameters yet, nor have we found the best set of parameter values which gives the best overall agreement with all the gamma sources calibration data. Therefore, more careful study is needed in the future.

Bibliography

[1] References to early literature on the subject can be obtained in K Winter (ed): Neutrino Physics (Cambridge University Press., 1991).

[2] For an English translations of the text of this latter, see Pauli's article in Ref. [1].

[3] E Fermi: Ricercha Scient. 2 (1933) 12; ZPh 88 (1934) 161.

[4] F.Reines, C.L. Cowan, Nature 178 (1956) 446.

[5] G.Backenstoss *et al.*, Phys. Rev. Lett. 6 415 (1961).

[6] J.N.Bahcall, S.Basu and M.H.Pinsonneault, Phys. Lett. B 433 (1998) 1-8.

[7] J.N.Bahcall, M.H.Pinsonneault and S.Basu, astr-ph/0010346.

[8] J.N.Bahcall's home page, http://www.sns.ias.edu jnb.

[9] S.Basu *et al.*, Mon. Not. R. Astron. Soc. 292 (1997) 1402.

[10] R.Davis Jr., D.S.Harmer and K.C.Hoffman, Phys. Rev. Lett. 20 (1968) 1205.

[11] A.I.Abazov *et al.*, Phys. Rev. Lett. 67 (1991) 3332.

[12] P.Anselmann *et al.*, Phys. Rev. Lett. B 285 (1992) 376.

[13] K.S.Hirata *et al.*, Phys. Rev., D 38 (1988) 448.

[14] Y.Fukuda *et al.*, Phys. Rev. Lett. 81 (1998) 1158.

[15] M.Altmann *et al.*, Phys. Rev. Lett. B 490 (2000) 16-26.

[16] S.Fukuda *et al.*, Phys. Rev. Lett. 86 (2001) 5651-5655.

[17] Q.R. Ahmad *et al.*, Phys. Rev. Lett. 87 (2001) 071301.

[18] R.C.Svoboda *et al.*, Nucl. Phys. B38, (1995).

[19] K.S.Hirata *et al.*, Phys. Lett. B280, 146 (1992).

[20] M.Ambrosio *et al.*, hep-ex/0304037

[21] M.Gell-Mann and A.Pais, Phys. Rev. 97 (1955) 1387.

[22] B.Pontecorvo, Sov. Phys. JEPT 6 (1958) 429.

[23] Z.Maki *et al.*, Prog. Theor. Phys. 28 (1962) 870.

[24] S.Bilenky and B.Pontecorvo, Phys. Reports 41 (1978) 225.

[25] Particle Data Group, D.E. Groom *et al.*, Eur. Phys. J. C15 (2000) 1.

[26] Z.Maki, M.Nakagawa, S.Sakata, progr. Theor. Phys. 28 (1962) 870.

[27] M. Kobayashi and T. Maskawa, Prog. Theor. Phys. 49, 652 (1973);
N. Cabibbo, Phys. Rev. Lett. 10, 531 (1963).

[28] L.Wolfenstein, Phys. Rev. D17 (1978) 2369.
S.P.Mikheyev and A.Yu.Smirnov, Yad. Fiz. 42 (1985) 1441.

[29] Q.R. Ahmad *et al.*, Phys. Rev. Lett. 89 (2002) 011302.

[30] J.B.Bahcall, P.I.Krastev and A.Yu. Smirnov, Phys. Rev. D 58 (1998) 096016.

[31] M.H.Ahn *et al.*, hep-ex/0212007 v2 16 Dec. 2002.

[32] M.Apollonio *et al.*, Phys. Lett. B 466 (1999) 415.

[33] F. Boehm *et al.*, Phys. Rev. Lett. 84 (2000) 3764.

[34] C.Athanassopoulos
et al., Phys. Rev. Lett. 81, 1774 (1998); C.Athanassopoulos *et al.*, Phys.
Rev. Lett. 77, 3082 (1996).

[35] K.Eguchi *et al.*, Phys. Rev. Letters, 90, 2 (2003).

[36] J.Busenitz *et al.*, Proposal for US Participation in KamLAND, March, 1999.

[37] G.L. Fogli *et al.*, Phys. Rev. D66 053010 (2002).

[38] R. Hertenberger *et al.*, Phys. Rev. C52, 3449 (1995).

[39] F. Boehm *et al.*, Phys. Rev. D62 (2000) 072002

[40] L.B. Bezrukov *et al.*, Sov. J. Nucl. Phys. 17, 51 (1973).

[41] R.I. Enikeev *et al.*, Sov. J. Nucl. Phys. 46, 1492 (1987).

[42] M. Aglietta *et al.*, Nuovo Cimento C12, 467 (1987).

[43] M. Aglietta *et al.*, Proc. 26th Inter. Cosmic Ray Conf., 1999, V2, p44, hep-ex/9905047.

[44] Y-F Wang *et al.*, Phys. Rev. D64 (2001) 013012, hep-ex/10101049, 27 Jan. 2001.

[45] K. Hirata *et al.*, Phys. Rev. D44, 2241 (1991).

[46] The Federation of Electric Power Companies, Japan, "Status of Electric Power Industry 1996 - 97" in Japan.

[47] D-M Mei *et al.*, Am-Be as a neutron calibration source for KamLAND, http://bama.ua.edu/ mei001/kamland/neutronindex.html.

[48] A.D.Vijaya and Arun Kumar, Nucl. Instr. and Meth. III (1973) 435-440.

[49] D.E. Groom, Univ. of Utah internal note, No. UUCR 102 (unpublished).

[50] G.L. Cassiday *et al.*, Phys. Rev. D7, 2022 (1973).

[51] M.Aglietta *et al.*, Phys. Rev. D58, 092005 (1998).

[52] Thomas K. Gaisser, Cosmic Ray and Particles 1990,p.77.

[53] P. Lipari and T. Stanev, Phys. Rev. D44, 3543 (1991).

[54] G.Battistoni *et al.*, hep-ex/9809006 v1, 9 Sep. 1998.

[55] M.Ambrosio *et al.*, hep-ex/0207043 v2, 18 Jan. 2002.

[56] A.F. Khalchukov *et al.*, IL NUOVO CIMENTO 6C, 320 (1983).

[57] J.C.Barton, Proc. 19th Inter. Cosmic Ray Conf., La Jolla, 1985, Physical Society, London, p.98.

[58] V.Chazal *et al.*, Nucl. Instrum. ℘ Meth. in Phys. Res. A, 490 (2002) 334, hep-ex/0102028.

[59] K.V.Alanakyan *et al.*, Sov. J. Nucl. Phys. 34, (1981) 828.

[60] G.L. Cassiday *et al.*, Phys. Rev. D7, 2022 (1973).

[61] P. Lipari and T. Stanev, Phys. Rev. D44, 3543 (1991).

[62] Review of Particle Physics volume 15, Number 1-4 2000.

[63] T.Kozlowski *et al.*, Nucl. Phys. A 436 (1985) 717-732.

[64] S.Matsuno *et al.*, Phys. Rev. D29, 1 (1984).

[65] T.Suzuki *et al.*, Phys. Rev. C35, 2212 (1987).

[66] L.Baudis *et al.*, Phys. Rev. Lett. 83 (1999) 41.

[67] C.F.Weizsäcker, Z. Phys. 88 (1934) 612; E.J. Williams, Kfl. Dan. Vidensk. Selsk. Mat. Fys. Medd. XIII (1935) 4.

[68] Jean Delorme *et al.*, Phys. Rev. C 52 (1995) 2222.

[69] L.W.Jones and K.M.Terwilliger, Phys. Rev. 91 (1953) 699.

[70] V.A.Kudryavtsev *et al.*, hep-ex/0303007 v1 9 Mar. 2003.

[71] Alimonti G. *et al.* Light propagation in a large volume liquid scintillator NIM 406 (1998) 411-426.

[72] R.Brun *et al.*, "GEANT3", CERN DD/EE/84-1 (revised), 1987.

[73] C.Zeitnitz *et al.*, Nucl. Instr. and Meth. in Phys. Res. A 349 (1994) 106-111

[74] J.B. Birks, Proc. Phys. Soc. A64 (1951) 874.

[75] J.D.Jackson, Classical Electrodynamics, 2nd edition, (John Wiley and Sons, New York, 1975).